MODELLING OF SINGLE CRYSTAL SUPERALLOYS UNDER SEVERE THERMOMECHANICAL LOADINGS

A THESIS SUBMITTED TO
THE GRADUATE SCHOOL OF NATURAL AND APPLIED SCIENCES
OF
ATILIM UNIVERSITY

BY

ÇAĞATAY KASAR

IN PARTIAL FULFILLMENT OF THE REQUIREMENTS
FOR
THE DEGREE OF DOCTOR OF PHILOSOPHY
IN
THE DEPARTMENT OF MECHANICAL ENGINEERING

JUNE 2025

Approval of the Graduate School of Natural and Applied Sciences, Atılım University.

_____

Assoc. Prof. Dr. Gökhan TUNÇ

Director

I certify that this thesis satisfies all the requirements as a thesis for the degree of **Doctor of Philosophy in Mechanical Engineering Department, Atılım University**.

_____

Prof. Dr. Hasan Umur AKAY

Acting Head of Department

This is to certify that we have read the thesis MODELLING OF SINGLE CRYSTAL SUPERALLOYS UNDER SEVERE THERMOMECHANICAL LOADINGS submitted by ÇAĞATAY KASAR and that in our opinion it is fully adequate, in scope and quality, as a thesis for the degree of Doctor of Philosophy.

_____

Prof. Dr. Özgür ASLAN

Supervisor

Examining Committee Members:

Prof. Dr. Ahmet Hakan ARGEŞO
Aerospace Engineering, Atılım University _____

Prof. Dr. Özgür ASLAN
Mechanical Engineering, University of Bristol _____

Asst. Prof. Dr. Ferit SAİT
Mechanical Engineering, Çankaya University _____

Asst. Prof. Dr. Hakan KALKAN
Mechanical Engineering, Atılım University _____

Asst. Prof. Dr. Bahram LOTFİ
Mechanical Engineering, TOBB ETU _____

Date: June 27, 2025

I declare and guarantee that all data, knowledge and information in this document has been obtained, processed and presented in accordance with academic rules and ethical conduct. Based on these rules and conduct, I have fully cited and referenced all material and results that are not original to this work.

Name, Last Name : ÇAĞATAY KASAR

Signature :

ABSTRACT

MODELLING OF SINGLE CRYSTAL SUPERALLOYS UNDER SEVERE THERMOMECHANICAL LOADINGS

Kasar, Çağatay

Ph.D., Department of Mechanical Engineering

Supervisor : Prof. Dr. Özgür ASLAN

June 2025, 122 pages

This thesis develops a computational framework for modeling fatigue crack initiation and growth in nickel-based single crystal superalloys under cyclic loading. A fully implicit crystal plasticity model is coupled with two damage regularization approaches: a gradient-enhanced microdamage continuum and a phase-field formulation for ductile fracture. The microdamage model introduces an internal length scale, enabling mesh-independent simulations that capture fatigue crack branching consistent with experimental observations. Its extension to three dimensions offers new insights into the roles of stress triaxiality and plastic slip accumulation. The phase-field method, implemented as a complementary approach, provides a robust and consistent way to simulate complex fracture paths without predefined geometry. The combined modeling strategies form a versatile platform for fatigue life prediction, especially valuable for aerospace applications where accurate simulation of stress concentrations and localized deformation is essential. Future work includes incorporating creep effects, thermal coupling, and polycrystalline structures to enhance model applicability.

Keywords: Nickel Based Single Crystal Superalloys, Constitutive Modeling, Damage Mechanics, Fracture Mechanics, Fatigue Damage

ÖZ

TEK TANELİ KRİSTALLERİN ZORLU TERMOMEKANİK YÜKLEME KOŞULLARI ALTINDA MODELLENMESİ

Kasar, Çağatay

Bütünleşik Doktora, Makina Mühendisliği

Tez Yöneticisi : Prof. Dr. Özgür ASLAN

Haziran 2025, 122 sayfa

Bu tez, nikel esaslı tek kristal süperalaşımlarda çevrimsel yükleme altında yorulma çatlağı başlama ve ilerlemesini modellemek amacıyla bir hesaplamalı çerçeve geliştirmektedir. Tam örtük kristal plastikliği modeli, gradyanla düzenlenmiş mikrohasar kontinuumu ve sünek kırılma için faz alanı yaklaşımıyla birleştirilmiştir. Mikrohasar modeli, içsel bir uzunluk ölçeği tanımlayarak ağdan bağımsız sonuçlar üretmekte ve deneysel çatlak dallanma davranışını başarılı şekilde yakalamaktadır. Bu modelin üç boyutlu genişletilmesi, gerilme üç eksenliğinin ve plastik kayma birikiminin rolünü ortaya koymaktadır. Ayrıca faz alanı yöntemi, önceden tanımlanmamış çatlak yollarını tutarlı biçimde simüle edebilmektedir. Her iki yöntem birlikte ele alındığında, yorulma ömrü tahmini için güçlü ve esnek bir modelleme altyapısı sunmaktadır. Özellikle havacılık uygulamaları için gerilme yığılmalarının ve lokal plastikleşmenin doğru modellenmesi açısından büyük önem taşımaktadır. Gelecek çalışmalar, sünme etkisi, ısıl bağlaşım ve polikristal yapıların modele entegre edilmesi yönünde olacaktır.

Anahtar Kelimeler: Nikel Bazlı Süperalaşımlar, Malzeme Modellenmesi, Sürekli Ortamlar Mekaniği, Yorulma Hasarı

To my beloved Mother, with endless gratitude and love.

ACKNOWLEDGMENTS

First and foremost, I would like to express my deepest gratitude to Prof. Dr. Özgür Aslan, my supervisor, for his exceptional guidance, unwavering support, and constant encouragement throughout this thesis. His profound knowledge, insightful feedback, and open-minded mentorship made this journey both intellectually stimulating and personally fulfilling. It has been a privilege to be under his supervision.

I would also like to sincerely thank the members of my thesis committee for their valuable time, guidance, and constructive feedback. I am particularly grateful to Prof. Dr. Ahmet Hakan Argeşo for his leadership as the head of my thesis committee and for his involvement in my thesis monitoring committee. I also appreciate the support and insightful suggestions provided by Asst. Prof. Dr. Ferit Sait, who served on both the monitoring and defense committees. My thanks extend as well to Asst. Prof. Dr. Bahram Lotfi and Asst. Prof. Dr. Hakan Kalkan for their helpful comments and contributions, which strengthened the quality of this thesis.

Special thanks go to Prof. Dr. Emin Bayraktar for his generous support and fruitful collaboration during this project. His expertise and kindness have been greatly appreciated.

I am especially grateful to my colleague and best friend Utku Kaftancıoğlu, whose companionship and relentless support, especially during countless debugging sessions, transformed this PhD journey into an engaging and rewarding experience. I also extend my sincere thanks to the members of the Aslan Research Group, particularly Gamze Çakır Kabakçı and Caner Çamalan, for their friendship, collaboration, and stimulating discussions.

I would like to thank my colleagues from Turkish Aerospace Inc. for their understanding and support throughout my academic endeavors. I am particularly thankful to Dr. Funda Şeniz Bayraktar, Enes Pekdemir, Muhammed Keklik and Murat Ongun Aksu as well as the rest of the Fatigue and Damage Tolerance Team, for creating a professional environment that allowed me to grow as both an engineer and a researcher.

I am also thankful to Turkish Engine Industries (TEI) and TÜBİTAK for their financial support, which made this research possible and sustainable.

My heartfelt thanks also go to my closest friends Mustafa Can Şanlıtürk, Mertcan Sevinç, Engin Deniz Uçak, and Alaz Kahraman for always being there for me. Their friendship has been a source of strength and joy over the years.

I owe special gratitude to my family for their unwavering love and support. I thank my sister Ezgi Ocakçı and, most of all, my mother Birgül Kasar, whose belief in me has never wavered and whose sacrifices made this possible.

Finally, and above all, I dedicate my deepest appreciation to my beloved wife, Cansu Kasar. Her unconditional love, endless patience, and unwavering belief in me have been the cornerstone of this journey. Without her, none of this would have been possible. This work is as much hers as it is mine. She has earned the title Dr. Kasar in every way, not just for her emotional support, but for being an integral part of this success. These words are but a humble expression of a love that will last a lifetime. This thesis marks not only an academic achievement, but the first of many milestones we will reach together.

TABLE OF CONTENTS

LIST OF TABLES

TABLES

LIST OF FIGURES

FIGURES

LIST OF SYMBOLS

$\mathcal{B}$	:	Material body
$\mathcal{B}_0$	:	Reference configuration
$\mathcal{B}_t$	:	Current (deformed) configuration
$\mathbf{X}$	:	Material point in reference configuration
$\mathbf{x}$	:	Spatial position in deformed configuration
χ	:	Deformation mapping function
$\dot{\chi}, \ddot{\chi}$	:	Material velocity and acceleration
$\mathbf{u}$	:	Displacement vector
$\mathbf{F}$	:	Deformation gradient tensor
$\mathbf{F}^e$	:	Elastic part of deformation gradient
$\mathbf{F}^p$	:	Plastic part of deformation gradient
$\mathbf{F}^d$	:	Damage part of deformation gradient
J	:	Jacobian of deformation gradient, $J = \det \mathbf{F}$
$\mathbf{I}$	:	Second-order identity tensor
δ_{ij}	:	Kronecker delta
$\mathbf{U}$	:	Right Cauchy stretch tensor
$\mathbf{V}$	:	Left Cauchy stretch tensor
$\mathbf{R}$	:	Rotation tensor
$\mathbf{C}$	:	Right Cauchy-Green tensor, $\mathbf{C} = \mathbf{F}^{\mathrm{T}}\mathbf{F}$
$\mathbf{C}^e$	:	Elastic right Cauchy-Green tensor
$\mathbf{B}$	:	Left Cauchy-Green tensor, $\mathbf{B} = \mathbf{F}\mathbf{F}^{\mathrm{T}}$

$\mathbf{E}$: Green-Lagrange strain tensor, $\mathbf{E} = \frac{1}{2}(\mathbf{C} - \mathbf{I})$

$\mathbf{E}^e$: Hencky (logarithmic) elastic strain tensor

$\mathbf{L}$: Velocity gradient, $\mathbf{L} = \nabla \mathbf{v}$

$\mathbf{D}$: Rate-of-deformation tensor, $\mathbf{D} = \frac{1}{2}(\mathbf{L} + \mathbf{L}^{\mathrm{T}})$

$\mathbf{W}$: Spin tensor, $\mathbf{W} = \frac{1}{2}(\mathbf{L} - \mathbf{L}^{\mathrm{T}})$

ρ : Mass density

$\mathbf{v}$: Velocity vector

$\mathbf{a}$: Acceleration vector

$\mathbf{b}$: Body force per unit mass or microstress vector (context-dependent)

$\mathbf{t}$: Traction vector

$\boldsymbol{\sigma}$: Cauchy stress tensor

$\mathbf{P}$: First Piola-Kirchhoff stress tensor

$\mathbf{S}$: Second Piola-Kirchhoff stress tensor

e : Specific internal energy

η : Specific entropy

r : Internal heat generation per unit mass

h : Heat flux per unit area

$\mathbf{q}$: Heat flux vector

θ : Absolute temperature

γ : Entropy production per unit mass

ψ : Helmholtz free energy

Γ : Total entropy production

K	:	Kinetic energy
E	:	Internal energy
P	:	Mechanical power
Q	:	Thermal power
$\mathcal{D}$	:	Mechanical dissipation
$\boldsymbol{\varepsilon}$	:	Infinitesimal strain tensor
$\boldsymbol{\varepsilon}^p$	:	Plastic strain tensor
$\mathbf{D}^p$	:	Plastic rate of deformation
$\mathbf{R}^e$	:	Elastic rotation tensor
$\mathbf{U}^e$	:	Elastic right stretch tensor
$\mathbb{C}$	:	Fourth-order elasticity tensor (cubic symmetry)
C_{11}, C_{12}, C_{44}	:	Elastic constants in Voigt notation
μ'	:	Effective shear modulus
τ	:	Resolved shear stress
$\dot{\gamma}^\alpha$	:	Slip rate on system α
f^α	:	Yield function for slip system α
τ_{crit}	:	Critical resolved shear stress
γ_{cum}	:	Cumulative plastic slip
$\mathbf{m}^\alpha$	:	Slip direction for system α
$\mathbf{n}^\alpha$	:	Slip plane normal for system α
r^α	:	Slip resistance on system α
r_0	:	Initial slip resistance
T_m	:	Melting Temperature

q : Hardening coefficient

b : Saturation rate parameter

$h^{r\alpha}$: Latent hardening matrix

n : Rate sensitivity exponent

$\dot{\gamma}_0$: Reference slip rate

a : Scalar microforce conjugate to microdamage

${}^{\chi}d$: Microdamage field

d : Local scalar damage variable

${}^{\chi}H$: Penalty stiffness for microdamage consistency

A : Microdamage gradient regularization coefficient

Y_f : Thermodynamic driving force for damage

Y^s : Regularized damage threshold function

Y_0 : Initial cleavage strength

σ_{ult} : Ultimate strength at full damage

Θ : Damage-plasticity coupling parameter

ϕ : Phase-field variable for fracture

G_c : Critical energy release rate (fracture toughness)

ℓ : Regularization length scale in phase-field model

$\mathcal{H}$: History field (maximum energy density)

W^+ : Positive (tensile) part of elastic energy

W^- : Negative (compressive) part of elastic energy

η : Viscous regularization parameter for phase-field evolution

$\mathcal{D}_f$: Fracture dissipation

$\mathcal{D}_p$: Plastic dissipation

CHAPTER 1

INTRODUCTION

1.1 Background and Evolution of Jet Turbine Engines

The emergence and evolution of jet turbine engines represent a pivotal chapter in modern engineering history, revolutionizing aviation by enabling faster, more efficient, and longer-range flight. The conceptual foundations of gas turbines date back to the 18^{th} and 19^{th} centuries, when inventors such as John Barber and Charles Parsons proposed the principles of continuous combustion and rotary motion [1, 2]. However, the practical implementation of these ideas only materialized in the 1930s with the parallel development of turbojet propulsion by Sir Frank Whittle in the United Kingdom and Hans von Ohain in Germany. These independent breakthroughs culminated in the first flight of the Heinkel He 178 in 1939 and the Gloster E.28/39 in 1941 [3]. These early engines initiated a technological revolution that would evolve rapidly in both military and commercial aviation. The basic architecture of a modern jet turbine engine is illustrated in Figure 1.1, which delineates the cold and hot sections of the engine. The air intake initiates the process by directing ambient air into the core of the engine, minimizing distortion and pressure loss. This air enters the compressor, a multi-stage system of rotating (rotors) and stationary (stators) blades that increases the pressure of the incoming air by a factor of 20 to 40 in modern engines [2]. The compressed air is then fed into the combustion chambers, where it is mixed with fuel and ignited. The resulting high-pressure and high-temperature gas flows into the turbine, which extracts mechanical energy to drive the compressor and engine accessories through concentric shafts. Finally, the remaining energy in the gas is converted into thrust as it is expelled through the exhaust nozzle [1, 3].

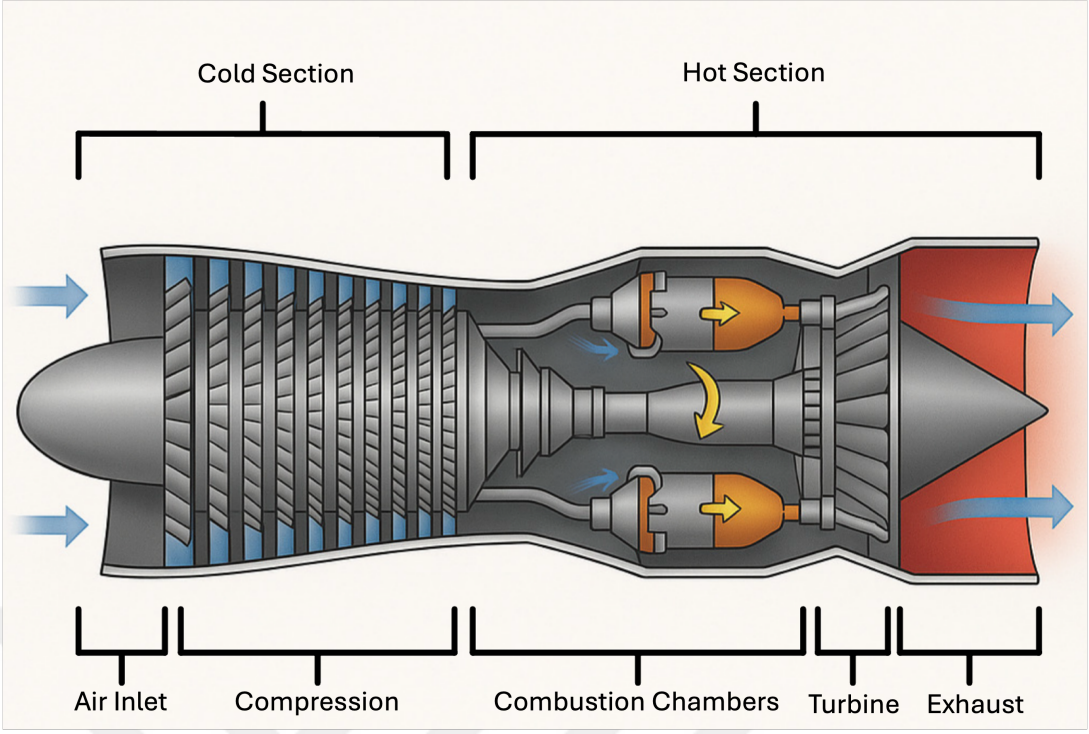

Figure 1.1: Schematic of a modern jet turbine engine. Representing two main sections.

Among these components, the turbine section is subjected to the most demanding thermomechanical environment. Located downstream of the combustion chamber, the turbine experiences gas temperatures exceeding 1100 °C, coupled with severe centrifugal forces from the high-speed rotation of the blades, and frequent thermal cycling during engine operation. These combined effects lead to material degradation phenomena such as creep, oxidation, and thermal fatigue [3, 4, 5]. The operational safety and performance of the engine are thus critically dependent on the ability of turbine blade materials to maintain mechanical integrity under these harsh conditions.

Figure 1.2 shows the Snecma M88 jet engine, developed for the Dassault Rafale fighter aircraft. The left image illustrates the entire engine, while the right image reveals internal modules including the high-pressure compressor, combustor, and turbine sections, which are central to the propulsion cycle and are the focal zones for material innovation [6].

Initially, turbine blades were manufactured from high-strength steels and basic nickel-chromium alloys, which offered limited creep resistance and oxidation stability. As

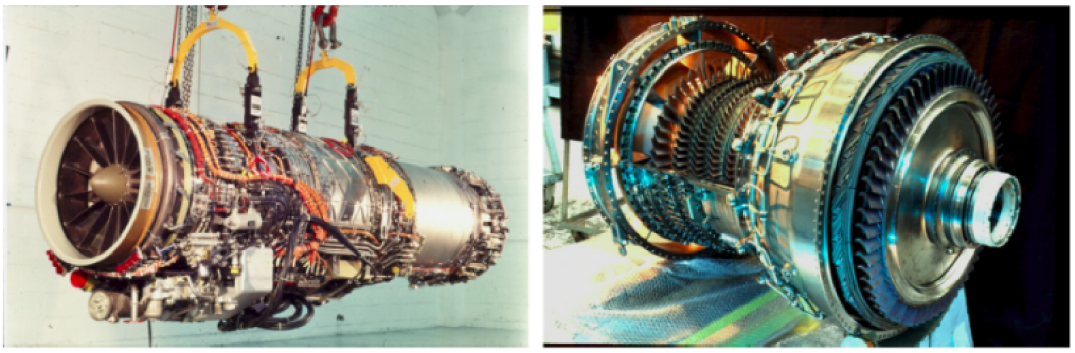

Figure 1.2: M88 Snecma jet engine (left), and close-up of the compressor, combustion chamber, and turbine (right) [6].

engine designs pushed toward higher turbine inlet temperatures to improve thermodynamic efficiency, these early materials proved inadequate. In response, the Nimonic series of nickel-based superalloys was introduced in the 1940s [3, 4, 1]. These alloys offered significant improvements in high-temperature strength and durability, enabling higher specific thrust and extended engine lifespans.

However, the most critical material challenge remained: resisting creep and fatigue damage over thousands of cycles at extreme temperatures. Creep, defined as the time-dependent deformation under stress, becomes especially pronounced above 0.6–0.7 of the material's melting point. In polycrystalline metals, grain boundaries act as preferred sites for creep cavitation and intergranular cracking, leading to premature failure. Likewise, thermal fatigue, driven by temperature gradients and cyclic operation, further compromises material life at grain boundaries.

These limitations drove the advancement of microstructural design in turbine blade alloys, as illustrated in Figure 1.3. The evolution progressed from polycrystalline equiaxed grains (left), to directionally solidified (DS) columnar grains (middle), and ultimately to single crystal (SX) structures (right). In DS blades, grains are aligned along the primary loading direction, minimizing transverse grain boundaries and improving creep performance in the axial direction. However, residual boundaries still exist and can be detrimental under multiaxial or thermal fatigue conditions.

The breakthrough came with the adoption of single crystal superalloys, manufactured via Bridgman-type directional solidification. These blades are grown as a single grain,

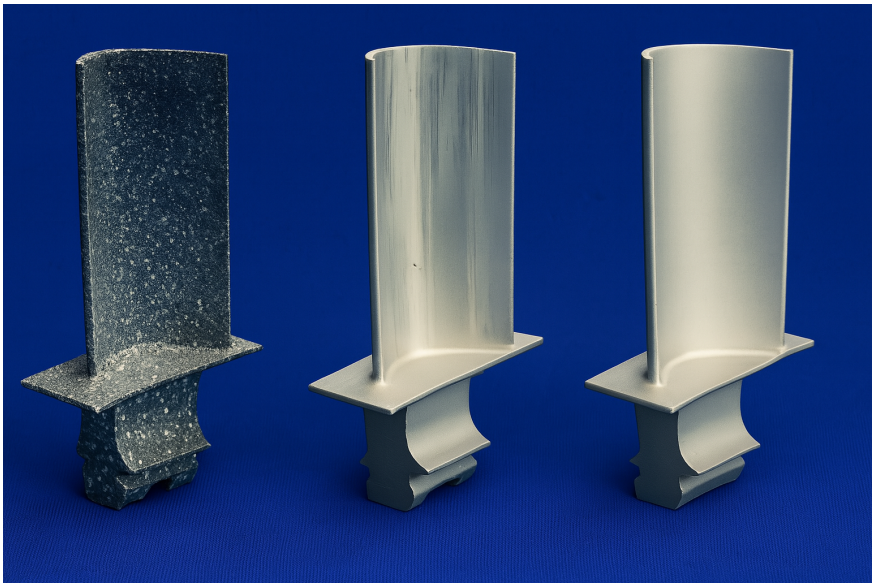

Figure 1.3: Ni-based superalloy turbine blades. Equiaxed polycrystal (left), directionally solidified (middle), single crystal (right) [7].

completely eliminating grain boundaries. This results in a dramatic improvement in creep resistance, thermal fatigue strength, and oxidation/corrosion durability [5, 8]. Furthermore, aligning the [001] crystallographic axis—the most creep-resistant direction in face-centered cubic crystals—with the principal stress axis, enables the full utilization of the alloy's anisotropic mechanical properties [3].

Single crystal blades also allow for tailored alloy chemistries, incorporating elements such as aluminum (for γ' strengthening), rhenium (to enhance creep), and tantalum or tungsten (to stabilize phases at high temperatures) [9]. These innovations led to modern superalloys such as CMSX-4, PWA1480, and René N4, which are now standard in both military and commercial turbine applications [8].

In this thesis, these advanced materials—single crystal nickel-based superalloys—are placed at the center of investigation from the perspective of computational modeling. Emphasis is placed on their anisotropic mechanical behavior, deformation mechanisms under high-temperature loading, and the numerical frameworks required to simulate their response accurately. A comprehensive treatment of their microstructural characteristics, constitutive modeling, and numerical implementation will be presented in the following chapters. The reader is referred to the thesis outline in the subsequent section for a detailed roadmap of the topics explored.

1.2 Scope and Outline

The primary objective of this thesis is to develop and rigorously validate micro mechanics based computational models capable of predicting crack initiation and 3D crack propagation in nickel-based single crystal superalloys under severe loading conditions typical of aerospace turbine engines. The research places significant emphasis on ensuring the physical realism and predictive capability of the proposed models, leveraging advanced crystal plasticity theories integrated with continuum damage mechanics. A distinctive and novel aspect of this work involves implementing a gradient-based microdamage regularization technique. This approach ensures the physical consistency of damage evolution, eliminating mesh dependency and providing physically meaningful insights into crack nucleation and growth mechanisms. Notably, the comprehensive three-dimensional investigation of crack initiation and propagation performed in this thesis fills a critical gap within the existing literature, where prior studies have been predominantly limited to two-dimensional representations or simplified fracture modeling approaches.

To further advance the robustness of damage simulations, a second regularization strategy is introduced via a variational **phase-field fracture formulation**. This approach, rooted in energy minimization principles, allows for the smooth representation of complex crack topologies and provides a thermodynamically consistent alternative to conventional damage models. Both regularization techniques—gradient microdamage and phase-field—are implemented and critically compared in terms of theoretical foundations, numerical performance, and physical interpretability. This comparative modeling framework enables a comprehensive exploration of crack nucleation, propagation, and fatigue behavior in anisotropic single crystal systems.

The thesis is organized into the following chapters:

- **Chapter 2: Nickel-Based Single Crystal Superalloys**
  This chapter reviews the physical metallurgy, phase constitution, microstructure, and mechanical properties of Ni-based single crystal superalloys. It establishes the materials science context needed for subsequent modeling developments.

- **Chapter 3: Theoretical and Computational Framework**
  This chapter introduces the thermomechanical foundation and kinematic framework of crystal plasticity. It presents the constitutive laws, flow rules, hardening behavior, and the numerical implementation of an implicit integration scheme. Model verification is performed through tension–torsion and CT specimen simulations.

- **Chapter 4: Damage Modeling of Single Crystals**
  This chapter formulates two complementary damage regularization strategies: a gradient-enhanced microdamage model and a phase-field formulation coupled to crystal plasticity. Their governing equations, variational formulations, and finite element implementations are detailed. Numerical simulations in one, two, and three dimensions are used to evaluate each model's capability in describing crack growth, localization, and fatigue degradation.

- **Chapter 5: Conclusions and Future Work**
  The final chapter summarizes the key contributions of the thesis, discusses the comparative insights gained from the dual regularization strategies, and outlines potential directions for further research and application.

Overall, this thesis bridges advanced constitutive modeling, microstructure-informed damage regularization, and high-fidelity numerical simulation to provide a predictive and physically grounded framework for understanding failure in nickel-based single crystal superalloys.

CHAPTER 2

Nickel Based Single Crystal Superalloys

2.1 Introduction

Nickel-based single crystal (SC) superalloys are among the most advanced metallic materials ever developed, renowned for their unparalleled performance in extreme environments. Their superior resistance to creep, fatigue, oxidation, and corrosion at high temperatures is a direct consequence of decades of targeted alloy design and microstructural optimization [3, 5]. These alloys are specifically engineered to operate at homologous temperatures approaching 0.9 T_m, where most structural materials would experience rapid degradation.

The distinguishing feature of single crystal superalloys is their ability to maintain mechanical integrity without the presence of grain boundaries, which are often the weakest structural elements in polycrystalline materials. Grain boundaries are known sites for diffusion, creep, environmental attack, and fatigue crack initiation. Their removal eliminates grain boundary sliding and void formation, two primary failure mechanisms under thermal-mechanical loads [10, 11].

More fundamentally, the performance of these alloys is governed by their characteristic two-phase microstructure: a disordered face-centered cubic (FCC) γ matrix phase and a coherent, ordered γ' phase with an $L1_2$ crystal structure, typically Ni_3(Al, Ti, Ta). The lattice coherency between these two phases leads to misfit strains that significantly impede dislocation motion, thereby enhancing high-temperature strength [12, 3]. The stability and morphology of γ' precipitates are central to the alloy's mechanical behavior and are sensitively dependent on alloy chemistry and heat treatment.

A unique feature of single crystal superalloys is their anisotropic mechanical response, which is inherently linked to their crystallographic orientation and slip system activity. Deformation occurs through a limited set of $\{111\}\langle 110\rangle$ slip systems, and the activation of these systems depends strongly on loading direction, temperature, and internal stress state [13]. This directional dependence is critical in understanding not only yield behavior but also fatigue and creep anisotropy.

Given their complex deformation mechanisms and sensitivity to microstructural evolution, the modeling of single crystal superalloys requires advanced constitutive frameworks that capture crystallographic anisotropy and microstructure-property relations. Conventional isotropic models are inadequate for predicting orientation-dependent plastic flow, dislocation interactions with γ' precipitates, or the role of lattice misfit in creep deformation. As a result, physically motivated crystal plasticity models have become the cornerstone of recent efforts to simulate the mechanical behavior of these materials under realistic service conditions [6, 14, 15].

This chapter aims to provide a comprehensive and materials-science-focused overview of nickel-based single crystal superalloys. Beginning with their chemical composition and phase constitution, it proceeds to examine their microstructure, processing methods, and the fundamental mechanisms governing their deformation. The discussion then transitions to their macroscopic mechanical properties—including tensile response, fatigue resistance, and creep behavior—before concluding with a historical account of alloy development. This foundation is essential for developing and validating the constitutive and damage models introduced in later chapters.

2.1.1 Chemical Composition

The high-temperature mechanical excellence of nickel-based single crystal (SC) superalloys is primarily attributed to their meticulously tailored chemical compositions. These alloys are engineered with up to a dozen alloying elements, each fulfilling specific roles such as strengthening, phase stabilization, oxidation resistance, and microstructural control [3, 5, 16].

The alloying strategy in SC superalloys revolves around partitioning between the face-centered cubic (FCC) γ matrix and the ordered $L1_2$ γ' phase (typically Ni_3(Al,Ti,Ta)).

This two-phase structure is the key to achieving both strength and creep resistance at elevated temperatures [13, 11]. The role of the major alloying elements can be categorized as follows:

- **Precipitation Strengtheners:** Aluminum is the principal γ'-forming element, typically present at 5–6 wt.%, enabling the formation of a coherent Ni_3Al phase that resists shearing [3, 5]. Titanium, tantalum, and niobium are added to enhance γ' stability by increasing the anti-phase boundary (APB) energy [17, 18]. These elements preferentially partition to the γ' phase and contribute to its cubic or cuboidal morphology.

- **Solid Solution Strengtheners:** Refractory elements such as rhenium (Re), tungsten (W), and molybdenum (Mo) segregate into the γ matrix and reduce dislocation mobility through solute drag [19, 20]. Re is especially potent due to its slow diffusion and atomic size mismatch, which increases lattice resistance to creep [5, 21]. W and Mo also contribute to strengthening but carry a higher risk of promoting topologically close-packed (TCP) phases under prolonged exposure.

- **Phase Stability Enhancers:** Ruthenium (Ru), introduced in fourth-generation alloys, does not significantly partition into either phase but stabilizes the microstructure by suppressing TCP phase formation through thermodynamic effects on element partitioning and diffusivity [19, 22, 13]. It also moderates the partitioning behavior of Re and W, effectively delaying TCP precipitation without degrading mechanical strength.

- **Oxidation and Corrosion Resistance:** Aluminum supports the formation of protective Al_2O_3 scales, while chromium contributes Cr_2O_3 formation in earlier alloy generations [3, 23]. However, Cr promotes TCP phases and is often reduced in later designs, with oxidation protection increasingly provided by external coatings [19].

The evolution of SC superalloys from second to fourth generation reflects a consistent increase in Re content for creep resistance, followed by the addition of Ru to mitigate

TCP formation. Table 2.1 summarizes representative compositions that illustrate these trends [5, 19, 22].

Table 2.1: Typical compositions (wt.%) of selected Ni-based single crystal superalloys [5, 19, 22].

Alloy	Al	Ta	W	Re	Mo	Cr	Co	Ti	Ru	Others
CMSX-4	5.6	6.5	6.0	3.0	0.6	6.5	9.0	1.0	–	Hf, Y
René N5	6.2	5.0	5.0	3.0	1.3	7.0	7.5	–	–	Hf, C
CMSX-10	5.9	8.0	5.0	6.0	–	2.0	5.0	–	–	Hf, Y
TMS-138	5.9	6.0	5.0	6.0	–	2.0	7.5	–	2.5	Hf

As shown in Table 2.1, the transition from CMSX-4 to TMS-138 involves increased use of Re and the introduction of Ru, allowing for higher refractory loading while suppressing unwanted phase transformations [22, 19]. Simultaneously, the reduction of Cr content illustrates the trade-off between oxidation resistance and TCP phase suppression [23].

In conclusion, the chemical composition of SC superalloys is the primary design lever that governs phase constitution, lattice misfit, diffusion kinetics, and creep resistance. These chemical strategies set the stage for the microstructural phenomena and thermomechanical responses addressed in the next sections.

2.1.2 Microstructure

The superior high-temperature performance of nickel-based single crystal (SC) superalloys is fundamentally linked to their engineered two-phase microstructure, composed of a face-centered cubic (FCC) γ matrix and ordered $L1_2$ γ' precipitates. This architecture provides an exceptional balance of strength, creep resistance, and microstructural stability under thermal and mechanical loading [16].

The γ phase is a Ni-rich disordered solid solution matrix that accommodates most of the refractory alloying elements (Re, W, Mo, etc.) and provides ductility. The γ' phase, with a nominal Ni_3(Al,Ta,Ti) composition, is an ordered intermetallic with the $L1_2$ structure, offering excellent resistance to dislocation motion and coarsening [17, 20]. The lattice coherency between the two phases results in elastic interactions that contribute to precipitation strengthening.

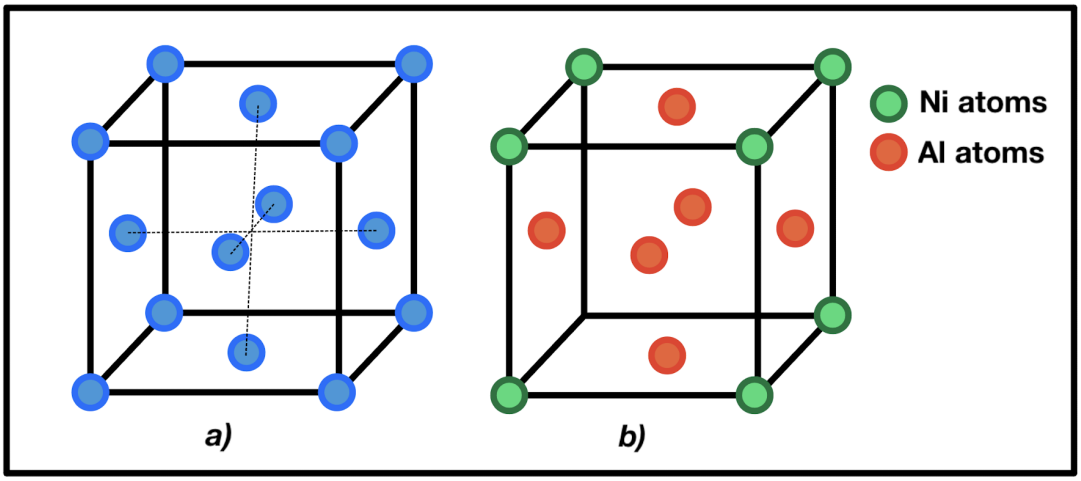

Figure 2.1: Atomic arrangement of the γ (FCC Ni solid solution) and γ' ($L1_2$ Ni_3Al) phases.

The γ' precipitates are typically cuboidal and uniformly distributed within the γ matrix. Their size ranges from 300–600 nm, and their volume fraction is usually between 65–75% in modern SC alloys [3, 18]. This microstructure imparts high strength and creep resistance by confining dislocation movement to narrow γ channels [13].

Most SC superalloys are designed with a slightly negative misfit (-0.1% to -0.3% at room temperature), promoting cuboidal precipitate morphology and coherency stresses that enhance creep resistance [13].

At elevated temperatures under stress, this microstructure evolves via directional coarsening or "rafting." In negative misfit alloys, γ' precipitates align perpendicular to the loading direction, impeding dislocation climb and increasing creep life [11, 20]. The rate of rafting depends on alloying content (especially Re and Ru), temperature, and stress orientation.

Ru-containing fourth-generation alloys such as TMS-138A show delayed rafting and superior microstructural stability during long-term aging, due to the sluggish diffusion and suppressed TCP phase formation [19, 22]. This makes the γ/γ' architecture not only effective in its initial state, but also resilient under service-like conditions.

In summary, the γ/γ' microstructure is the defining feature of Ni-based SC superalloys. Its morphology, volume fraction, coherency, and directional evolution govern

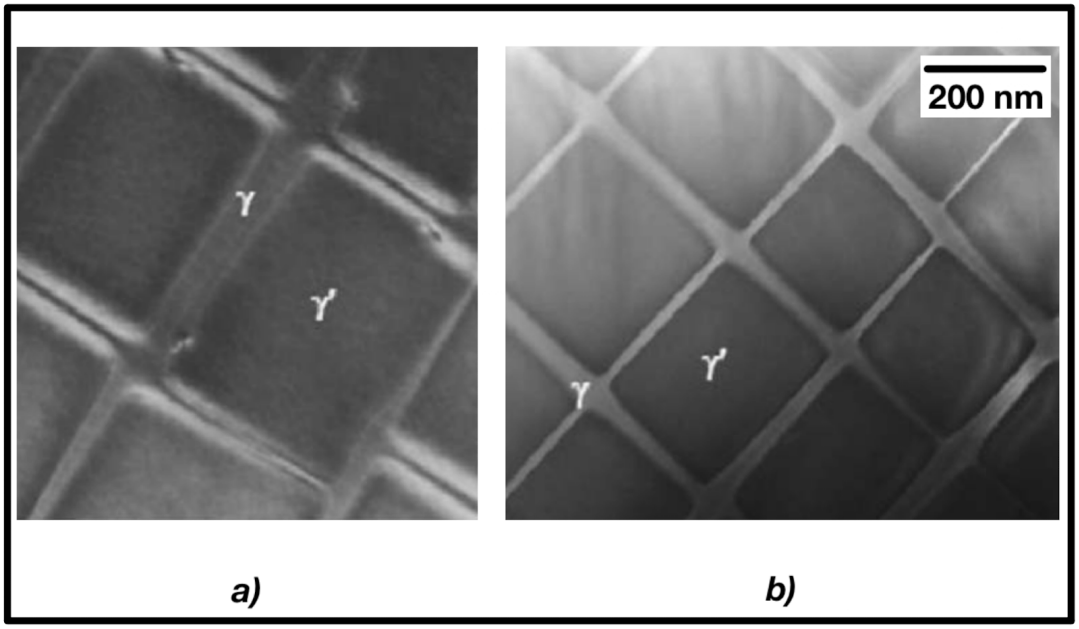

Figure 2.2: Post-heat treatment SEM micrographs of Ni-based SC superalloys: (a) TMS-138A (4th generation), (b) TMS-168 (5th generation). Cuboidal γ' precipitates are embedded in the γ matrix [24].

the alloy's thermomechanical performance. The next section examines how such microstructures are achieved and stabilized through heat treatment.

2.1.3 Heat Treatment

Heat treatment plays a critical role in developing and optimizing the two-phase γ/γ' microstructure of Ni-based single crystal (SC) superalloys. Through a carefully tailored thermal schedule—comprising high-temperature solution treatment followed by controlled aging steps—metallurgists refine the size, morphology, and distribution of γ' precipitates, ensuring peak mechanical performance and long-term stability [16].

The rationale behind heat treatment is grounded in the phase equilibria of the Ni–Al binary system, where γ (Ni) and γ' (Ni_3Al) phases coexist over a range of compositions and temperatures.
As shown in Figure 2.3, the γ' phase forms in the Ni-rich corner of the phase diagram below its solvus temperature, which lies between 1200–1300°C depending on alloy chemistry and the presence of tertiary elements [25].

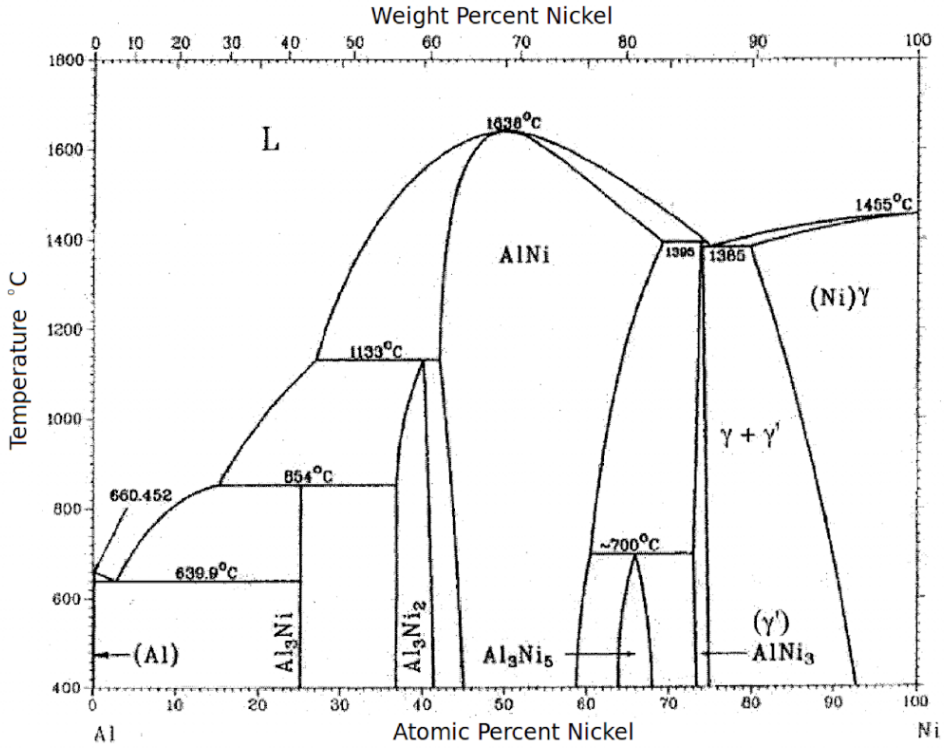

Figure 2.3: The Ni–Al binary phase diagram, illustrating the γ, γ', and $\gamma + \gamma'$ phase fields [25].

- **Solution Treatment** The as-cast microstructure of SC superalloys contains chemical segregation due to solidification, with heavy refractory elements (e.g., Re, W) concentrated in dendritic cores and γ'-forming elements (Al, Ta) enriched in interdendritic regions [5]. Additionally, residual eutectic γ–γ' pools may be present.

  To homogenize the alloy and dissolve pre-existing γ' and eutectic phases, a solution treatment is performed slightly below the solidus and γ' solvus temperatures, often in the range of 1280–1320°C [3]. This thermal cycle eliminates as-cast heterogeneities and establishes a clean γ matrix ready for controlled precipitation [16].

- **Aging Treatment** A two-stage aging schedule is typically employed. The first step (e.g., 1140–1160°C for 4–8 hours) precipitates primary cuboidal γ' with edge lengths of 400–600 nm. The second step (e.g., 870–900°C for 16–24

hours) produces finer secondary γ' within the matrix channels [17, 20]. This bimodal distribution enhances creep strength and tensile properties by impeding dislocation motion at both high and intermediate temperatures.

- **Thermodynamic Basis and Control** The γ' solvus temperature, determined from the phase diagram and influenced by Co, Cr, Ta, and Re content, dictates the upper limit of the solution treatment. If this temperature is exceeded, incipient melting can occur, damaging the component. Conversely, under-solutioning results in retained eutectics and coarse precipitates, degrading mechanical performance [18, 16].

- **Cooling and Rejuvenation**

  After aging, controlled cooling avoids formation of excessive tertiary γ' precipitates, which, though initially strengthening, are unstable during long-term service [26]. In degraded components, rejuvenation heat treatments (partial or full re-solution followed by re-aging) can restore the γ/γ' architecture, particularly in Ru-containing fourth-generation alloys where microstructural degradation occurs more slowly [19].

In summary, the design of heat treatment schedules in SC superalloys is deeply rooted in phase equilibrium principles. The Ni–Al binary system provides the foundational understanding, while the addition of multicomponent alloying necessitates precise thermal control to develop the desired precipitate morphologies and maintain long-term phase stability.

2.1.4 Strengthening Mechanisms

The exceptional high-temperature strength of Ni-based single crystal (SC) superalloys is the outcome of several carefully engineered and interrelated strengthening mechanisms. These mechanisms operate across scales and timescales to impede dislocation motion, stabilize microstructure, and ensure creep resistance under extreme thermo-mechanical loads [20, 16].

2.1.4.1 Precipitation Strengthening via γ' Phase

The dominant source of strengthening arises from coherent γ' precipitates, which are typically Ni_3(Al,Ta,Ti) intermetallics with an ordered $L1_2$ crystal structure. These particles are coherent with the disordered FCC γ matrix and form a periodic, cuboidal distribution with a high volume fraction (typically 65–75%) [20, 17].

Dislocations interacting with these precipitates exhibit two primary mechanisms, shown in Figure 2.4:

- *Orowan bypassing:* Dislocations bow around non-shearable γ' precipitates, forming loops and leaving behind residual stress fields that resist further motion [27, 28, 29].
- *Cutting:* When precipitates are sufficiently fine and APB energy is low, dislocations may shear through them, forming APBs and stacking faults [20, **?**].

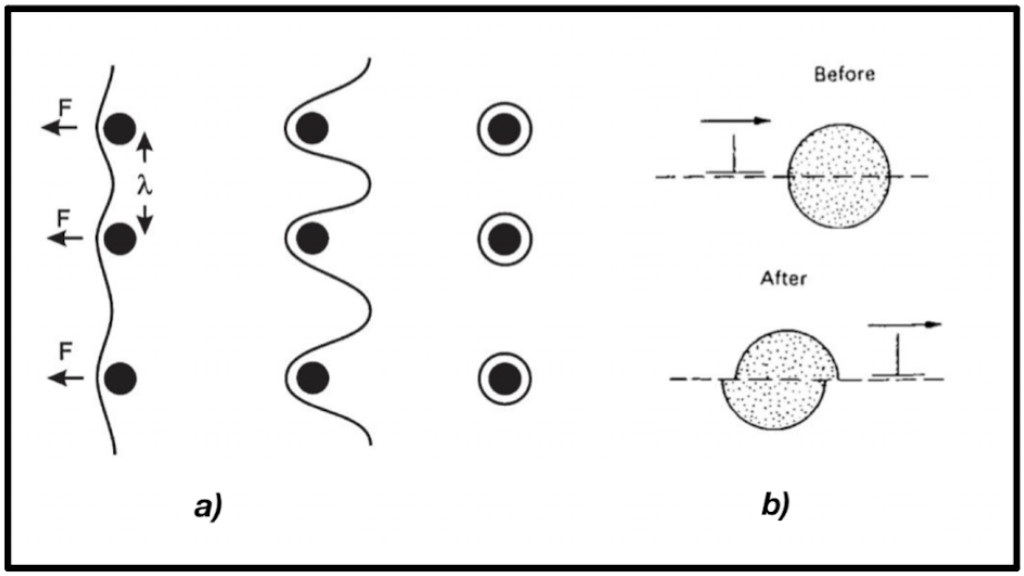

Figure 2.4: Dislocation–precipitate interaction mechanisms: (a) Orowan bypass of non-shearable particles [27]; (b) shearing of coherent precipitates [28].

The threshold stress for Orowan looping increases with decreasing particle spacing, while shearing resistance is governed by γ' size, ordering, and APB energy. Ta, Ti, and Nb increase the APB energy and favor bypassing, enhancing creep resistance [18].

2.1.4.2 Solid Solution Strengthening in γ Matrix

The disordered γ matrix is strengthened by refractory solutes such as rhenium (Re), tungsten (W), and molybdenum (Mo). These elements generate elastic strain fields due to atomic size mismatch and retard dislocation motion via solute drag [21, 22, 19].

Re, in particular, provides significant solid solution strengthening due to its low diffusivity and high misfit, which also reduces dislocation climb mobility during creep [3, 5]. The combined Re–W–Mo additions delay dislocation motion and stabilize the γ matrix at elevated temperatures [20].

2.1.4.3 Coherency Strengthening and Lattice Misfit

The γ/γ' interface is coherent and associated with a small lattice misfit:

$$\delta = \frac{a_{\gamma'} - a_{\gamma}}{a_{\gamma'}} \times 100 \tag{2.1}$$

where $a_{\gamma'}$ and a_{γ} are the respective lattice parameters. Most modern SC alloys are engineered with negative misfit ($\delta \approx -0.1\%$ to -0.3%), resulting in coherency strains that generate back-stresses against dislocation motion [16, 13].

This misfit not only strengthens the alloy through elastic interaction but also governs the directionality of rafting under creep. Negative misfit favors γ' rafting perpendicular to the load axis, creating plate-like structures that confine dislocation movement and improve creep life [11, 29].

2.1.4.4 Creep Strengthening via Dislocation Interactions

At high temperatures, dislocation motion is limited primarily to the γ channels between γ' precipitates. As deformation proceeds:

- Dislocations accumulate in γ channels due to the impenetrability of γ'.
- Climb becomes the rate-limiting step, particularly at low strain rates [20, 13].
- Cross-slip and climb are further delayed by solute drag and rafting.

Advanced alloys with Ru and Re additions exhibit delayed coarsening and suppressed TCP phase formation, thereby preserving strengthening mechanisms for longer durations [22, 19].

2.1.4.5 Summary

In combination, the following mechanisms act synergistically:

- Precipitation hardening by coherent γ' particles
- Solid solution strengthening in γ by Re, W, Mo
- Coherency strengthening through lattice misfit strains
- Creep resistance via dislocation–precipitate interactions, Orowan looping, and rafting

These metallurgical strategies enable SC superalloys to operate under extreme conditions of stress and temperature, particularly in turbine blades and high-performance aerospace components.

2.2 Deformation Mechanisms

2.2.1 Plastic Slip in FCC Nickel-Based Superalloys

Nickel-based single crystal (SC) superalloys derive their plastic deformation resistance primarily from the motion of dislocations in the face-centered cubic (FCC) γ matrix. Plasticity in FCC metals is governed by the activation of slip systems—specific combinations of crystallographic planes and directions—which minimize the energy required for dislocation motion.

The most closely packed atomic planes in the FCC lattice are the {111} family, while the shortest lattice vectors belong to the ⟨110⟩ family. This dense atomic configuration facilitates dislocation glide. The interplanar spacing for {111} planes is:

$$d_{111} = \frac{a}{\sqrt{3}} \tag{2.2}$$

and the Burgers vector magnitude for dislocations in the ⟨110⟩ direction is:

$$|\vec{b}| = \frac{a}{\sqrt{2}} \tag{2.3}$$

where a is the lattice constant. Figure 2.5 schematically illustrates these densely packed planes and directions.

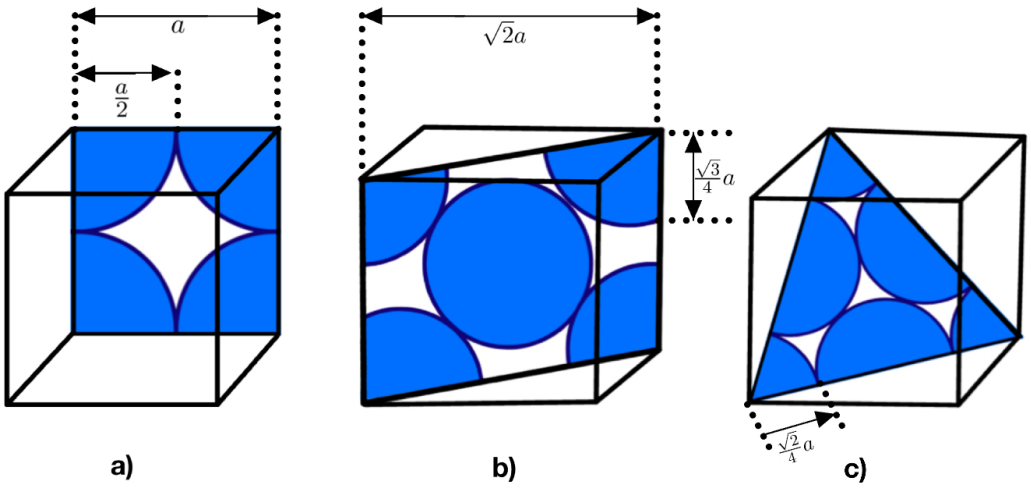

Figure 2.5: Most closely packed planes in FCC. (a) 100 Planes with Packing Density 79%. (b) 110 Planes with Packing Density 83%. (c)111 Planes with Packing Density 91%.

As a result, plastic slip in FCC crystals occurs most readily on {111} planes in ⟨110⟩ directions. This gives rise to 12 independent *octahedral slip systems*, which are the most active under typical loading conditions. However, at elevated temperatures—typically above 800°C—the activation of *cube slip systems* {100}⟨110⟩ becomes significant due to increased dislocation mobility and thermal energy as can ben seen from Figure 2.6 as a schematic[5, 3].

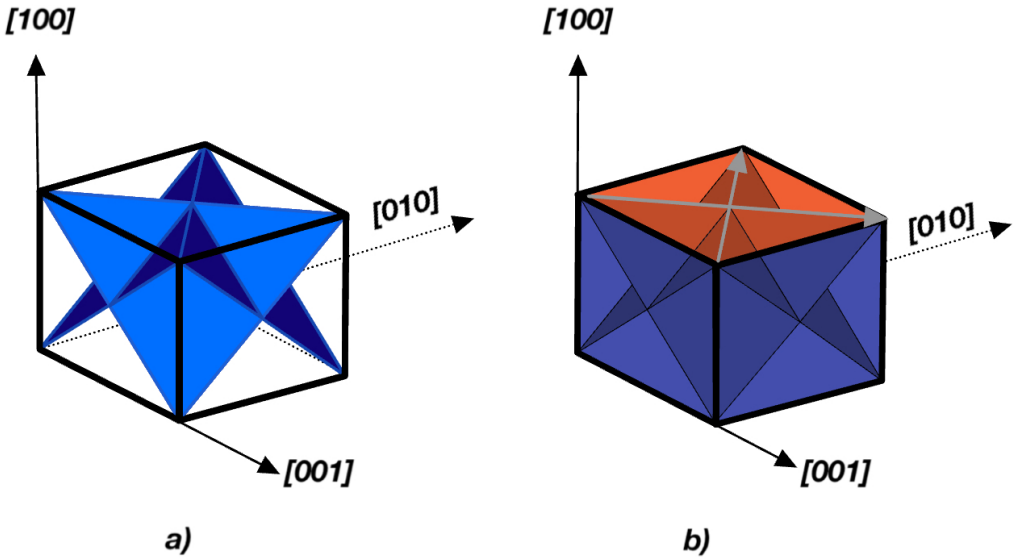

Figure 2.6: FCC Slip system schematic. (a) 111 Octahedral Slip Family. (b) 100 Cubic Slip Family

Dislocations move through the lattice as illustrated in Figure 2.7, where a dislocation line is shown gliding on a slip plane. This fundamental mechanism gives rise to localized surface slip traces, as seen in Figure 2.8, which reveals experimentally observed dislocation activity in a [001]-oriented crystal.

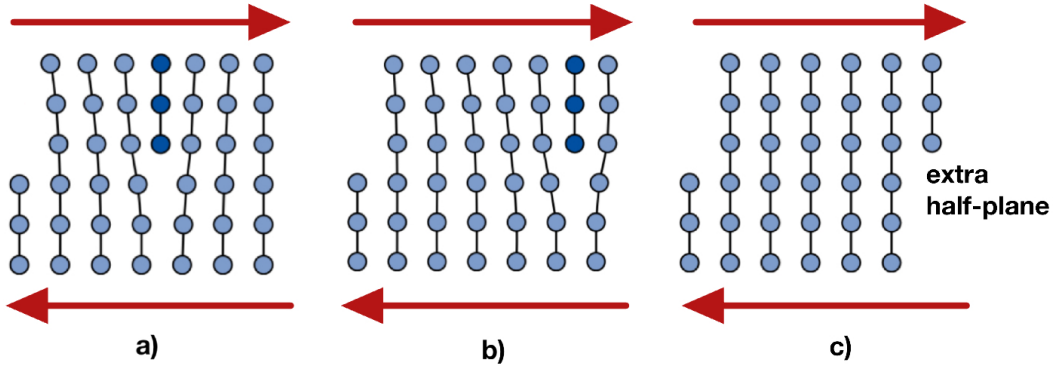

Figure 2.7: Schematic of an extra half plane (dislocation line) moving on a slip plane.

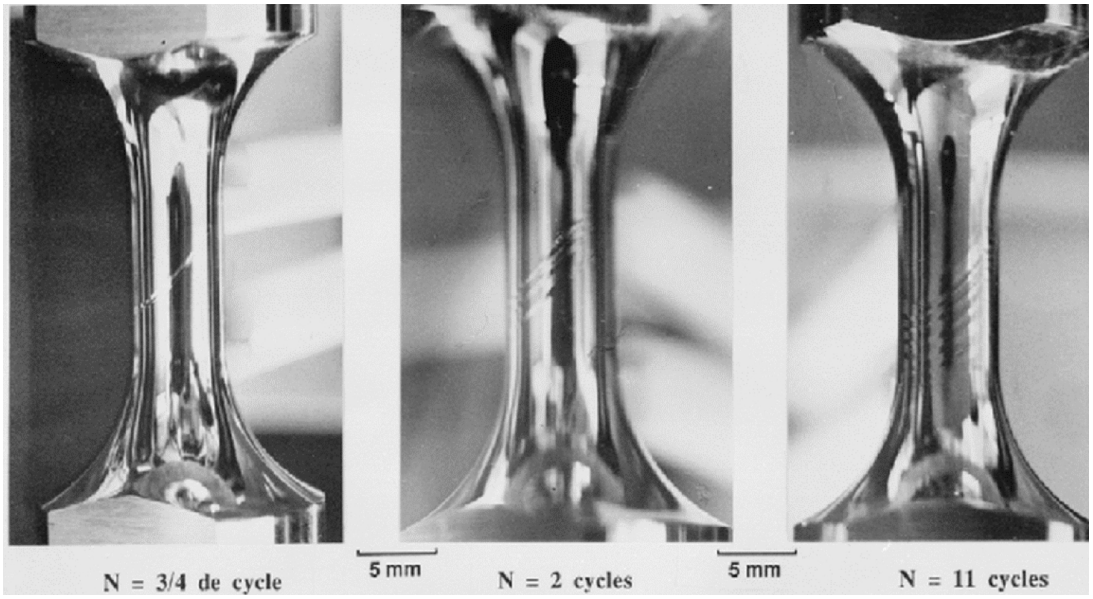

Figure 2.8: Anisotropic slip traces seemed on Single Crystal Nickel Base Superalloy Specimen. [30]

A full list of 18 crystallographic slip systems used in modeling (12 octahedral + 6 cube systems) is provided in Table 2.2.

Table 2.2: Octahedral and Cube Slip Systems in FCC Crystals

System Type	Slip Plane	Slip Direction
Octahedral	(111)	$[1\bar{0}1]$, $[011\bar{]}$, $[1\bar{1}0]$
Octahedral	$(\bar{1}11)$	[101], [011], $[1\bar{1}0]$
Octahedral	$(11\bar{1})$	[101], $[1\bar{0}1]$, [011]
Octahedral	$(\bar{1}\bar{1}\bar{1})$	[101], $[1\bar{0}1]$, $[011\bar{]}$
Cube	(100)	[011], $[01\bar{1}]$
Cube	(010)	[101], $[1\bar{0}1]$
Cube	(001)	[110], $[1\bar{1}0]$

2.2.2 Resolved Shear Stress and Schmid's Law

The initiation of slip on a given system depends on the resolved shear stress τ acting on the slip plane in the slip direction. This is governed by Schmid's Law:

$$\tau = \sigma \cos\phi \cos\lambda \tag{2.4}$$

where σ is the applied axial stress, ϕ is the angle between the loading axis and the slip plane normal, and λ is the angle between the loading axis and slip direction.

The product $\cos\phi\cos\lambda$ is the *Schmid factor*, and it determines which slip system becomes active first. For [001] single crystals, the maximum Schmid factor for octahedral slip systems is approximately 0.41.

Figure 2.9 illustrates the double projection that defines Schmid's law and shows how stress transforms into shear on crystallographic planes.

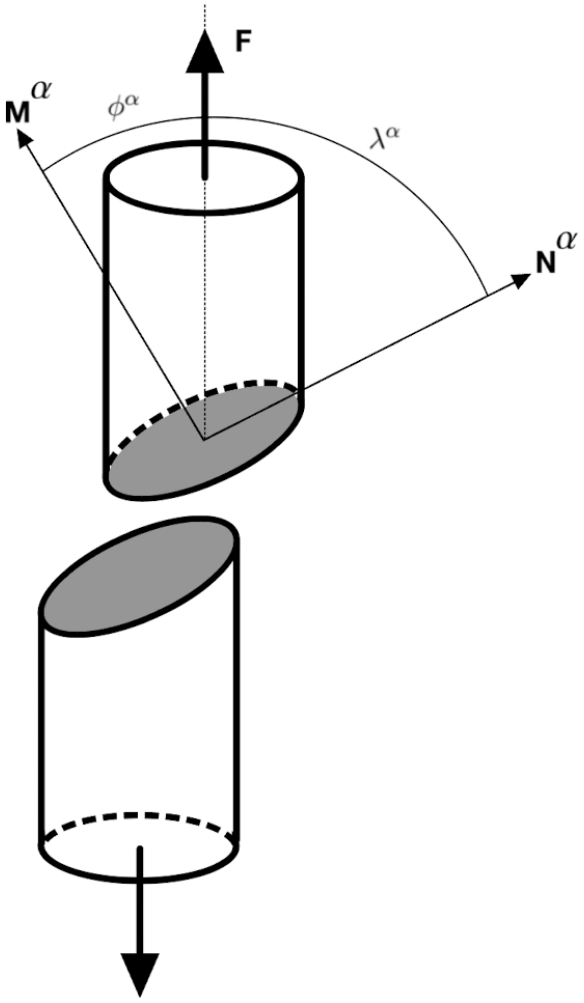

Figure 2.9: Schmid law showing resolved shear stress on slip plane for a tensile stress specimen.

2.3 Mechanical Properties of Nickel-Based Superalloys

Nickel-based superalloys exhibit outstanding mechanical performance across a wide range of service temperatures, particularly in demanding high-temperature applications such as gas turbines, aeroengines, and power generation systems. Their mechanical properties are strongly influenced by microstructural features, crystallographic orientation, chemical composition, and operating temperature. Single crystal (SC) variants eliminate grain boundary effects, enabling superior creep and fatigue resistance. This section provides an overview of their tensile, fatigue, and creep behavior based on experimentally observed trends.

2.3.1 Tensile Properties

- Nickel-based SC superalloys show strong anisotropy in their tensile behavior. The [001] orientation is typically aligned along the loading direction in turbine blades due to its balance between high tensile strength and good ductility [3].
- At room temperature, these materials exhibit a relatively high yield strength and moderate work hardening. As temperature increases, yield strength decreases gradually up to 600°C, followed by a plateau or slight increase, known as the *yield strength anomaly* [31, 32]. This effect is attributed to the cross-slip suppression of screw dislocations and the stability of γ' precipitates.
- Above 800°C, the mechanical strength drops significantly due to dislocation climb and increased mobility, though the γ' phase still provides strong resistance to deformation up to 1000–1100°C [33, 34].
- The orientation dependence of tensile strength is substantial: [001] crystals show the highest high-temperature strength due to symmetrical Schmid factors across active slip systems, while [011] and [111] orientations exhibit lower yield stress and reduced plastic stability [35, 36]. Brittle behavior is more likely in non-[001] orientations under multiaxial or fast transient loading.
- Ductility decreases with temperature as deformation becomes more localized, but SC alloys still retain reasonable plasticity at 1000°C in the [001] direction.

Elongation values vary between 2–6% depending on alloy composition and heat treatment [37, 38].

- Precipitate morphology and spacing—controlled by heat treatment—play a crucial role in tensile behavior. Finer, uniformly distributed γ' precipitates increase strength at intermediate temperatures by obstructing dislocation glide [39, 40].

- Fracture surfaces under tension typically exhibit dimpled morphologies consistent with microvoid coalescence. In certain cases, planar slip and interface decohesion contribute to premature failure in poorly oriented specimens or under overload conditions [41, 42].

2.3.2 Fatigue Behavior

Fatigue failure is one of the most critical damage mechanisms in nickel-based single crystal (SC) superalloys due to the cyclic thermal and mechanical loads experienced during turbine engine operation. These alloys are designed to operate near their melting temperature, where both low-cycle fatigue (LCF) and high-cycle fatigue (HCF) mechanisms may govern the component life depending on loading conditions. The fatigue resistance of these materials is governed by a range of factors including γ/γ' microstructure, crystallographic orientation, temperature, strain amplitude, and surface condition. This section presents a comprehensive view of the fatigue damage mechanisms, followed by detailed discussions on fatigue crack initiation and growth, based on extensive experimental studies.

2.3.2.1 Fatigue Damage Mechanisms

Fatigue damage can generally be classified into three fracture modes, schematically illustrated in Figure 2.10. Mode I corresponds to opening-mode fracture, Mode II to in-plane shear, and Mode III to tearing (out-of-plane shear). In metallic fatigue, crack propagation typically begins in Mode II (along crystallographic slip planes) and transitions to Mode I with increasing crack length or stress intensity.

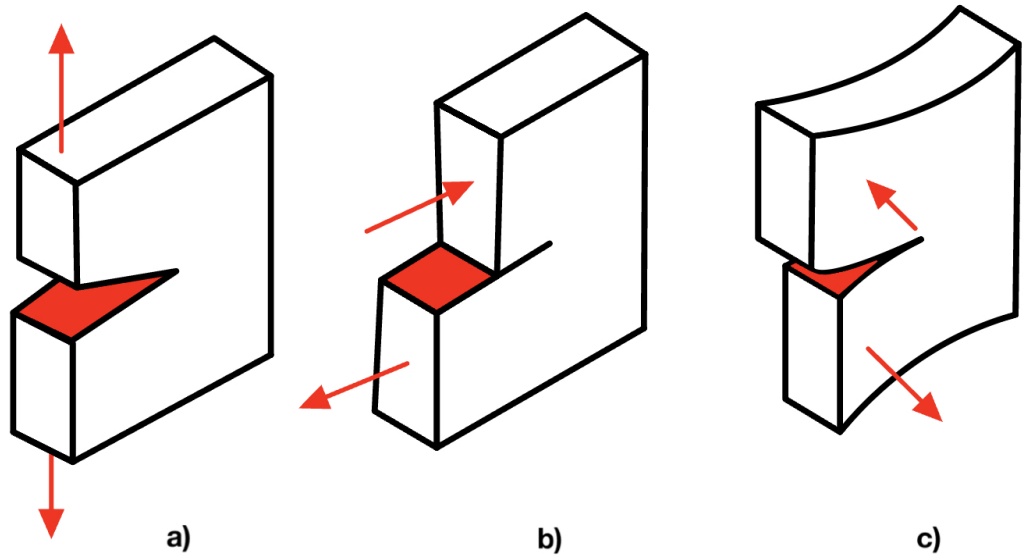

Figure 2.10: Damage Modes. a) Opening (Mode I). b) Shearing (Mode II). c) Tearing (Mode III).

Fatigue life (N_f) is defined as the number of cycles to failure under a specified cyclic load. It is typically separated into two regimes: crack initiation and stable crack propagation. The stable crack growth regime is most commonly described by the Paris law:

$$\frac{da}{dN} = C(\Delta K)^m \tag{2.5}$$

where $\frac{da}{dN}$ is the crack growth rate per cycle, ΔK is the range of stress intensity factor, and C and m are material constants. Figure 2.11 illustrates the characteristic crack growth curve with three stages: crystallographic growth (I), Paris regime (II), and final unstable propagation (III). For SC superalloys, ΔK_{th} values are typically in the range of 8–12 MPa $\sqrt{\text{m}}$ [43, 44, 45].

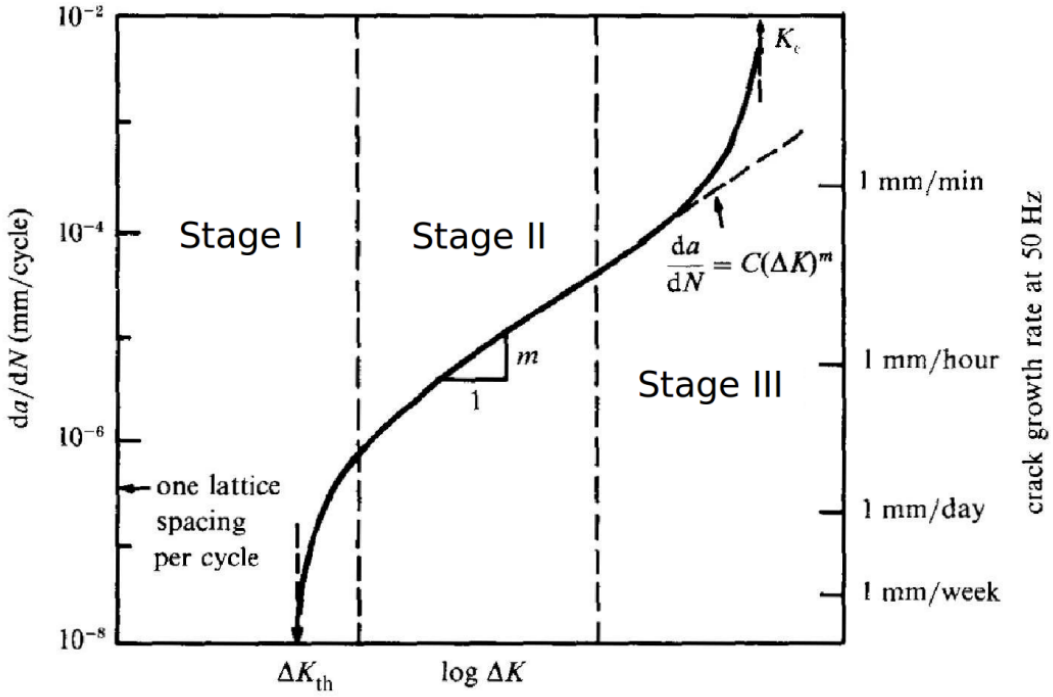

Figure 2.11: Crack growth behavior curve for most metallic materials. [43]

2.3.2.2 Fatigue Crack Initiation

Fatigue crack initiation in nickel-based SC superalloys depends on microstructural features, surface conditions, and environmental exposure. At high temperatures, surface oxidation, casting porosity, and creep interactions become significant contributors to damage accumulation [46, 47, 38].

Experimental SEM observations on CMSX-4 samples fatigued at 1050°C and $\Delta\epsilon_t$ = 0.9% reveal typical crack initiation sites (Figure 2.12). Cracks initiate at surface pores (a), oxidized regions (b), and propagate from these into the material (c). Rafted microstructures, oxidation-assisted mechanisms, and surface roughness accelerate the early stages of fatigue damage.

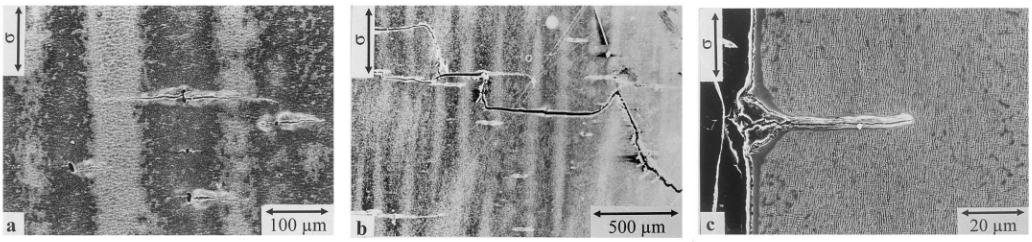

Figure 2.12: Fatigue crack initiation in CMSX-4 at 1050°C. [46]

Orientation affects both the local stress state and activation of slip systems. In [001]-oriented crystals, four octahedral slip systems can be equally activated, promoting homogeneous deformation and delaying crack initiation [48, 35, 36]. In [111] and [011] directions, fewer systems carry the majority of the strain, leading to localized plasticity, higher Schmid factors, and more rapid crack formation [49].

Temperature also governs crack initiation mechanisms. At room temperature, initiation often originates from carbides and microstructural inhomogeneities [41]. At elevated temperatures (¿800°C), oxidation accelerates crack formation and reduces resistance to plastic deformation [44, 37]. HIP-treated alloys show reduced porosity and improved fatigue life by eliminating early-stage initiation sites [50, 51].

2.3.2.3 Fatigue Crack Growth

Following initiation, fatigue cracks propagate through the matrix and across γ' precipitates. Crack growth mechanisms depend on stress intensity, microstructure, temperature, and environment. Figure 2.13 shows crack morphologies in CMSX-4 under different γ/γ' conditions: cuboidal precipitates (a–b), perpendicular rafting (c–d), and parallel rafting (e–f) [46]. Each morphology influences crack tortuosity and growth rate.

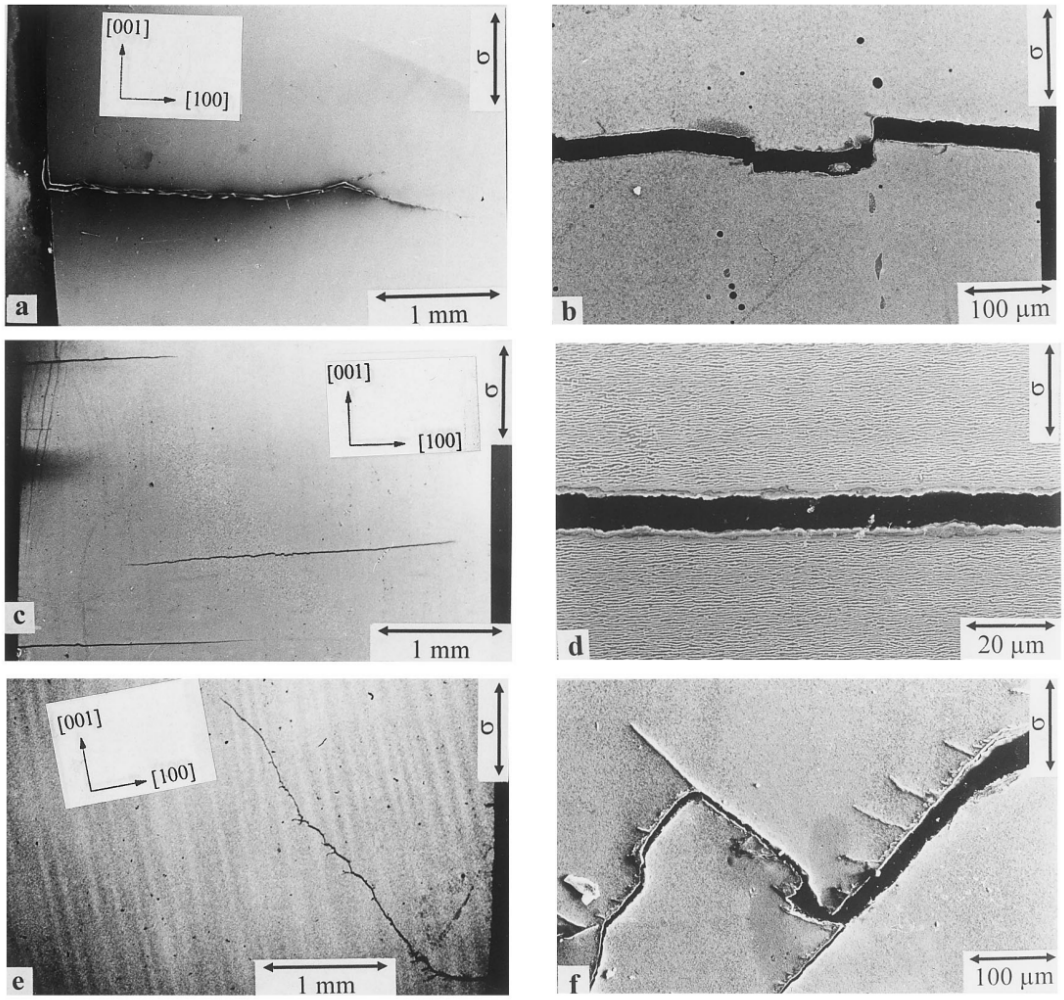

Figure 2.13: Fatigue crack propagation in CMSX-4 [46].

At lower ΔK, growth proceeds crystallographically along {111} planes (Stage I), especially in vacuum or inert atmospheres [44, 50]. In Stage II, growth is dominated by mode I mechanisms, perpendicular to applied load. Environmental effects become more severe at higher temperatures and lower frequencies: oxide-assisted propagation can dominate above 850°C [48, 33].

Orientation dependence persists in the growth regime. [001] specimens exhibit deflected or zigzag crack paths and lower da/dN rates due to multidirectional slip resistance [37, 38]. [011] and [111] crystals, in contrast, show more planar crack paths and higher rates due to limited active slip systems and lower work hardening [45, 51].

Surface oxidation also reduces threshold values and accelerates crack coalescence. Application of protective coatings (e.g., aluminides, MCrAlY) significantly improves fatigue life at high temperatures by delaying crack initiation and suppressing oxidation at the crack tip [52, 47].

Combined fatigue-creep interaction at high temperatures leads to microvoid formation near crack tips, and time-dependent growth. This is especially evident in trapezoidal waveforms or dwell-fatigue testing [44, 48, 32].

Thus, the fatigue resistance of SC nickel superalloys is maximized by [001] alignment, controlled γ' morphology, low defect content, and protective coatings—all of which reduce the severity of crack initiation and growth under cyclic loading.

2.3.3 Creep Behavior

Creep is the time-dependent deformation that occurs when a material is subjected to a constant load at elevated temperature, typically above 0.4 times its melting temperature. For nickel-based single crystal (SC) superalloys, which are often used near or above 1000°C, creep resistance is one of the most critical performance metrics, especially for turbine blade applications. The elimination of grain boundaries in SC alloys removes the grain boundary sliding mechanism dominant in polycrystalline alloys, significantly enhancing creep performance under uniaxial loading conditions.

The primary creep strengthening mechanism in these alloys is the ordered γ' phase, which forms a coherent precipitate with the disordered γ matrix. Dislocations must either shear through the γ' precipitates or bypass them through Orowan looping, both of which require high stress. The coherency between γ and γ' is crucial for retarding dislocation motion. Furthermore, at elevated temperatures, γ' rafting occurs—directional coarsening of γ' particles into plate-like structures aligned perpendicular or parallel to the applied stress—which influences creep resistance.

Creep in SC superalloys proceeds through three classical stages: primary (transient hardening), secondary (steady state), and tertiary (accelerated deformation).

The minimum creep rate during secondary creep, $\dot{\varepsilon}_{\min}$, is a key design parameter and is often expressed using a power-law creep equation:

$$\dot{\varepsilon}_{\min} = A\sigma^n \exp\left(\frac{-Q}{RT}\right) \tag{2.6}$$

where A is a model parameter, σ is applied stress, n is the stress exponent (typically 4–8 for SC alloys), Q is the activation energy for creep, R is the gas constant, and T is the temperature in Kelvin [31, 37].

Rafting behavior is strongly dependent on alloy composition, heat treatment, temperature, and orientation. For [001]-oriented crystals, the most common configuration in blades, rafting occurs perpendicular to the applied stress and helps block dislocation motion across the γ/γ' interface. This improves creep resistance over long periods [47, 40].

Creep-fatigue interaction is an important phenomenon, particularly under thermomechanical fatigue (TMF) conditions where a component experiences repeated loading at high temperatures. During dwell periods or slow cycling, time-dependent creep strain accumulates, contributing to crack initiation and accelerating crack growth. This synergy is especially detrimental at temperatures above 850°C and low loading frequencies [44, 48, 32].

Experimental studies have shown that crack tip creep relaxation leads to enhanced plastic zone size and accelerates interfacial decohesion in rafted structures. In particular, crack propagation in directionally rafted microstructures can be facilitated along the γ channels under tensile stress [46, 51].

Design strategies for improving creep resistance include increasing γ' volume fraction, optimizing Al/Ti ratios, alloying with refractory elements (e.g., Re, W, Ta), and tailoring heat treatment to refine precipitate morphology. Newer generations of SC superalloys (4th and 5th gen) exhibit outstanding creep life even beyond 1000°C due to such innovations [52].

In summary, the superior creep resistance of SC superalloys arises from their tailored microstructure, anisotropy, and controlled deformation mechanisms.

However, when creep interacts with fatigue—particularly in TMF regimes—lifing models must account for both strain amplitude and time-at-temperature effects, which are critical for accurate component life prediction.

2.4 Evolution of Nickel-Based Single Crystal Superalloys

The advancement of nickel-based single crystal (SC) superalloys has been a cornerstone in the development of high-performance turbine blades for aerospace and energy applications. These alloys exhibit superior creep resistance, fatigue life, and environmental stability at elevated temperatures, primarily due to the elimination of grain boundaries, optimization of the γ/γ' microstructure, and systematic alloying strategies across six generations. This section outlines the evolution of SC superalloys, with individual subsections dedicated to each generation.

2.4.1 First Generation: High γ' Volume Fraction, No Rhenium

First-generation SC superalloys, such as PWA 1480, René N4, and CMSX-2, were introduced in the late 1970s and early 1980s. These alloys aimed to maximize creep resistance by increasing the γ' precipitate content (up to 70% volume fraction) and optimizing its morphology. Key alloying elements included Al, Ti, Ta, W, and Cr, while avoiding rhenium (Re). The typical composition featured high Al+Ti content to stabilize the γ' phase and moderate levels of Cr for oxidation resistance.

The elimination of grain boundaries significantly enhanced creep life and fatigue resistance. However, oxidation resistance and castability remained challenges, addressed in part by Hf, C, and B additions. First-generation alloys established the foundational design principles of SC superalloys [3, 5].

2.4.2 Second Generation: Introduction of Rhenium (3%)

Second-generation alloys, such as CMSX-4, PWA 1484, and René N5, introduced 3 wt% rhenium to improve creep strength. Rhenium partitioned to the γ matrix and

reduced diffusion rates, thus delaying creep deformation. These alloys retained high γ' content while reducing Cr and modifying other elements to accommodate Re.

The addition of Re led to significant improvements in creep rupture life and high-temperature capability. CMSX-4, for instance, became widely used in commercial aerospace engines due to a balance of strength, stability, and castability. However, Re increased density and cost, prompting further optimization in subsequent generations [31, 40].

2.4.3 Third Generation: High Rhenium Content (6%) with TCP Risks

Third-generation SC superalloys, including CMSX-10 and René N6, doubled the Re content to 6 wt%, further enhancing creep strength. However, the increased Re and W content heightened the risk of topologically close-packed (TCP) phase formation, which can embrittle the alloy and degrade mechanical performance.

To mitigate this, Cr content was reduced (often to lower than 3%) and careful heat treatment schedules were developed. These alloys demonstrated exceptional creep performance up to 1100°C but required meticulous microstructural control to avoid TCP phase precipitation [5].

2.4.4 Fourth Generation: Introduction of Ruthenium (3%) for Phase Stability

Fourth-generation alloys, such as TMS-138 and EPM-102, added 3 wt% ruthenium alongside 6 wt% Re. Ruthenium improved phase stability by altering the partitioning behavior of Re and W, thereby suppressing TCP phase formation. These alloys also showed improved microstructural stability during long-term high-temperature exposure.

EPM-102, for example, achieved enhanced creep and fatigue resistance while maintaining structural integrity under aggressive thermal cycles. The generation marked a key advance in balancing strength with phase stability [47, 52].

2.4.5 Fifth Generation: Higher Ruthenium (5%) and Balanced Oxidation Resistance

Fifth-generation SC superalloys, such as TMS-196, pushed Ru content to 5 wt%, maintained high Re levels, and optimized Cr (4%) and Mo/W content. These adjustments enhanced oxidation resistance and hot corrosion behavior while preserving creep performance.

TMS-196 was shown to sustain creep at 1100°C for extended durations with improved environmental durability. The alloy design also focused on castability and microstructural stability, making it suitable for large turbine blade applications [52].

2.4.6 Sixth Generation: Advanced Creep and Oxidation Resistance

Sixth-generation alloys, exemplified by TMS-238, refined the fifth-generation composition by slightly reducing Mo and W, increasing Co and Ta, and maintaining high Ru and Re. The result was a well-balanced alloy offering excellent creep rupture strength and oxidation resistance.

TMS-238 achieved superior performance in oxidation and hot corrosion tests compared to earlier generations, while maintaining similar or better creep properties. This generation reflects the culmination of decades of alloy design, balancing mechanical and environmental properties for next-generation aerospace engines [52].

2.5 Concluding Remarks

Nickel-based single crystal (SC) superalloys have evolved over the past four decades into one of the most advanced classes of structural materials, particularly in high-temperature aerospace applications. Their remarkable ability to retain mechanical strength, resist creep deformation, and maintain oxidation and corrosion resistance at temperatures approaching 1100°C has enabled substantial increases in gas turbine efficiency and engine lifetime.

The superior performance of SC superalloys originates from their unique microstructural features—most notably the ordered γ' phase embedded within a disordered γ matrix—and the elimination of grain boundaries, which suppresses common failure mechanisms such as grain boundary sliding and creep cavitation. The progression from first- to sixth-generation alloys has seen the incremental introduction of potent refractory elements such as rhenium and ruthenium, the fine-tuning of chromium and molybdenum contents to balance environmental resistance, and ongoing suppression of topologically close-packed (TCP) phases. These developments have been strategically aligned with the performance needs of increasingly demanding engine environments.

In this chapter, the physical metallurgy of SC superalloys was examined in detail, including their compositional design, microstructural evolution, mechanical response under tensile, fatigue, and creep loading, and the role of deformation mechanisms such as dislocation motion and phase rafting. The fatigue and creep behavior—critical for life-limited components like turbine blades—were analyzed with special emphasis on orientation dependence, temperature effects, and fatigue–creep interactions.

Furthermore, the historical evolution of SC alloy design was reviewed across six generations, showcasing how alloying innovations and microstructural engineering have enabled these materials to meet ever-rising temperature and performance requirements.

As the next frontier of superalloy design emerges, further breakthroughs are expected to come from combinatorial alloy optimization, machine learning-assisted discovery, and integration with advanced processing methods such as additive manufacturing. Nonetheless, the foundational understanding of the physical metallurgy and deformation mechanisms of single crystal nickel-based superalloys remains essential for both academic study and industrial application.

CHAPTER 3

Modeling of Single Crystals

3.1 Introduction to Crystal Plasticity

3.1.1 Background and Motivation

The theory of crystal plasticity originates from early 20th-century observations of anisotropic deformation in single crystals. Initial mechanical testing by Taylor and Elam revealed that the yielding and flow behavior of metallic crystals depend significantly on crystallographic orientation, leading to the foundational concept of crystallographic slip as the primary mode of plastic deformation. This concept was fundamentally advanced in 1934, when Orowan, Polanyi, and Taylor independently introduced the theory of dislocations as line defects in the crystal lattice, explaining how plastic deformation can occur at stresses significantly lower than theoretical shear strengths of perfect crystals [53].

Following these early discoveries, the mid-20th century saw the formal development of constitutive models describing multislip plasticity. Hill's generalization of the plastic behavior of single crystals under multiaxial stress states represented a significant leap forward, capturing anisotropic yielding based on the activation of multiple crystallographic slip systems [54]. These early models, typically formulated in terms of critical resolved shear stress (CRSS) and kinematic constraints, laid the groundwork for modern crystal plasticity constitutive laws.

The advent of finite element methods (FEM) in structural mechanics offered a powerful computational tool for solving complex boundary value problems. Peirce, Asaro,

and Needleman pioneered the first crystal plasticity finite element (CPFE) simulations in 1982, employing a rate-dependent formulation to model large-strain single crystal plasticity [55]. This formulation incorporated crystallographic kinematics, orientation evolution, and slip system-level hardening, making it a foundational model for later computational implementations. As computational resources expanded, Becker was among the first to implement full 3D CPFE simulations using all twelve FCC slip systems [56]. These efforts marked the emergence of CPFE as a robust multiscale modeling platform, enabling simulations that connect microstructural mechanics to macroscopic responses.

The primary motivation behind the development and use of crystal plasticity theory lies in its ability to capture the inherent mechanical anisotropy of crystalline solids. Unlike classical isotropic plasticity models, which abstract material behavior into scalar measures, crystal plasticity recognizes that the stress-strain response, hardening behavior, and deformation-induced texture are tensorial and orientation-dependent [57]. This orientation sensitivity is vital in applications involving textured polycrystals, single crystals, or components with complex loading conditions, where predictions of anisotropic yield, strain localization, and microstructure evolution are essential for accurate modeling and life assessment.

3.1.2 Scope and Applications in Single Crystal Superalloys

Crystal plasticity theory has found significant application in modeling the mechanical behavior of single crystal nickel-based superalloys, which are widely used in high-temperature turbine components such as blades and vanes. These materials, engineered for optimal performance in aggressive thermomechanical environments, are directionally solidified or cast as single crystals to eliminate grain boundaries, thus enhancing creep resistance and fatigue life [3].

In single crystal superalloys, plastic deformation is governed almost entirely by dislocation motion along specific slip systems in the FCC γ matrix and γ' precipitates. Crystal plasticity models are uniquely capable of simulating this behavior by representing the underlying physics of slip system activation and resistance. In the context of the CPFE method, these constitutive models are embedded within finite

element simulations of components subjected to complex thermal and mechanical loading. This allows for the resolution of microscale phenomena, such as slip localization and lattice rotation, which are critical to understanding component-level performance [57].

For example, turbine blades are commonly oriented with a [001] axis aligned along the loading direction to exploit the high strength of this orientation. CPFE simulations have been instrumental in predicting stress concentrations near geometric discontinuities (e.g., cooling holes, blade roots), identifying the active slip systems under service conditions, and estimating local strain accumulation that may lead to damage initiation [59, 58]. Such simulations aid in optimizing component design and evaluating the mechanical integrity under operational constraints.

3.1.3 Fatigue Behavior and the Role of Crystal Plasticity Models

Fatigue failure, particularly under cyclic thermomechanical loading, is a critical mode of damage in single crystal components exposed to high-temperature service environments. Traditional fatigue models often lack microstructural resolution and fail to account for the crystallographic nature of fatigue crack initiation. Crystal plasticity models address this gap by providing a physically based description of how cyclic slip accumulates on specific crystallographic systems, leading to persistent slip bands, surface roughening, and ultimately, crack nucleation [60].

Under cyclic loading, CPFE simulations can track the evolution of internal variables such as backstress, accumulated slip, and lattice orientation. These variables are essential for capturing the Bauschinger effect, cyclic hardening/softening, and ratcheting behavior. More advanced models integrate dislocation density-based formulations to link microstructural evolution with macroscopic fatigue response, enabling more accurate predictions of fatigue life and damage localization [61].

For instance, Zhang et al. employed a CPFE model to simulate low-cycle fatigue in a nickel-based single crystal superalloy, capturing orientation-dependent cyclic plasticity and identifying the critical slip systems responsible for crack initiation [62]. The predicted fatigue damage sites showed excellent agreement with experimental

observations of surface slip traces and crack paths. Additionally, environmental effects such as oxidation-assisted damage have been incorporated into crystal plasticity models, allowing for the simulation of oxidation-fatigue interactions, which are particularly relevant for turbine components operating at elevated temperatures [63].

From a design perspective, CPFE-based fatigue models enable the microstructurally informed prediction of fatigue initiation life and support the optimization of materials and geometries to enhance durability. These models form a crucial link between fatigue testing and in-service performance, offering a predictive capability that is grounded in the physics of crystallographic deformation mechanisms.

3.2 Crystal Plasticity Theory

The crystal plasticity model presented in this work is formulated within the framework of finite strain continuum mechanics and adheres strictly to the principles of thermodynamics. The total deformation of a crystalline solid is decomposed into elastic and plastic components, and the internal dissipation is governed by thermodynamically admissible flow rules. The theory is developed using the Helmholtz free energy potential and rate-dependent viscoplasticity.

The first law of thermodynamics, expressed as the balance of internal energy, is given by

$$\rho \dot{e} = \boldsymbol{\sigma} : \nabla \mathbf{v} - \nabla \cdot \mathbf{q} + \rho r \tag{3.1}$$

where:

- ρ: mass density,
- e: specific internal energy,
- $\boldsymbol{\sigma}$: Cauchy stress tensor,
- $\mathbf{v}$: velocity field,
- $\mathbf{q}$: heat flux,
- r: internal heat generation per unit mass.

The second law is imposed via the Clausius–Duhem inequality:

$$\rho \dot{s} + \nabla \cdot \left(\frac{\mathbf{q}}{T} \right) - \frac{\rho r}{T} \geq 0 \tag{3.2}$$

Introducing the Helmholtz free energy $\psi = e - Ts$, and assuming isothermal conditions, the inequality becomes

$$\rho \dot{\psi} - \boldsymbol{\sigma} : \nabla \mathbf{v} \leq 0 \tag{3.3}$$

This inequality ensures that the rate of change of free energy does not exceed the mechanical power input, thus enforcing dissipative behavior. The specific form of the free energy ψ, defined per unit reference volume, includes contributions from elastic strain and internal variables:

$$\psi = \frac{1}{2} \boldsymbol{E}^e : \mathbb{C} : \boldsymbol{E}^e + \sum_{\alpha=1}^{N} h_0 \rho^\alpha + \sum_{\alpha=1}^{N} r_0 \gamma^\alpha \tag{3.4}$$

Here, $\boldsymbol{E}^e = \frac{1}{2} \ln(\mathbf{C}^e)$ is the elastic logarithmic strain derived from the elastic right Cauchy–Green tensor $\mathbf{C}^e = \mathbf{F}^{eT} \mathbf{F}^e$, $\mathbb{C}$ is the fourth-order elasticity tensor, ρ^α is the isotropic hardening variable, γ^α is the accumulated slip, and h_0, r_0 are material constants.

The second Piola–Kirchhoff stress tensor is obtained from the energy potential as

$$\mathbf{S} = \frac{\partial \psi}{\partial \boldsymbol{E}^e} = \mathbb{C} : \boldsymbol{E}^e \tag{3.5}$$

which defines the hyperelastic response of the crystal.

For materials with cubic symmetry such as Ni-based FCC crystals, the stiffness tensor $\mathbb{C}$ has only three independent components C_{11}, C_{12}, C_{44}. In Voigt notation, the elastic tensor is written as:

$$\mathbb{C} = \begin{bmatrix} C_{11} & C_{12} & C_{12} & 0 & 0 & 0 \\ C_{12} & C_{11} & C_{12} & 0 & 0 & 0 \\ C_{12} & C_{12} & C_{11} & 0 & 0 & 0 \\ 0 & 0 & 0 & C_{44} & 0 & 0 \\ 0 & 0 & 0 & 0 & C_{44} & 0 \\ 0 & 0 & 0 & 0 & 0 & C_{44} \end{bmatrix}$$

The moduli are related to isotropic constants via:

$$C_{11} = \frac{1}{3}(3K + 4\mu), \quad C_{12} = \frac{1}{3}(3K - 2\mu), \quad C_{44} = \mu + \mu'$$

where K is the bulk modulus, μ is the shear modulus, and μ' is an additional shear anisotropy parameter.

The total deformation gradient $\mathbf{F}$ is decomposed multiplicatively into elastic and plastic parts:

$$\mathbf{F} = \mathbf{F}^e \mathbf{F}^p \tag{3.6}$$

where $\mathbf{F}^p$ represents the plastic deformation due to crystallographic slip, and $\mathbf{F}^e$ captures elastic lattice distortion and rotation. Assuming plastic flow is volume-preserving, we have

$$\det(\mathbf{F}^p) = 1 \tag{3.7}$$

The velocity gradient $\mathbf{L} = \dot{\mathbf{F}}\mathbf{F}^{-1}$ becomes

$$\mathbf{L} = \mathbf{L}^e + \mathbf{F}^e \mathbf{L}^p \mathbf{F}^{e^{-1}}, \qquad \mathbf{L}^p = \dot{\mathbf{F}}^p \mathbf{F}^{p^{-1}} \tag{3.8}$$

with the symmetric and skew-symmetric parts of $\mathbf{L}^p$ denoted as

$$\mathbf{D}^p = \mathrm{sym}(\mathbf{L}^p), \qquad \mathbf{W}^p = \mathrm{skw}(\mathbf{L}^p)$$

Assuming irrotational and incompressible plastic flow leads to:

$$\mathbf{W}^p = 0, \qquad \mathrm{tr}(\mathbf{D}^p) = 0, \qquad \dot{\mathbf{F}}^p = \mathbf{D}^p \mathbf{F}^p \tag{3.9}$$

Plastic deformation in crystals is governed by the activity of crystallographic slip systems. The plastic strain rate tensor is expressed as the sum of slip system contributions:

$$\mathbf{D}^p = \sum_{\alpha=1}^{N} \dot{\gamma}^\alpha \, \mathbf{m}^\alpha \otimes \mathbf{n}^\alpha \tag{3.10}$$

where $\dot{\gamma}^\alpha$ is the shear rate on system α, $\mathbf{m}^\alpha$ is the slip direction, and $\mathbf{n}^\alpha$ is the normal to the slip plane.

The resolved shear stress on each slip system is obtained by projecting the stress tensor onto the corresponding Schmid tensor:

$$\tau^\alpha = \mathbf{S} : (\mathbf{m}^\alpha \otimes \mathbf{n}^\alpha) \tag{3.11}$$

A viscoplastic flow rule governs the evolution of slip on each system:

$$\dot{\gamma}^\alpha = \left\langle \frac{|\tau^\alpha| - r^\alpha}{K} \right\rangle^n \mathrm{sign}(\tau^\alpha) \tag{3.12}$$

where r^α is the slip resistance, K is a viscosity parameter, and n is the strain rate sensitivity exponent. The Macaulay brackets ensure plastic flow occurs only when the resolved shear stress exceeds the slip resistance.

The slip resistance evolves according to a nonlinear isotropic hardening law:

$$r^\alpha = r_0 + q \sum_{\beta=1}^{N} h^{\alpha\beta} \left(1 - \exp(-b|\gamma^\beta|)\right) \tag{3.13}$$

Here, r_0 is the initial yield stress, q is a saturation strength, b is a material parameter controlling the saturation rate, and $h^{\alpha\beta}$ is the latent hardening matrix that captures interaction between slip systems. For Ni-based single crystals, latent hardening is typically weak, and $h^{\alpha\beta} = \delta^{\alpha\beta}$ is often assumed [64, 65, 66, 67, 68].

3.2.1 Implicit Time Integration of Plastic Slip

The internal variable evolution in finite strain crystal plasticity is governed by a set of coupled, nonlinear ordinary differential equations associated with each active slip system. These equations arise from the viscoplastic flow rule and isotropic hardening relations, and are integrated over a time step $[t_n, t_{n+1}]$ using a fully implicit (backward Euler) scheme. Given the time increment $\Delta t = t_{n+1} - t_n$, the evolution equation for each slip system $\alpha \in [1, N]$ is

$$\Delta\gamma^{(\alpha)} = \Delta t \cdot \left\langle \frac{|\tau^{(\alpha)}| - r^{(\alpha)}}{K} \right\rangle^n \operatorname{sign}(\tau^{(\alpha)}). \tag{3.14}$$

To solve this system, we define the residual vector $\mathbf{R} \in \mathbb{R}^N$ as:

$$R^{(\alpha)} = \Delta\gamma^{(\alpha)} - \Delta t \cdot \left\langle \frac{|\tau^{(\alpha)}| - r^{(\alpha)}}{K} \right\rangle^n \operatorname{sign}(\tau^{(\alpha)}) \tag{3.15}$$

where the resolved shear stress is

$$\tau^{(\alpha)} = \mathbf{S} : (\mathbf{m}^{(\alpha)} \otimes \mathbf{n}^{(\alpha)}) \tag{3.16}$$

and the slip resistance is defined via an exponential isotropic hardening law:

$$r^{(\alpha)} = r_0 + q \sum_{\beta=1}^{N} h^{\alpha\beta} \left(1 - \exp(-b|\gamma^{(\beta)}|)\right) \tag{3.17}$$

3.2.2 Newton–Raphson Solver and Jacobian Derivation

To solve the nonlinear system $\mathbf{R}(\boldsymbol{\Delta\gamma}) = \mathbf{0}$, a Newton–Raphson scheme is used. The update formula is:

$$\boldsymbol{\Delta\gamma}^{(k+1)} = \boldsymbol{\Delta\gamma}^{(k)} - \mathbf{J}^{-1} \cdot \mathbf{R}^{(k)} \tag{3.18}$$

where $\mathbf{J} \in \mathbb{R}^{N\times N}$ is the Jacobian matrix:

$$J_{\alpha\beta} = \frac{\partial R^{(\alpha)}}{\partial \Delta\gamma^{(\beta)}} \tag{3.19}$$

Each Jacobian entry has two contributions:

- The sensitivity of the resolved shear stress $\tau^{(\alpha)}$ to a change in slip $\Delta\gamma^{(\beta)}$, which involves differentiating the stress through its dependence on the elastic strain $\boldsymbol{E}^e$.
- The sensitivity of the hardening function $r^{(\alpha)}$ with respect to $\gamma^{(\beta)}$, expressed as:

$$\frac{\partial r^{(\alpha)}}{\partial \gamma^{(\beta)}} = qh^{\alpha\beta} b \exp(-b|\gamma^{(\beta)}|) \cdot \text{sign}(\gamma^{(\beta)}) \tag{3.20}$$

Putting it together, the Jacobian becomes:

$$J_{\alpha\beta} = \delta_{\alpha\beta} - \Delta t \cdot n \cdot \left(\frac{f^{(\alpha)}}{K}\right)^{n-1} \left[\text{sign}(\tau^{(\alpha)}) \cdot \frac{\partial \tau^{(\alpha)}}{\partial \Delta\gamma^{(\beta)}} - \frac{\partial r^{(\alpha)}}{\partial \Delta\gamma^{(\beta)}}\right] \tag{3.21}$$

where $f^{(\alpha)} = |\tau^{(\alpha)}| - r^{(\alpha)}$ is the yield function value.

After convergence:

- Update $\gamma^{(\alpha)}_{n+1} = \gamma^{(\alpha)}_n + \Delta\gamma^{(\alpha)}$,
- Update hardening $\rho^{(\alpha)} = 1 - \exp(-b|\gamma^{(\alpha)}|)$,
- Compute plastic velocity gradient $\mathbf{D}^p = \sum_\alpha \dot{\gamma}^{(\alpha)} \mathbf{m}^{(\alpha)} \otimes \mathbf{n}^{(\alpha)}$,
- Update $\mathbf{F}^p$ using the exponential map,
- Compute $\mathbf{F}^e = \mathbf{F} \cdot (\mathbf{F}^p)^{-1}$,
- Use spectral decomposition to extract $\mathbf{U}^e$ and compute logarithmic strain $\boldsymbol{E}^e$,

- Finally, evaluate $\mathbf{S} = \mathbb{C} : \boldsymbol{E}^e$.

Convergence is achieved when:

$$\max |R^{(\alpha)}| < \varepsilon. \tag{3.22}$$

This concludes the return mapping scheme for the Gauss point-level crystal plasticity update.

3.3 Model Verification

3.3.1 Introduction

Verifying a constitutive model is an essential step in ensuring that it behaves consistently with known physical principles and theoretical predictions. In the case of single crystal plasticity, model verification is particularly important due to the directional nature of slip and the role of crystallographic anisotropy in shaping the material response.

In this section, the developed crystal plasticity model is tested against two benchmark problems. The first involves a compact tension (CT) specimen under plane strain conditions, where the results are compared to Rice's analytical crack tip solution for ideally plastic single crystals. This provides a direct test of the model's ability to reproduce expected shear band orientations and localization behavior. The second verification case examines the model's response under combined tension–torsion loading, where multiple slip systems are activated and the evolution of anisotropic plastic flow can be observed.

Together, these cases offer a clear and controlled setting to evaluate the model's fidelity before applying it to more complex fracture and damage problems.

3.3.2 CT Specimen Geometry and Material Parameters

The first verification case is based on a compact tension (CT) specimen under plane strain conditions, representative of classical fracture mechanics experiments. The goal

of this configuration is to evaluate whether the implemented crystal plasticity model can capture the directional strain localization predicted analytically by Rice [69] in a crystallographically oriented single crystal.

The geometry of the CT specimen is illustrated in Figure 3.1. It consists of a 40 mm $\times$ 40 mm square plate with two pin holes of 4 mm radius. A 10 mm notch is cut vertically from the lower edge, and an 18 mm long pre-crack extends horizontally from the notch tip. The upper pin hole is subjected to a vertical tensile load F, while the lower one is clamped to prevent displacement. This asymmetric loading induces crack opening and plastic flow concentrated at the crack tip. The red rectangle highlights the central region where detailed stress and strain fields are evaluated through mesh refinement and post-processing.

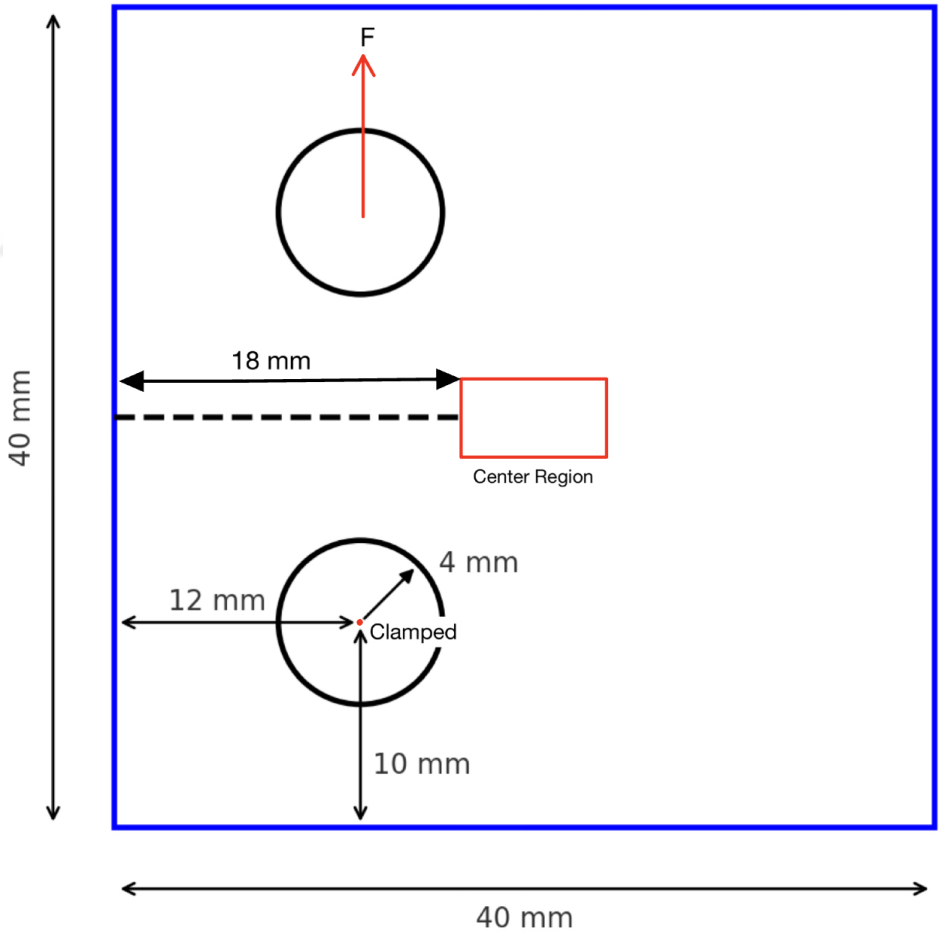

Figure 3.1: CT specimen geometry and dimensions.

A close-up view of the meshed central region is shown in Figure 3.2. The mesh is highly refined near the crack tip to resolve steep stress gradients and accurately track the formation of strain localization bands. The lower horizontal edge, marked in blue, corresponds to the crack plane and midline of the specimen. Symmetry boundary conditions are enforced along the right-hand half of this line, while the left-hand half is traction-free, allowing the crack to open. Due to the loading applied via the upper pin hole and the fixed lower support, the central region undergoes an effective rotational deformation, as shown by the green arrow. This rotation mimics the physical loading path observed in CT tests and contributes to the complex activation of slip systems in the vicinity of the crack tip.

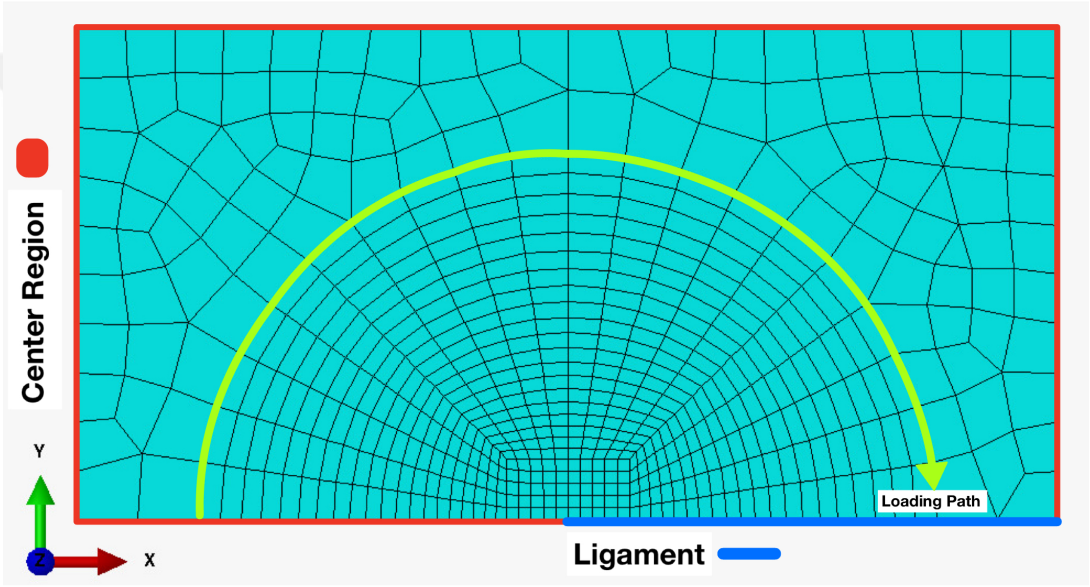

Figure 3.2: Finite Element Mesh of Center Region of the CT Specimen.

All simulations are conducted under plane strain conditions to remain consistent with the assumptions of Rice's analytical solution. The material used in the simulations is CMSX-4, a second-generation Ni-based single crystal superalloy. The crystal plasticity model accounts for twelve octahedral and six cube slip systems. Octahedral slip is considered the primary deformation mechanism, while cube slip remains inactive under most conditions unless explicitly triggered by loading.

The elastic response assumes cubic symmetry. Viscoplastic flow is modeled using a rate-dependent formulation with no isotropic hardening. A nonlinear kinematic

hardening rule governs the evolution of backstress, allowing for directional hardening and the development of Bauschinger-like effects. The material parameters for CMSX-4, used in this section, are listed in Table 3.1.

Table 3.1: Crystal plasticity parameters for CMSX-4 used in CT specimen simulations.

Slip System	K [MPa$^{1/n}$]	n	r_0 [MPa]	q [MPa]	b	c [MPa]	d [MPa]
Octahedral	551.3	7.8	108.1	–	–	163514.9	1821.5
Cubic	541.0	7.8	36.8	–4.7	5400.5	97189.9	1879.4

3.3.3 Rice's Analytical Solution

To verify the accuracy of the strain localization patterns predicted by the crystal plasticity model, we refer to the analytical crack-tip solution developed by Rice [69] for anisotropic ideally plastic single crystals. This asymptotic solution provides a piecewise-constant stress field in the vicinity of a stationary crack under plane strain conditions, and serves as a rigorous benchmark for assessing the model's ability to capture crystallographically driven localization.

In this work, we focus on the (001)[110] crack orientation in an FCC crystal, where the crack plane lies normal to the [001] direction and propagates along the [110] direction. Plane strain is imposed in the (x_1, x_2) plane, where $x_1 \parallel [110]$ and $x_2 \parallel [001]$, consistent with the configuration described in the CT specimen (Figure 3.3). The crack tip is located at the origin of this coordinate system.

Effective Slip Systems and Sectoral Fields

Plastic flow in Rice's theory is governed by Schmid's law:

$$\tau^s = \boldsymbol{\sigma} : \mathbf{m}^s = \tau_c \tag{3.23}$$

where τ^s is the resolved shear stress, τ_c is the critical resolved shear stress, and $\mathbf{m}^s$ is the symmetric Schmid tensor defined by:

$$\mathbf{m}^s = \tfrac{1}{2}\left(\mathbf{l}^s \otimes \mathbf{n}^s + \mathbf{n}^s \otimes \mathbf{l}^s\right) \tag{3.24}$$

In the (001)[110] configuration, three effective slip system directions are sufficient to maintain plastic plane strain flow: 54.7°, 90°, and 125.3°, measured from the crack plane. These directions correspond to slip system pairs such as (111)[101], (111)[011] and their symmetric variants. The angular sectors separated by these directions are each associated with a unique, constant stress state.

Table 3.2: Effective slip systems and associated constant stress states in each sector for the (001)[110] crack orientation.

Sector	**Angle Range**	**Effective Slip System(s)**	σ_{11}	σ_{22}	σ_{12}
A	0°–54.7°	(111)[101], (111)[011]	$2\sqrt{6}\tau_c$	$3\sqrt{6}\tau_c$	0
B	54.7°–90°	same as A	$\frac{3}{2}\sqrt{6}\tau_c$	$2\sqrt{6}\tau_c$	$-\sqrt{3}\tau_c$
C	90°–125.3°	$(\bar{1}11)[101]$, $(\bar{1}11)[011]$	$\frac{3}{2}\sqrt{6}\tau_c$	$\sqrt{6}\tau_c$	$-\sqrt{3}\tau_c$
D	125.3°–180°	same as C	$\sqrt{6}\tau_c$	0	0

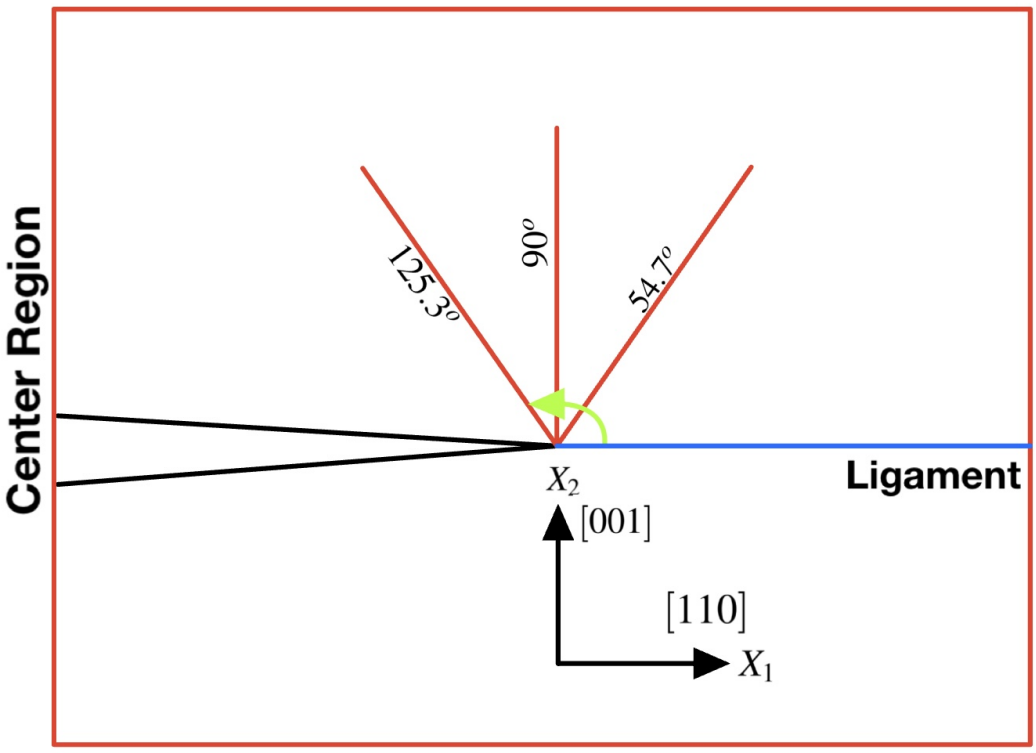

Figure 3.3: Rice's theoretical shear band directions for the (001)[110] orientation at the near crack tip.

Yield Surface and Discontinuity Lines

The activated effective slip systems define a hexagonal yield surface in the stress space $\left(\frac{\sigma_{11}-\sigma_{22}}{2}, \sigma_{12}\right)$. Each segment of this hexagon corresponds to an active slip direction, and the solution jumps from vertex to vertex across stress discontinuities. These jumps are constrained by traction continuity across sector boundaries:

$$[\![\sigma_{\alpha\beta}]\!]e'_\beta = 0 \quad \text{or} \quad [\![\sigma_{\alpha\lambda}]\!] = e_\alpha e_\lambda [\![\sigma_{11} + \sigma_{22}]\!]$$

leading to the piecewise-constant field given in Table 3.2. The corresponding yield surface is shown in Figure 3.4.

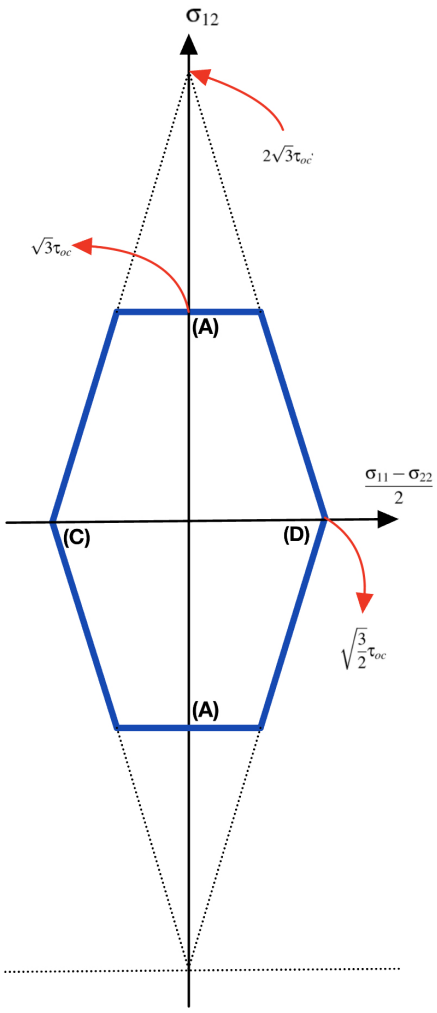

Figure 3.4: Hexagonal yield surface associated with effective slip systems for (001)[110] orientation. Each side corresponds to activation of a slip direction.

Slip and Kink Band Interpretation

The discontinuity lines predicted in Rice's solution correspond to angular boundaries across which the stress tensor exhibits a finite jump. These discontinuities manifest physically as either *slip bands* or *kink bands*, depending on the crystallographic alignment of the slip system involved.

In the case of the (001)[110] crack orientation, the inclined bands at $\theta = 54.7°$ and 125.3° are aligned both with the slip plane trace and the slip direction of the active slip systems. This crystallographic alignment allows the crystal to accommodate deformation through simple shear, and these bands are thus interpreted as *slip bands*. The vertical band at $\theta = 90°$, however, results from a symmetric double-slip configuration. The effective shear direction in this case is not aligned with any crystallographic plane, leading to out-of-plane distortions and lattice rotation. Consequently, this central band is identified as a *kink band*.

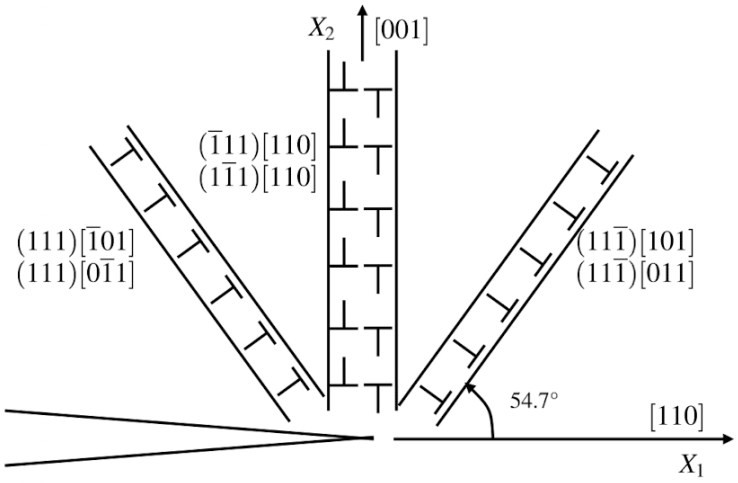

Figure 3.5: Discontinuity lines and localization structure for the (001)[110] crack orientation. Inclined bands are slip bands; the vertical band is a kink band. [70].

For the (110)[001] orientation, the situation is reversed due to symmetry. While the angular structure remains unchanged under plane strain, the crystallographic alignment of the active slip systems is different. The vertical discontinuity at $\theta = 90°$ is now aligned with both the slip direction and the slip plane trace of the active systems, allowing deformation via single slip. This makes it a slip band.

On the other hand, the inclined discontinuities at 54.7° and 125.3° lack this alignment and result in lattice rotation, and are thus identified as kink bands.

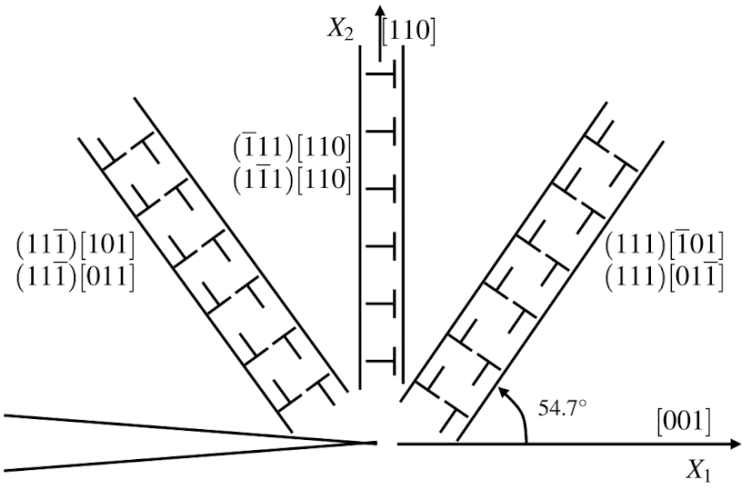

Figure 3.6: Discontinuity lines and localization structure for the (110)[001] crack orientation. The vertical band is now a slip band; inclined bands are kink bands. [70].

This distinction between slip and kink bands is crucial when interpreting numerical results. Slip bands often exhibit sharper, more localized plastic deformation, while kink bands are generally broader and associated with smoother gradients in lattice orientation. In the next section, we compare the simulation results from the crystal plasticity model to these theoretical predictions.

3.3.4 Comparison with Experimental Observations and Model Prediction

To assess the predictive capability of the developed crystal plasticity model, numerical results are compared against Rice's analytical solution and available experimental data from micrograph observations. As shown in Figure 3.7, the experimental micrograph exhibits three slip bands radiating from the crack tip, oriented at approximately θ = 54.7°, 90°, and 125.3°. These directions coincide with the theoretical discontinuity angles predicted by Rice's asymptotic solution for a stationary crack in a $\langle 001 \rangle \{110\}$ orientation.

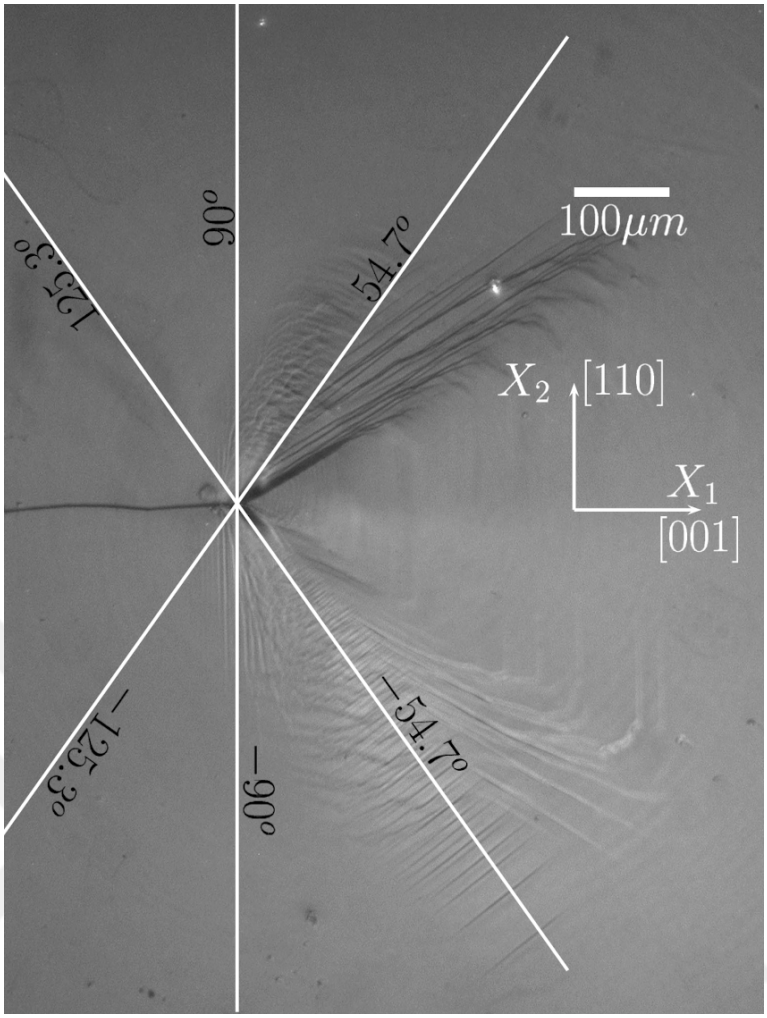

Figure 3.7: Experimental optical micrograph of a cracked specimen under plane strain loading with superimposed analytical solution lines [70].

The finite element simulation shown in Figure 3.8(a) predicts similar patterns of plastic shear strain concentration. Three clearly defined localization bands emerge from the notch tip and align with the directions of the analytical sector boundaries. These bands correspond to regions of intense plastic activity where slip systems are preferentially activated under plane strain constraints. The central vertical band is typically interpreted as a kink band, while the inclined bands are classified as slip bands due to alignment between the band direction and slip plane traces.

Figure 3.8(b) presents a quantitative comparison of the angular distribution of equivalent plastic shear strain, juxtaposed with Rice's theoretical discontinuity lines. While the finite element solution reproduces the three primary shear bands, small differences

exist in peak magnitude and angular spread. The peak strain at $\theta = 90^\circ$ is captured accurately, but the inclined peaks near 55° and 125° exhibit slightly broader and more intense profiles than their analytical counterparts. These differences are attributed to the smoothing and regularization inherent in the numerical formulation.

Although experimental and numerical data do not perfectly coincide in magnitude, the orientation of plastic strain bands aligns well in all cases. The minor discrepancies observed are likely due to limitations in imaging resolution, material variability, and simplifications such as isotropic elasticity in the simulation. Despite these factors, the model successfully reproduces the dominant band structure, validating its capability to simulate anisotropic plastic flow in single crystal Ni-based alloys under plane strain fracture conditions. Overall, the results demonstrate that the developed model faithfully recovers the slip band architecture dictated by Rice's theoretical framework and offers a realistic approximation of the local plasticity mechanisms observable in single crystal nickel-based superalloys. This validation provides a solid foundation for extending the model to more complex loading configurations and for coupling with damage or fracture formulations in future studies.

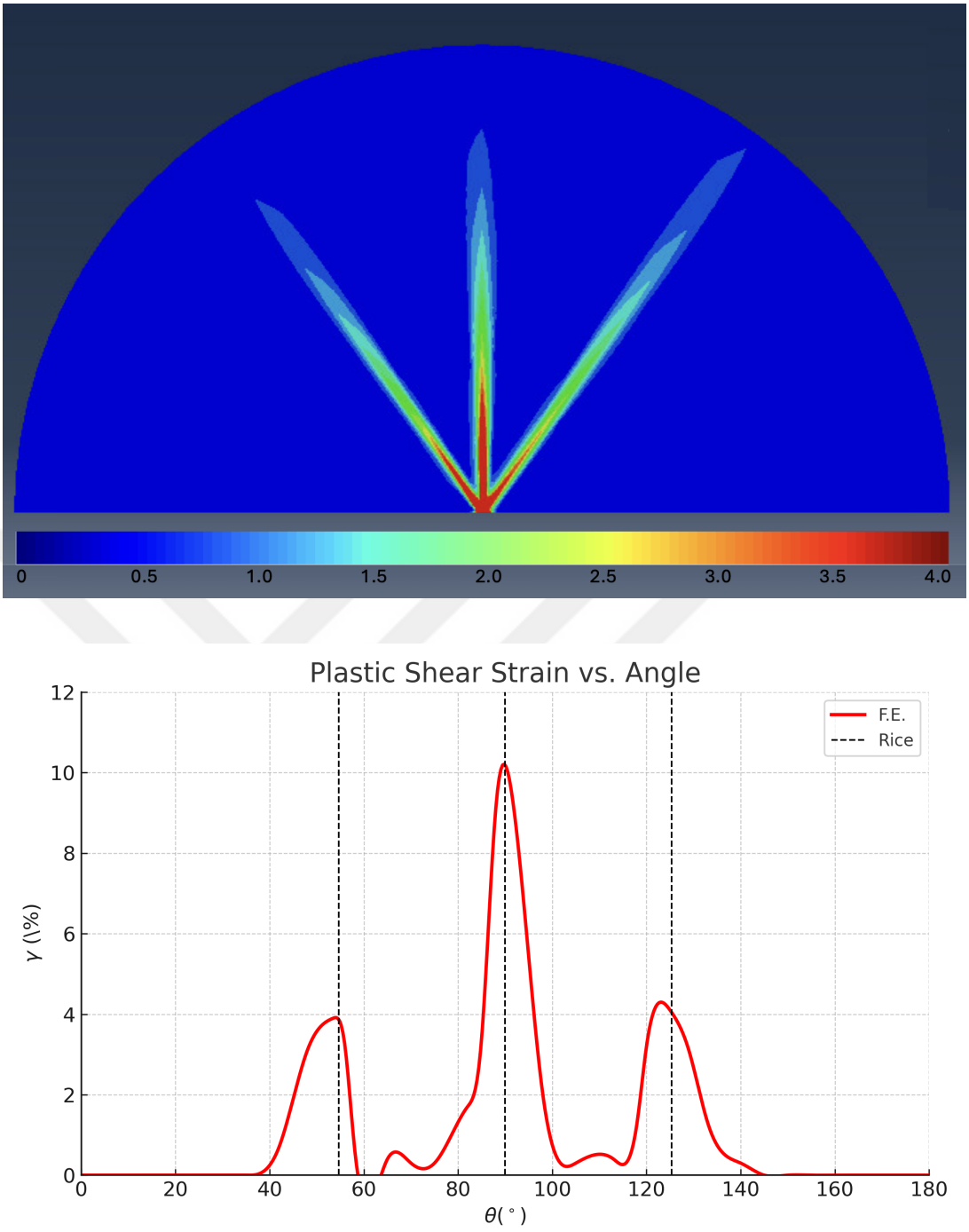

Figure 3.8: Comparison of finite element prediction with Rice's solution. (a) Localized shear band contours. (b) Angular shear strain distribution from FEM, with vertical lines indicating theoretical band angles.

3.4 A Case Study: Tension-Torsion Specimen

3.4.1 Introduction

The accurate modeling of anisotropic plasticity in single crystal materials requires experimental loading conditions that are capable of activating multiple slip systems simultaneously. Among various mechanical tests, tension–torsion experiments stand out as a robust benchmark for this purpose. Unlike uniaxial tension or compression, which often engage only the most favorably oriented slip systems, combined tension–torsion loading introduces non-proportional and multiaxial stress states that are particularly effective in triggering a broader range of slip system activity. This, in turn, provides critical insight into latent hardening, slip interactions, and the directional dependence of plastic flow.

The significance of torsional components in multiaxial testing has been recognized in numerous foundational studies. Franciosi et al. [71] demonstrated that latent hardening, where slip on one system strengthens others, becomes evident only under multi-slip conditions. Peirce, Asaro, and Needleman [55] further emphasized that realistic prediction of single crystal plasticity demands the simulation of complex stress states, achievable only through multiaxial deformation paths. Bassani and Wu [72] explored the evolution of anisotropic yield surfaces under such conditions and highlighted the necessity of accounting for slip system interactions in constitutive formulations. These insights collectively underline that torsion is not merely an added load component, but a key mechanism to probe the underlying structure of plastic anisotropy.

This role of torsional loading becomes even more essential when modeling materials like nickel-based single crystal superalloys, which possess multiple families of active slip systems—including both octahedral and cube slips. Jordan and Walker [73] observed that torsion, when combined with axial tension, is particularly effective in activating otherwise latent slip systems, making it indispensable for both model calibration and validation. Nouailhas and Cailletaud [74] later built upon this approach by applying cyclic tension–torsion loading to specimens, generating rich experimental data that were used to confirm the fidelity of their crystal plasticity framework.

In the present work, the classic tension–torsion benchmark originally proposed by Cailletaud is revisited to assess the predictive capability of the implemented crystal plasticity framework. By simulating cyclic axial–torsional loading on a single crystal specimen, the study aims evaluating the model's ability to reproduce the anisotropic response observed in multiaxial deformation. This comparison serves as an essential verification step, confirming that the model captures directional hardening and slip system interactions accurately, thereby establishing a solid foundation for subsequent extensions to coupled damage modeling.

3.4.2 Dogbone Specimen

The geometry used in this study corresponds to a hollow axisymmetric dogbone specimen designed to reproduce multiaxial stress states under combined loading. As shown in Figure 3.9, the total specimen length is 80 mm, with a gauge section of 26 mm in length and 8 mm in inner radius. The gauge region is filleted into the shoulders via a 55 mm radius, and the outer radius measures 9 mm, resulting in a constant wall thickness of 1 mm across the specimen.

To resolve the crystallographic deformation patterns with high fidelity, a structured mesh composed of $C3D20$ quadratic brick elements with full integration was employed throughout the model. Element dimensions were set to $1 \times 1 \times 1$ mm^3 to ensure sufficient spatial resolution, particularly in the gauge region where plastic localization is anticipated and all analyses were carried under isothermal conditions.

The bottom face of the specimen was fully constrained in all directions, while the torsional loading was applied in the form of a sinusoidal rotation of 3.7° amplitude at the top face. No axial displacement was enforced, thereby imposing cyclic shear deformation under plane strain-like boundary conditions in the axial direction. The specimen was initialized with a [100] crystallographic orientation aligned along the longitudinal axis (Z), consistent with the loading direction, and the tangential torsion was applied around this axis.

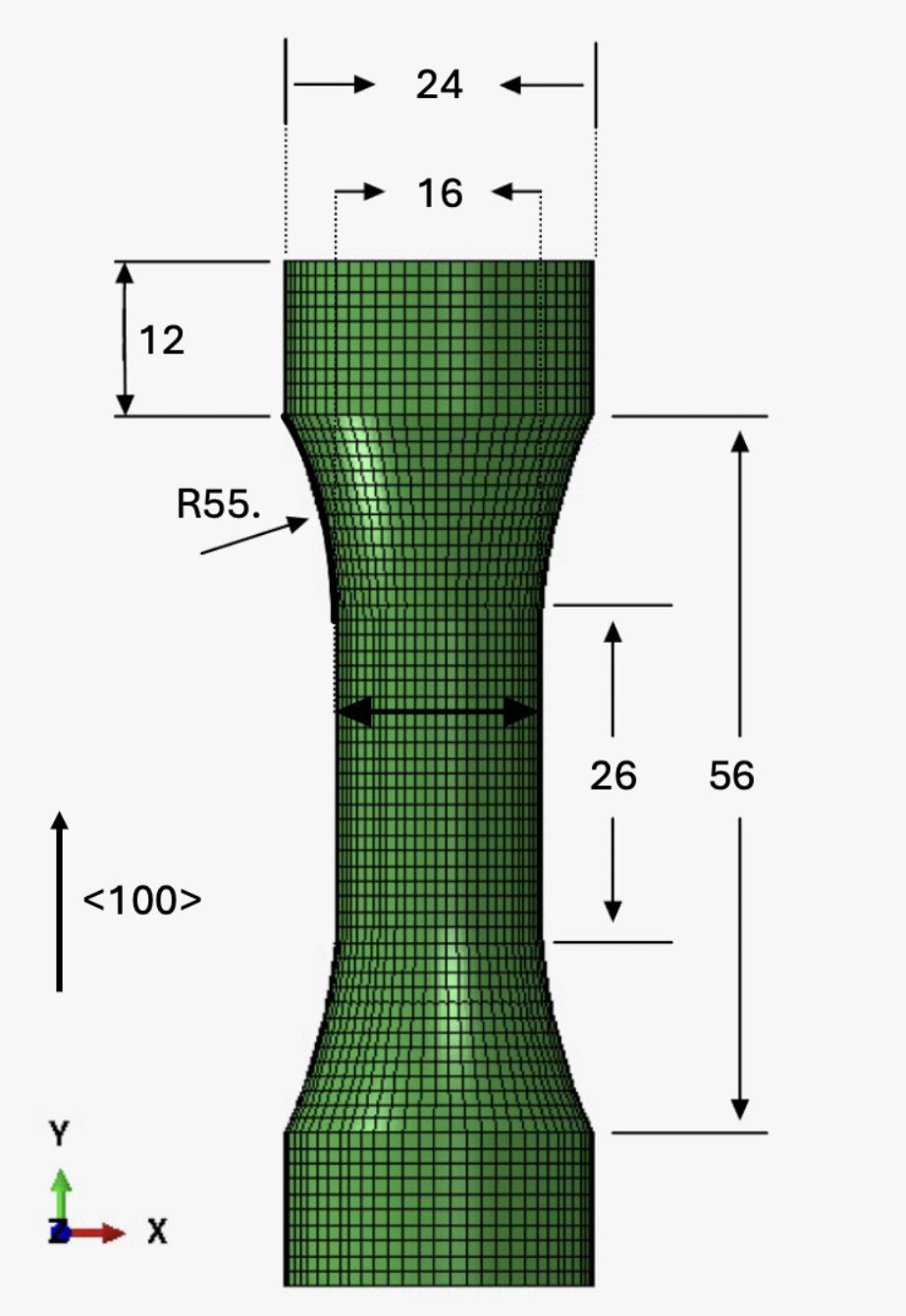

Figure 3.9: Finite element mesh and dimensions of the hollow dogbone specimen.

3.4.3 Results and Discussion

To evaluate the anisotropic deformation response of the crystal plasticity model under multiaxial loading, a tension–torsion simulation was conducted on a single crystal

dogbone specimen oriented along the [100] direction. The loading path consisted of cyclic axial straining while keeping the torsional degree of freedom fixed, thereby promoting non-proportional loading conditions and multi-slip activation—ideal for probing crystallographic anisotropy.

The results from this analysis are illustrated in two complementary views. The first visualization (Figure 3.10) shows the accumulated plastic shear strain on the outer surface of the specimen. Clear directional shear bands emerge and propagate at oblique angles, closely aligned with the active slip systems. This confirms the model's capacity to reproduce orientation-dependent strain localization, a key characteristic of anisotropic single crystal behavior.

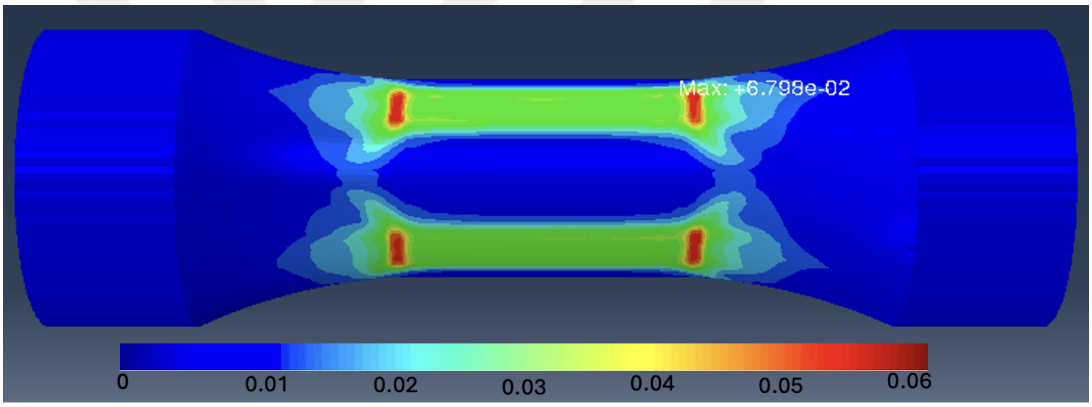

Figure 3.10: Accumulated plastic shear strain on the outer surface of the dogbone specimen under cyclic axial loading.

The second visualization (Figure 3.11) presents a section view through the gauge region, providing additional insight into the internal deformation structure. Four primary shear bands are observed, symmetrically distributed with respect to the loading axis. This further supports that the model accurately captures the spatial orientation and crystallographic trace of the activated slip systems, as expected in a physically-based crystal plasticity framework.

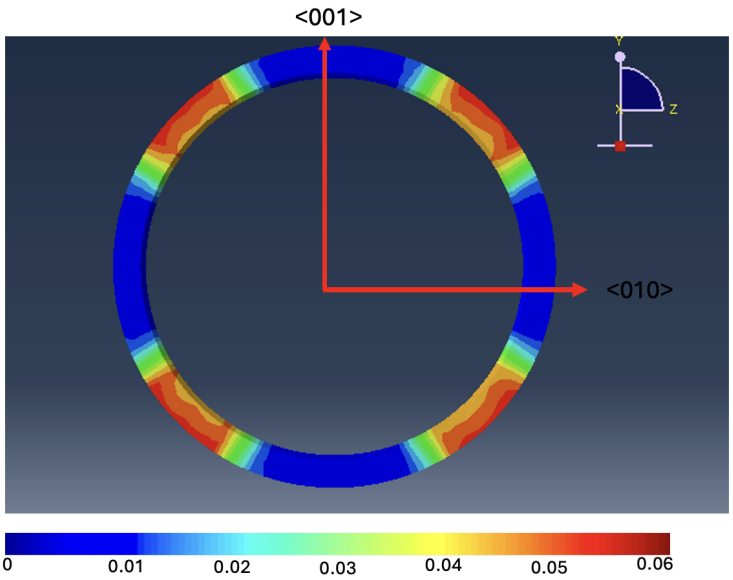

Figure 3.11: Section view of the gauge region showing multiple crystallographically aligned shear bands across the internal structure.

In addition to spatial results, the temporal evolution of the axial stress at the specimen's gauge center is plotted in Figure 3.12. The stress–time curve exhibits nonlinear hardening behavior and cyclic asymmetry, reflecting the history-dependent evolution of slip resistance under multiaxial conditions. While no experimental comparison is made here, the overall characteristics of the stress response are consistent with the expected behavior of single crystal alloys subjected to cyclic deformation.

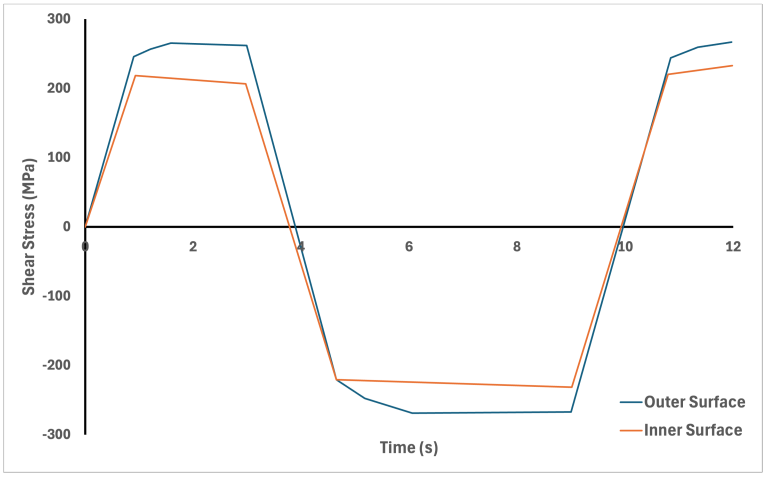

Figure 3.12: Axial stress evolution over time at the specimen's gauge center. The stress response exhibits characteristic anisotropic hardening and cyclic asymmetry.

It is important to note that the present discussion focuses solely on the [100] orientation. A broader assessment incorporating additional orientations and loading paths would enable further evaluation of the model's generality. Readers are referred to the work of Cailletaud [74] for a detailed experimental and numerical treatment of this problem.

Together, the spatial and temporal results highlight the model's ability to resolve anisotropic features of plastic deformation under complex loading. These findings reinforce the robustness of the crystal plasticity formulation and establish a solid foundation for future integration with damage and fracture models.

CHAPTER 4

Damage Modeling of Single Crystals

4.1 Introduction

Accurate prediction of material failure requires modeling frameworks that account not only for plastic deformation but also for the degradation of material properties leading to crack initiation and propagation. While plasticity theories, particularly crystal plasticity, effectively capture the anisotropic and path-dependent deformation behavior of metallic crystals, they fundamentally lack the mechanisms required to describe material softening, damage localization, and fracture [75, 76, 77, 78, 79]. This limitation becomes particularly critical in high-temperature applications, where failure is governed by the accumulation of microstructural damage under creep and fatigue conditions.

Crystal plasticity models inherently assume a hardening response, with no provision for stiffness degradation or crack formation unless an external criterion is applied. However, experimental studies demonstrate that failure often results from co-evolving mechanisms such as dislocation pile-ups, cleavage, void nucleation, γ' rafting, and topological inversion of phases—none of which are captured by classical plasticity alone [80, 81, 79, 82]. For example, cyclic ratchetting under multiaxial loading or rapid tertiary creep softening cannot be reproduced with plasticity models unless coupled with damage [78, 83, 84].

To address this shortcoming, continuum damage mechanics (CDM) was developed, introducing internal variables to represent degradation of the material's load-carrying capacity. Pioneered by Kachanov [85] and Rabotnov [86], and later generalized by

Lemaitre [84] and Chaboche [87], CDM models incorporate scalar or tensorial damage variables into the free energy or effective stress, allowing simulation of stiffness reduction due to void growth, microcracking, or phase instability [88, 89, 82]. These models have been widely used in creep rupture and high-cycle fatigue studies [90, 91].

However, classical CDM suffers from two fundamental limitations. First, it often represents damage as isotropic and homogeneous, which fails to capture direction-sensitive mechanisms such as slip-induced decohesion and cleavage fracture observed in single crystals [79, 91, 92]. Second, and more importantly, local CDM models lead to mesh-dependent solutions when implemented in finite element analyses. As soon as softening begins, the governing PDEs lose ellipticity, resulting in strain localization into infinitesimally small zones and non-physical dissipation that depends on the element size [93, 77, 94, 79].

To overcome this, regularization methods introduce internal length scales into the damage formulation to restore mathematical well-posedness. One class of solutions involves gradient damage models, where the free energy is augmented by a damage gradient term, resulting in Helmholtz-type evolution equations [93, 77, 95, 94, 79]. These models smooth the localization and prevent pathological mesh sensitivity. In the context of crystal plasticity, such formulations have evolved into microdamage models, where anisotropic degradation is governed by crystallographic orientations and combined effects of shear and normal stress [92, 79, 78].

In these models, damage evolves as a function of slip system activity and stress triaxiality, capturing the interplay between ductile and brittle failure modes. For example, Gong et al. [79] developed a directional microdamage model for FCC single crystals that accounts for both cleavage and slip-induced damage. The model includes a Laplacian term for the damage field, introducing a regularization length that controls the size of the localization zone and demonstrates mesh-objective results. Similarly, Wang et al. [78] coupled an anisotropic damage law with crystal plasticity to simulate ratchetting under cyclic loading, revealing the necessity of including damage to capture experimentally observed strain accumulation.

An alternative and increasingly popular regularization framework is the phase-field method for fracture. Based on the variational formulation of brittle fracture [96, 97],

this method approximates cracks with a diffuse scalar field governed by a fracture energy functional. The crack surface energy is regularized over a finite width controlled by an internal length scale, allowing complex crack patterns to be modeled without ad hoc criteria [98, 89, 99].

In recent years, phase-field models have been extended to ductile and creep fracture, incorporating degradation of fracture toughness or elastic energy with plastic strain or creep damage [100, 101, 102]. These models have been successfully applied to simulate high-temperature damage in single crystal superalloys. For instance, Harikrishnan and Le Graverend [82] proposed a creep-phase-field model coupled with a Kachanov-type damage law, capable of predicting topological inversion of the γ/γ' morphology. Similarly, Wu and Zhang [102] integrated phase-field fracture, dislocation-based plasticity, and microstructural evolution to simulate the full creep curve—including the onset of tertiary creep governed by phase coarsening and stiffness degradation.

Both microdamage and phase-field approaches provide a systematic, thermodynamically consistent way to eliminate mesh dependency and capture the competing effects of crystallographic slip, cleavage, and microstructural instability. Their coupling with crystal plasticity enables accurate prediction of not just the deformation behavior, but the entire failure process, from micro-damage nucleation to macroscopic crack propagation [79, 102, 82, 78, 94, 100].

4.2 Continuum Damage Modeling of Single Crystals

This section presents a finite strain continuum damage model for single crystal metallic materials, formulated to capture the anisotropic and mode-dependent nature of fracture processes. The model accounts for cleavage-driven and shear-driven failure mechanisms that activate along crystallographic planes under multiaxial stress states. Damage and plasticity are treated as distinct yet coupled internal processes, evolving according to independent criteria and kinematics.

The total deformation gradient is multiplicatively decomposed into three parts:

$$\mathbf{F} = \mathbf{F}^e\mathbf{F}^p\mathbf{F}^d \tag{4.1}$$

where $\mathbf{F}^e$, $\mathbf{F}^p$, and $\mathbf{F}^d$ denote the elastic, plastic, and damage-induced deformation gradients, respectively. This decomposition reflects the physical sequence in which damage alters the reference configuration, followed by plastic flow and elastic response. Assuming incompressible plasticity, the total Jacobian becomes

$$\det(\mathbf{F}) = J = J^e J^p J^d, \qquad \text{with} \quad J^p = 1 \tag{4.2}$$

4.2.1 Cleavage Systems and Kinematics

Damage is assumed to occur along a set of predefined cleavage planes indexed by $s = 1, \ldots, N_{\text{damage}}$. Each damage system is described by a local orthonormal frame $(\mathbf{n}^s, \boldsymbol{\ell}_1^s, \boldsymbol{\ell}_2^s)$, where $\mathbf{n}^s$ is the normal to the cleavage plane, and $\boldsymbol{\ell}_1^s$, $\boldsymbol{\ell}_2^s$ are in-plane directions capturing shearing deformation modes (Figure 4.1). In FCC crystals, cleavage tends to occur along the (111) planes, while the shearing modes align with the in-plane [110] and $[1\bar{1}0]$ directions.

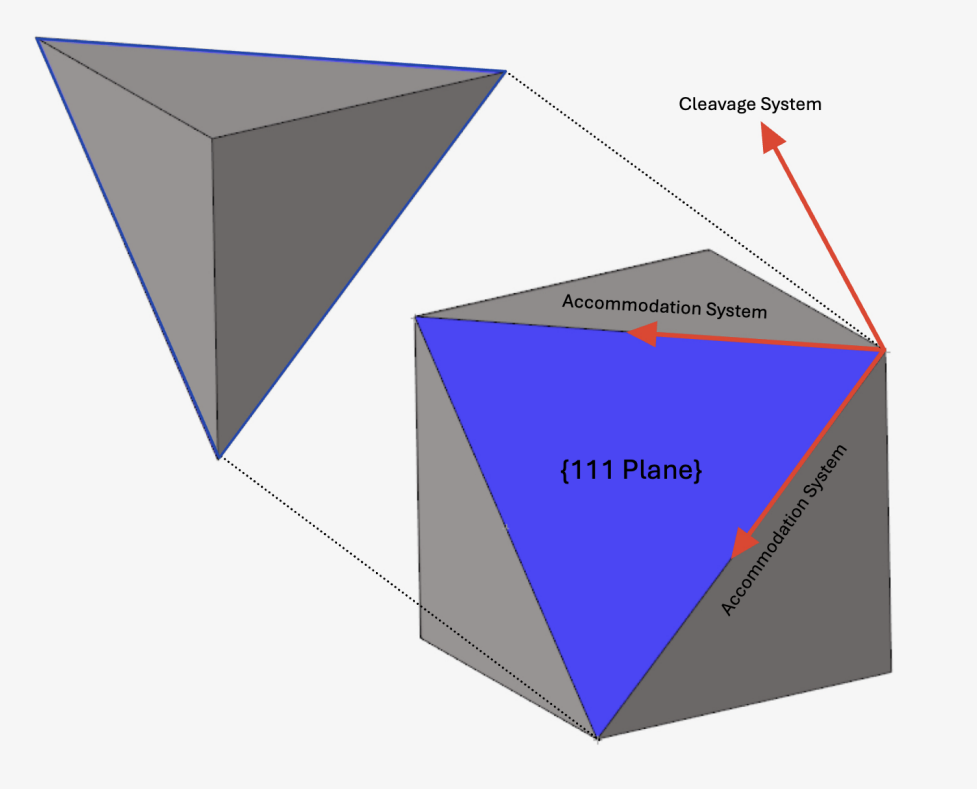

Figure 4.1: Representation of a crystallographic cleavage system defined by normal vector $\mathbf{n}^s$ and two orthogonal accommodation directions $\boldsymbol{\ell}_1^s$ and $\boldsymbol{\ell}_2^s$.

The irreversible velocity gradient associated with damage is expressed as:

$$\mathbf{L}^d = \dot{\mathbf{F}}^d \mathbf{F}^{d-1} = \sum_{s=1}^{N_{\text{damage}}} \left(\dot{\delta}_c^s \, \mathbf{n}^s \otimes \mathbf{n}^s + \dot{\delta}_1^s \, \text{sym}(\mathbf{n}^s \otimes \boldsymbol{\ell}_1^s) + \dot{\delta}_2^s \, \text{sym}(\mathbf{n}^s \otimes \boldsymbol{\ell}_2^s) \right) \tag{4.3}$$

where $\dot{\delta}_c^s$, $\dot{\delta}_1^s$, and $\dot{\delta}_2^s$ are the strain rates for crack opening (Mode I), and in-plane shearing (Modes II and III) along system s.

4.2.2 Driving Forces and Damage Criteria

The thermodynamic force conjugate to damage is the Mandel stress:

$$\mathbf{M} = \mathbf{C}^e \mathbf{T} \tag{4.4}$$

where $\mathbf{C}^e$ is the elastic right Cauchy–Green tensor, and $\mathbf{T}$ is the second Piola–Kirchhoff stress. The projected tractions along the cleavage system are defined as:

$$t_c^s = \mathbf{n}^s \cdot \mathbf{M} \cdot \mathbf{n}^s, \qquad t_i^s = \mathbf{n}^s \cdot \mathbf{M} \cdot \boldsymbol{\ell}_i^s \quad (i = 1, 2) \tag{4.5}$$

Damage activation is governed by critical stress thresholds Y^s, which represent the cleavage strength for each system. A damage criterion is defined for each failure mode as:

$$f_c^s = |t_c^s| - Y^s \tag{4.6}$$

$$f_i^s = |t_i^s| - Y^s \quad (i = 1, 2) \tag{4.7}$$

When $f^s > 0$, damage begins to evolve in the corresponding mode.

4.2.3 Damage Evolution and Coupling

The evolution of crack opening and shearing strains is governed by a rate-dependent power-law form:

$$\dot{\delta}_c^s = \left\langle \frac{f_c^s}{K_d} \right\rangle^{n_d} \text{sign}(t_c^s) \tag{4.8}$$

$$\dot{\delta}_i^s = \left\langle \frac{f_i^s}{K_d} \right\rangle^{n_d} \text{sign}(t_i^s), \quad i = 1, 2 \tag{4.9}$$

where K_d is a damage viscosity parameter and n_d is the damage rate exponent. The Macaulay brackets ensure that damage initiates only when the driving force exceeds the threshold. Moreover, unilateral damage conditions are enforced in Mode I by suppressing evolution under compression:

$$\dot{\delta}_c^s = 0 \quad \text{if} \quad t_c^s < 0 \tag{4.10}$$

The total damage activity is monitored through a scalar cumulative rate:

$$\dot{d} = \sum_{s=1}^{N_{\text{damage}}} \left(|\dot{\delta}_c^s| + |\dot{\delta}_1^s| + |\dot{\delta}_2^s| \right) \tag{4.11}$$

The variable d serves as a global indicator of material degradation and is used to couple damage to the material's strength.

To capture the progressive softening of cleavage strength due to plastic deformation, the critical stress threshold Y^s is allowed to decay with cumulative slip:

$$\gamma_{\text{cum}} = \sum_{s=1}^{N_{\text{slip}}} |\dot{\gamma}^s|, \qquad Y^s = \sigma_{c0}\, e^{-\Theta \gamma_{\text{cum}}} + \sigma_{\text{res}} \tag{4.12}$$

An alternative formulation links the degradation to the accumulated scalar damage variable d, leading to:

$$Y^s = Y_0^s + Hd + \sigma_{\text{ult}} \tag{4.13}$$

Here, Y_0^s is the initial damage threshold (often degraded by plasticity), $H < 0$ is the softening modulus controlling damage-driven weakening, and σ_{ult} is the residual strength at full degradation. In the present formulation, only plastic deformation affects damage thresholds. The influence of damage on plasticity is neglected due to the lack of experimental evidence supporting such coupling in single crystal metals. Thus, the interaction is modeled as one-way and thermodynamically consistent.

4.2.4 Mesh Dependency Problem

A fundamental challenge in strain-softening damage mechanics is the mesh-dependent nature of localization. In local models, once material instability begins (typically initiated by softening), the deformation and damage localize into increasingly smaller

zones as the mesh is refined. This phenomenon is not only numerical but also physical in consequence: since the formulation lacks a characteristic length scale, the size of the localization zone becomes arbitrarily small, violating energy balance and causing global responses to change with discretization. This mesh sensitivity can lead to significant inaccuracies in predicted failure loads, crack paths, and dissipated energy [103, 93].

To demonstrate this effect, we consider a simple one-dimensional traction test of a $1\,\text{mm} \times 7\,\text{mm}$ rectangular bar under vertical loading. The boundary conditions are illustrated in Figure 4.2. A displacement of 0.7 mm is applied at the top edge of the bar, while the bottom edge is fully constrained in the vertical (Y) direction. To eliminate rigid body motion, the bottom-left corner is additionally fixed in the horizontal (X) direction.

Four different finite element discretizations are used: 3, 5, 7, and 9 elements. A small imperfection is introduced into the central element of each mesh to act as a crack nucleation point. Figure 4.3 shows the final equivalent damage fields obtained from each simulation.

The figure reveals that damage consistently localizes into a single element—the one containing the initial imperfection—regardless of mesh density. As the mesh is refined, the damaged zone becomes narrower, and the peak damage increases. This behavior results from the absence of any internal length scale in the formulation: smaller elements experience higher strain under the same applied displacement, leading to more rapid damage accumulation. The finer the mesh, the faster this concentration occurs.

This phenomenon is also evident in the global response plots. Figure 4.4 shows the stress vs. displacement response for all mesh configurations. Interestingly, the 9-element simulation fails earlier than the 3-element one, reaching zero stress more quickly. This is not due to material behavior but rather faster localization: although the material softens identically under the same constitutive law, the smaller element size amplifies strain and thus accelerates softening. In contrast, the larger elements in coarser meshes distribute strain over a wider volume, resulting in delayed failure. This clearly demonstrates that without regularization, the apparent softening behavior

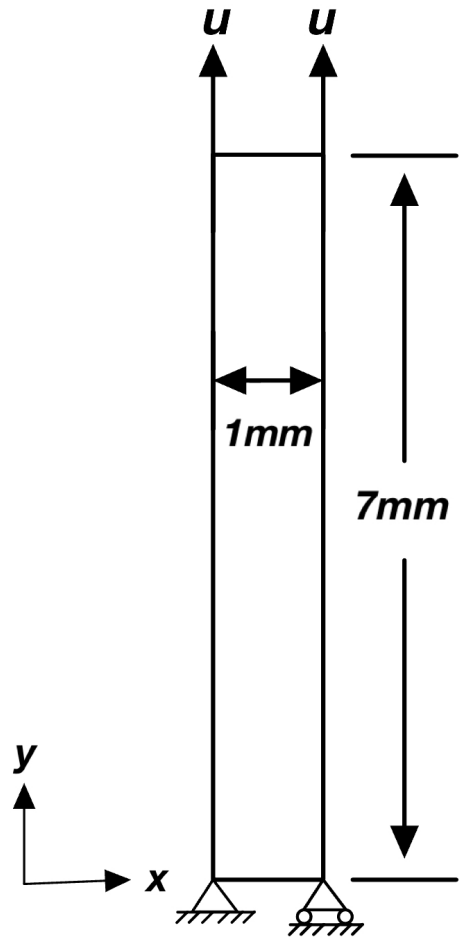

Figure 4.2: Geometry and boundary conditions of the 1D tensile bar. A vertical displacement of 0.7 mm is applied at the top edge, while the bottom edge is fully fixed in Y. The bottom-left corner is fixed in X to prevent rigid motion.

of the material is an artifact of discretization.

In contrast, the stress vs. equivalent damage curves in Figure 4.5 reveal an important distinction. All simulations follow nearly identical trajectories during the damage evolution phase, reflecting the fact that the softening law—governed by a mesh-independent damage resistance parameter H—is consistent across analyses. However, the endpoints of each curve differ: finer meshes result in larger total damage values at failure. This is because the same amount of energy is dissipated within a smaller element, increasing the equivalent damage in that location. Thus, although the material model behaves consistently at the integration point level, its localization behavior—and consequently the global results—are mesh dependent.

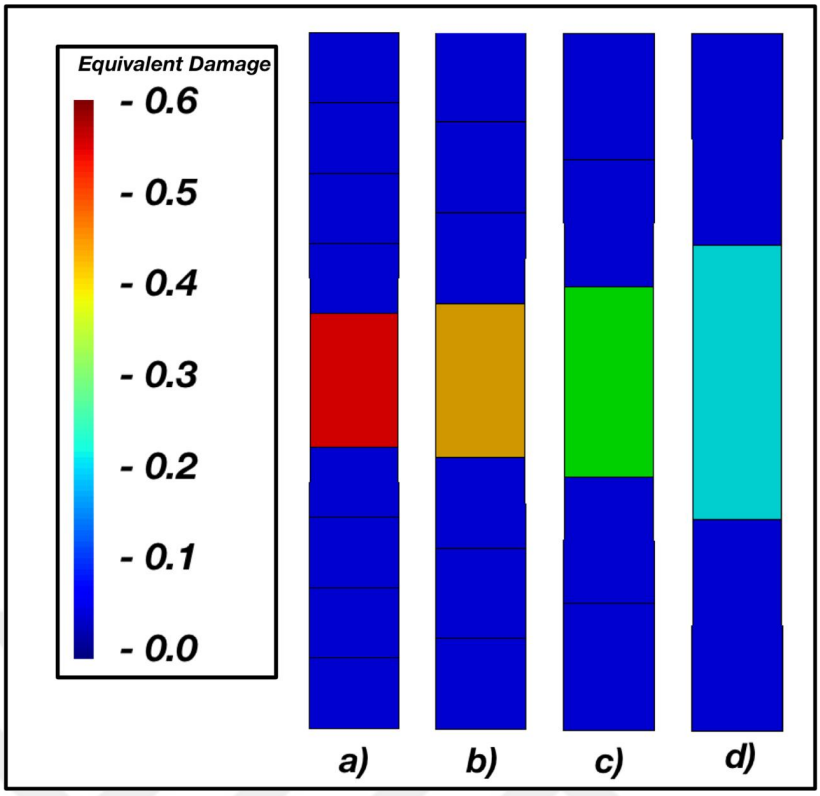

Figure 4.3: Equivalent damage field at failure for different mesh densities: (a) 9 elements, (b) 7 elements, (c) 5 elements, (d) 3 elements. In all cases, damage localizes into the central element, with narrower localization observed in finer meshes.

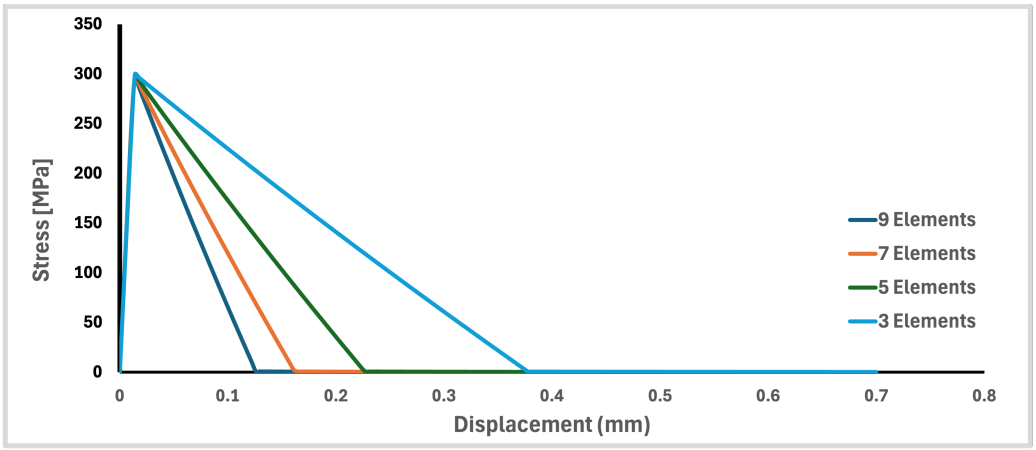

Figure 4.4: Stress vs. displacement curves for different mesh densities.

These observations highlight the dual impact of mesh dependency in local damage formulations: it affects both the quantitative damage evolution and the apparent softening response. Without a mechanism to regularize damage over a finite length scale,

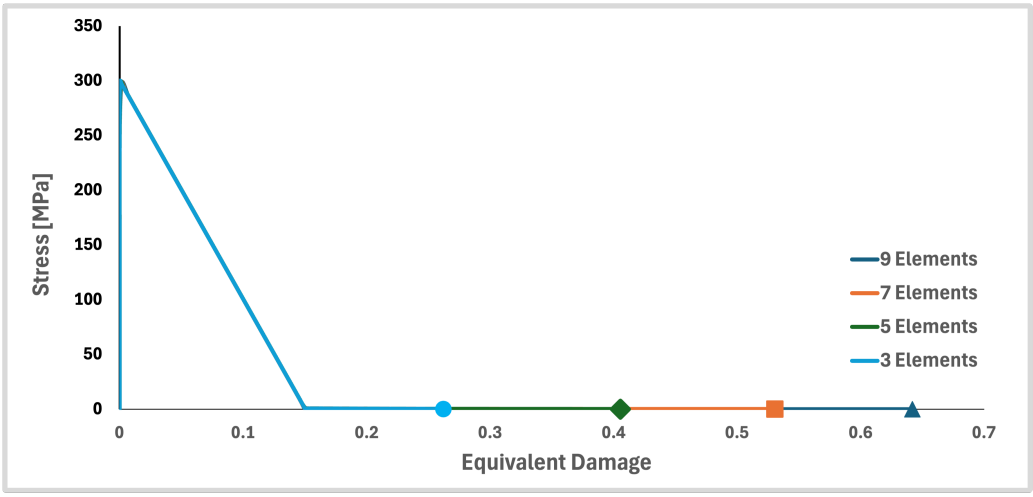

Figure 4.5: Stress vs. equivalent damage for different mesh densities.

such models fail to provide physically meaningful or mesh-objective results. In the next section, we introduce a regularized microdamage formulation to resolve this issue and ensure spatially distributed failure processes.

4.3 Microdamage Modeling

4.3.1 Motivation and Background

Classical continuum mechanics assumes that the stress at a material point depends solely on the local deformation, with no influence from neighboring points. While this assumption holds for many standard engineering problems, it becomes inadequate in the presence of strain-softening phenomena and damage localization. Under such conditions, conventional local damage models exhibit pathological mesh sensitivity, where the predicted response—particularly in terms of energy dissipation and failure progression—depends on the discretization.

As demonstrated in Figure 4.3, once softening begins, the deformation tends to localize into a single element, leading to spurious loss of stiffness and non-physical results that are not representative of the underlying material behavior.

To address this issue, the framework of *generalized continua* provides a physically motivated alternative. Among the most comprehensive of these is the *micromorphic theory* developed by Eringen and Suhubi [104], which extends the classical continuum by introducing additional degrees of freedom that account for microstructural effects. These may include independent micro-rotations, deformation gradients, or scalar fields associated with internal material processes. Each additional field satisfies its own balance law, allowing the material model to capture internal length scales, gradient effects, and substructure interactions. This enrichment enables more accurate modeling of phenomena such as strain localization, size effects, and fracture initiation.

A particular scalar specialization of this theory is the *microdamage formulation*, wherein a scalar internal field ${}^{\chi}d$ is introduced to describe the evolution of sub-critical damage at the microscale. Unlike classical damage models, where a local scalar variable d evolves pointwise based on stress or strain history, the microdamage framework treats ${}^{\chi}d$ as a continuous field governed by a partial differential equation. This field captures the spatial distribution of damage and introduces an intrinsic length scale that governs the width of the localization zone. The evolution of ${}^{\chi}d$ is energetically coupled to the local damage variable d through a penalty term, ensuring smooth and physically consistent damage propagation across the domain. As a result, the formulation yields *well-posed, mesh-objective solutions* even under conditions of strong softening.

In this study, we extend the scalar microdamage framework to a *finite strain setting* and implement it in the commercial finite element software *Abaqus*. The approach in this work departs from earlier studies (e.g., [6, 106, 107]) in several key aspects. First, the formulation is developed entirely under finite deformation kinematics, which is essential for modeling ductile single crystals subjected to large strains. Second, the numerical implementation is carried out via a coupled subroutine architecture. A custom *User Element Subroutine (UEL)* is developed to solve the microdamage evolution equation, introducing an additional scalar degree of freedom at each node of standard

two-dimensional and three-dimensional brick and shell elements. This field is tightly coupled with a *User Material Subroutine (UMAT)*, which governs the constitutive response, including plasticity and local damage evolution. The coupled system enables the consistent simulation of damage regularization across multiple scales and geometries, from one-dimensional bars to three-dimensional compact tension specimens. The next sections describe the theoretical foundations and numerical implementation of this microdamage model in detail.

4.3.2 Microdamage Continuum Formulation

The microdamage continuum formulation employed here builds upon the micromorphic theory originally introduced by Eringen and Suhubi [104]. In contrast to conventional damage models, this approach introduces a regularized internal variable ${}^{\chi}d$—referred to as the microdamage field—which serves to control the spatial distribution of damage and eliminate pathological mesh sensitivity. By enriching the kinematic description with this additional field, a thermodynamically consistent and numerically stable framework for damage regularization is obtained [105].

4.3.2.1 Balance and Constitutive Equations

The set of primary degrees of freedom is extended to include both displacement and microdamage:

$$\text{DOF} = \{\mathbf{u}, {}^{\chi}d\}, \qquad \text{STRAIN} = \{\mathbf{E}, d, {}^{\chi}d, \nabla^{\chi}d\}$$

where $\mathbf{u}$ is the displacement field, d is the local damage variable, and $\mathbf{E}$ denotes the elasto-plastic logarithmic strain tensor. The microdamage field ${}^{\chi}d$ acts as a nonlocal counterpart to d, providing regularization through its spatial gradient.

The internal virtual power of the system is generalized as:

$$\mathcal{P}^{\text{int}} = \mathbf{S} : \dot{\mathbf{E}} + a\,{}^{\chi}\dot{d} + \mathbf{b} \cdot \nabla^{\chi}\dot{d} \tag{4.14}$$

where:

- $\mathbf{S}$: second Piola–Kirchhoff stress, conjugate to $\mathbf{E}$,
- a: scalar microforce conjugate to ${}^{\chi}d$,
- $\mathbf{b}$: vectorial microstress conjugate to $\nabla^{\chi}d$.

Stationarity of the internal power yields the governing field equations:

$$\operatorname{Div}\mathbf{P} = \mathbf{0} \qquad \text{(Momentum balance)} \tag{4.15}$$

$$a = \operatorname{Div}\mathbf{b} \qquad \text{(Microforce balance)} \tag{4.16}$$

where $\mathbf{P}$ is the first Piola–Kirchhoff stress.

The Helmholtz free energy per unit reference volume is expressed as:

$$\rho\psi = \psi_{ep}(\mathbf{E}) + \frac{1}{2}Hd^2 + \frac{1}{2}{}^{\chi}H(d - {}^{\chi}d)^2 + \frac{1}{2}A\,\nabla^{\chi}d \cdot \nabla^{\chi}d \tag{4.17}$$

with the following physical interpretations:

- $\psi_e(\mathbf{E})$: elastic strain energy density,
- $H < 0$: softening modulus governing degradation due to damage,
- ${}^{\chi}H > 0$: penalty stiffness enforcing consistency between d and ${}^{\chi}d$,
- $A > 0$: gradient regularization parameter controlling the spatial smoothness of ${}^{\chi}d$,
- ρ: mass density.

The associated constitutive relations follow from the energy derivatives:

$$\mathbf{S} = \rho\,\frac{\partial\psi}{\partial\mathbf{E}} = \frac{\partial\psi_e}{\partial\mathbf{E}} \tag{4.18}$$

$$a = \rho\,\frac{\partial\psi}{\partial{}^{\chi}d} = -{}^{\chi}H(d - {}^{\chi}d) \tag{4.19}$$

$$\mathbf{b} = \rho\,\frac{\partial\psi}{\partial\nabla^{\chi}d} = A\nabla^{\chi}d \tag{4.20}$$

Inserting these into the microforce balance leads to a Helmholtz-type partial differential equation governing the microdamage field:

$$ {}^{\chi}d - \frac{A}{{}^{\chi}H}\Delta {}^{\chi}d = d \tag{4.21} $$

4.3.2.2 Damage Driving Force and Evolution

The thermodynamic driving force for the evolution of local damage is derived from the free energy as:

$$ Y_f = \rho \frac{\partial \psi}{\partial d} = Hd + {}^{\chi}H(d - {}^{\chi}d) \tag{4.22} $$

This expression replaces the classical critical damage stress criterion with a penalized formulation in which Y_f reflects the combined influence of softening (H) and the microdamage consistency condition (${}^{\chi}H$). The damage evolution satisfies the Kuhn–Tucker conditions:

$$ \dot{d} \geq 0, \quad Y_f \leq 0, \quad \dot{d} \cdot Y_f = 0 \tag{4.23} $$

Plasticity is coupled to damage by degrading the effective damage threshold. Specifically, the modified damage criterion is expressed as:

$$ Y^s = Y_0 \, e^{-\Theta \gamma_{\text{cum}}} + \sigma_{\text{ult}} + Y_f \tag{4.24} $$

This expression reflects a one-way coupling from plasticity to damage: as plastic slip accumulates, the material's resistance to further damage (Y^s) decreases exponentially. The presence of the regularization term Y_f ensures smooth and mesh-independent damage fields by linking local degradation to the nonlocal microdamage variable.

4.3.2.3 Regularization of a 1D Bar

The regularization properties of the microdamage formulation can be demonstrated analytically and numerically through a one-dimensional tensile bar example. This simplified setting provides insight into the spatial smoothing behavior introduced by the gradient-enhanced microdamage field.

The damage consistency function for the 1D setting takes the form:

$$ f = 2\mu(\varepsilon - d) - Y_0 - (H + {}^{\chi}H)d + {}^{\chi}H {}^{\chi}d = 0 \tag{4.25} $$

where μ is the shear modulus, Y_0 is the damage threshold, and $H < 0$, ${}^{\chi}H$, and A are material parameters that govern softening, penalization, and gradient regularization, respectively. Under equilibrium and microforce balance, the governing equation for the regularized microdamage field reduces to a third-order differential equation. The solution admits a sinusoidal form:

$$ {}^{\chi}d(x) = \alpha \sin(\omega x) + \beta \cos(\omega x) + \gamma, \quad \text{where} \quad \omega = \sqrt{\frac{H\,{}^{\chi}H}{A(H + {}^{\chi}H)}} \tag{4.26} $$

This result confirms that the regularization introduces a characteristic length scale $\ell = 1/\omega$, which governs the spatial extent of the damage field.To validate this regularization behavior numerically, a 2D rectangular strip of dimensions 15 mm × 1 mm is modeled under plane stress conditions. The left boundary is constrained in the x-direction, and the lower-left corner is additionally fixed in the y-direction to eliminate rigid body motion. A total displacement of 0.35 mm is applied to the right edge in the horizontal direction.

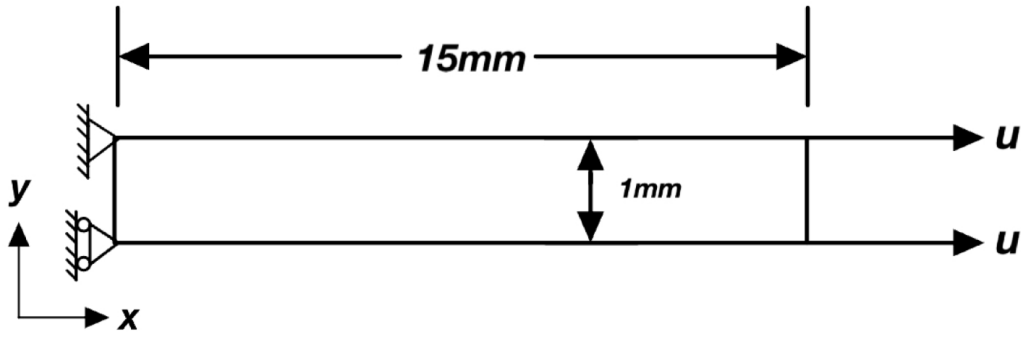

Figure 4.6: Geometry and boundary conditions of the 1D strip specimen under tension.

The material parameters used in the simulation are:

- Softening modulus: $H = -7500\,\text{MPa}$
- Microdamage penalty stiffness: ${}^{\chi}d = 30000\,\text{MPa}$
- Gradient regularization parameter: $A = 2000\,\text{MPa} \cdot \text{mm}^2$
- Damage threshold: $Y_0 = 300\,\text{MPa}$

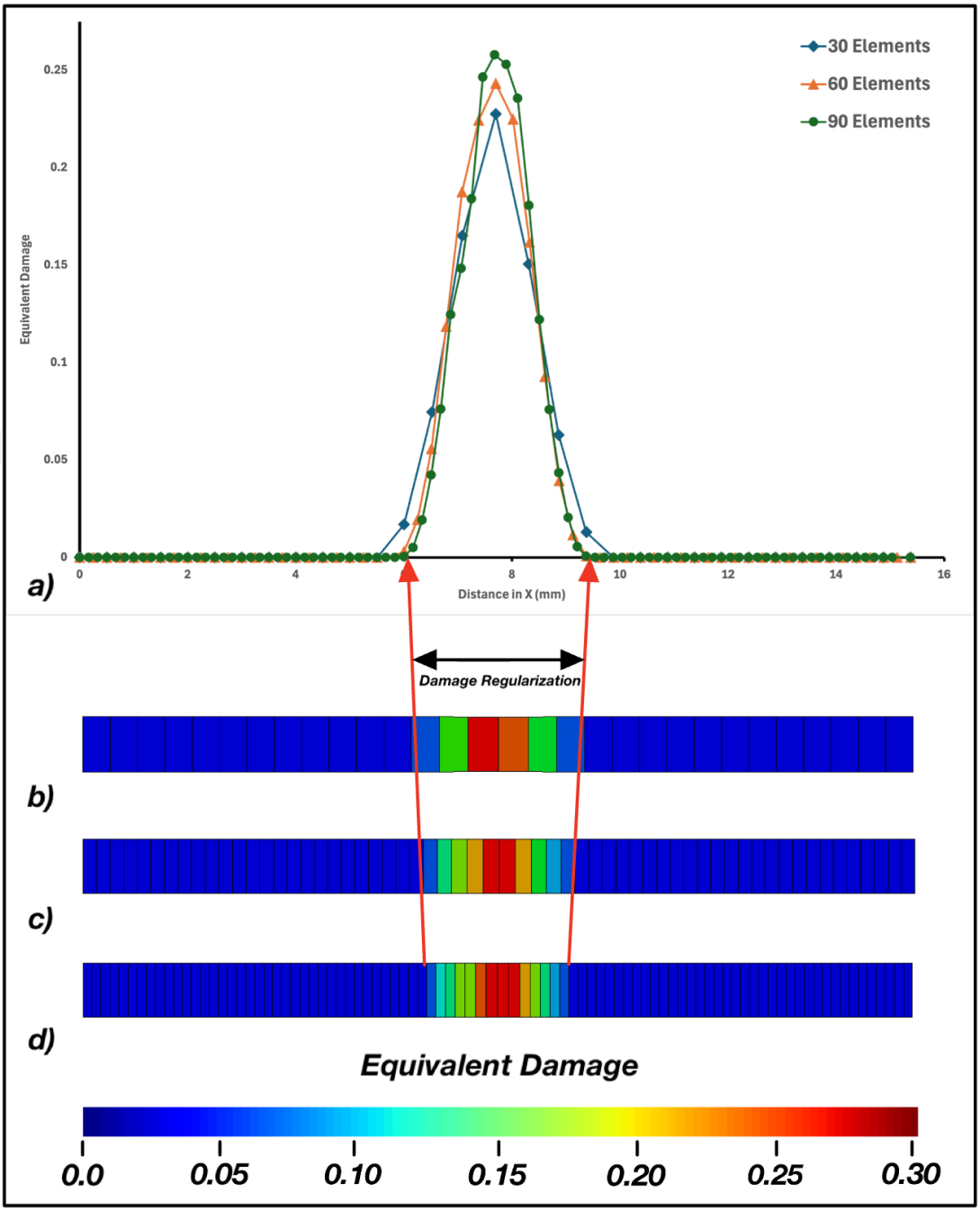

Figure 4.7: Mesh-objective damage evolution: (a) Equivalent damage profile along the specimen for different mesh densities. (b) Damage field for 30 elements. (c) Damage field for 60 elements. (d) Damage field for 90 elements.

The bar is discretized using three different mesh densities: 30, 60, and 90 linear elements along its length. A small imperfection is introduced at the center to trigger damage localization. The results are presented in Figure 4.7.

The results in Figure 4.7 provide critical evidence of the effectiveness of the microdamage formulation in addressing mesh dependency—a long-standing issue in local damage mechanics. The damage profiles obtained for different mesh densities are in close agreement with one another, both in spatial extent and in shape. Although slight differences are observed at the damage peak due to element resolution, the width and position of the damage band remain consistent.

This behavior sharply contrasts with conventional local damage models, where damage typically concentrates into a single element and results vary drastically with mesh refinement. Here, the presence of the gradient term and internal length scale ensures that localization is spread over a physically meaningful zone, independent of element size. This enables objective predictions of failure without requiring prohibitively fine meshes.

The ability to simulate strain-softening and damage propagation with mesh-insensitive results represents a significant advancement in the continuum modeling of failure. It establishes the microdamage formulation as a robust and thermodynamically consistent framework capable of capturing distributed failure processes in a physically grounded and computationally reliable manner.

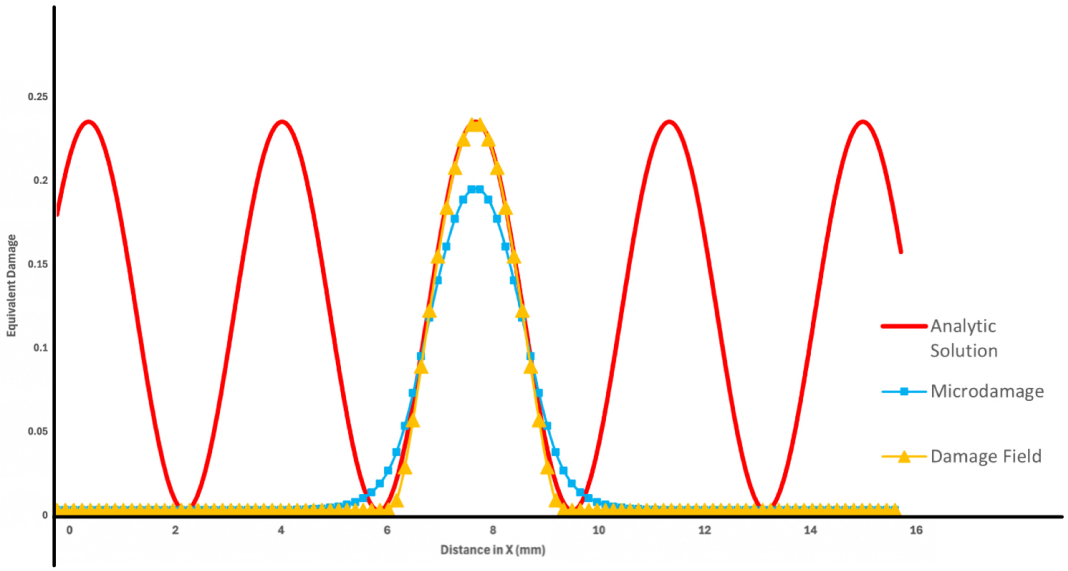

Figure 4.8: Comparison between the analytical solution and the simulation result for the 90-element case.

Figure 4.8 presents a direct comparison between the analytical damage solution and the numerical results for the finest discretization (90 elements). The simulation data align exceptionally well with the analytical profile, both in terms of amplitude and spatial distribution. This agreement validates not only the correctness of the numerical implementation but also the physical fidelity of the theoretical framework.

The ability of the model to reproduce the expected closed-form solution under idealized conditions demonstrates that the regularization is not an artifact of numerical diffusion, but rather an intrinsic and predictable response of the system. This result establishes strong confidence in the microdamage formulation's applicability to more complex, realistic geometries—while maintaining objectivity and mesh-independence throughout.

4.3.2.4 Finite Element Implementation

The numerical implementation of the microdamage-regularized crystal plasticity model is performed using the finite element method in the finite strain setting. The displacement field $\mathbf{u}$ and scalar microdamage field ${}^{\chi}d$ are treated as primary degrees

of freedom. The constitutive equations for crystal plasticity and local damage are solved within the `UMAT`, while the microdamage evolution governed by a Helmholtz-type PDE is solved through a `UEL` formulation. This section presents the variational formulation and the fully implicit incremental integration strategy used in the implementation.

4.3.2.5 Variational Formulation and Discretization

The weak form of the governing equations is derived from the extended principle of virtual power. In the reference configuration Ω, the virtual internal power becomes:

$$\delta\mathcal{W}_{\text{int}} = \int_{\Omega} \left[\mathbf{P} : \delta\dot{\mathbf{F}} + a\,\delta^{\chi}\dot{d} + \mathbf{b} \cdot \nabla\delta^{\chi}\dot{d} \right] dV \tag{4.27}$$

Imposing balance with external virtual work, and applying integration by parts, yields the coupled weak form:

$$\int_{\Omega} \delta\mathbf{F} : \mathbf{P}\, dV = \int_{\partial\Omega_t} \delta\mathbf{u} \cdot \mathbf{T}\, dS \tag{4.28}$$

$$\int_{\Omega} \left[\delta^{\chi}d\, a + \nabla\delta^{\chi}d \cdot \mathbf{b} \right] dV = \int_{\partial\Omega_{\chi}} \delta^{\chi}d\, \bar{a}\, dS \tag{4.29}$$

The displacement field and microdamage field are discretized with standard finite element interpolation:

$$\mathbf{u} = N_u\, \mathbf{d}_u, \quad {}^{\chi}d = N_{\chi}\, \mathbf{d}_{\chi}, \quad \nabla^{\chi}d = B_{\chi}\, \mathbf{d}_{\chi} \tag{4.30}$$

The discretized internal force vectors for the mechanical and microdamage parts become:

$$\mathbf{R}_u = \int_{\Omega} B_u^T \mathbf{P}\, dV - \int_{\partial\Omega_t} N_u^T \mathbf{T}\, dS \tag{4.31}$$

$$\mathbf{R}_{\chi} = \int_{\Omega} N_{\chi}^T a\, dV + \int_{\Omega} B_{\chi}^T \mathbf{b}\, dV - \int_{\partial\Omega_{\chi}} N_{\chi}^T \bar{a}\, dS \tag{4.32}$$

4.3.2.6 Implicit Incremental Formulation

The integration of internal variables is performed locally at each integration point using a fully implicit Newton–Raphson scheme.

The total deformation gradient is assumed to follow the multiplicative decomposition:

$$\mathbf{F} = \mathbf{F}_e \, \mathbf{F}_p \, \mathbf{F}_d \tag{4.33}$$

and the elastic right Cauchy-Green tensor is:

$$\mathbf{C}_e = \mathbf{F}_e^T \mathbf{F}_e = \mathbf{F}_d^{-T} \, \mathbf{F}_p^{-T} \, \mathbf{C} \, \mathbf{F}_p^{-1} \, \mathbf{F}_d^{-1} \tag{4.34}$$

At time $t_{n+1} = t_n + \Delta t$, the update of internal variables is formulated in residual form as:

$$\mathbf{R} = \begin{Bmatrix} R_{\mathbf{C}_e} \\ R_{\gamma^s} \\ R_d \\ R_{\chi d} \end{Bmatrix} = \begin{Bmatrix} \Delta \mathbf{C}_e + \Delta \mathbf{C}_p + \Delta \mathbf{C}_d - \Delta \mathbf{C} \\ \Delta \gamma^s - \Delta t \cdot \dot{\gamma}^s \\ \Delta d - \Delta t \cdot \dot{d} \\ {}^{\chi}d - \dfrac{A}{{}^{\chi}H} \nabla^2 {}^{\chi}d - d \end{Bmatrix} \tag{4.35}$$

The Jacobian matrix is constructed as:

$$[J] = \begin{bmatrix} \frac{\partial R_{\mathbf{C}_e}}{\partial \Delta \mathbf{C}_e} & \frac{\partial R_{\mathbf{C}_e}}{\partial \Delta \gamma^s} & \frac{\partial R_{\mathbf{C}_e}}{\partial \Delta d} & 0 \\ \frac{\partial R_{\gamma^s}}{\partial \Delta \mathbf{C}_e} & \frac{\partial R_{\gamma^s}}{\partial \Delta \gamma^s} & 0 & 0 \\ \frac{\partial R_d}{\partial \Delta \mathbf{C}_e} & \frac{\partial R_d}{\partial \Delta \gamma^s} & \frac{\partial R_d}{\partial \Delta d} & 0 \\ 0 & 0 & \frac{\partial R_{\chi d}}{\partial \Delta d} & \frac{\partial R_{\chi d}}{\partial {}^{\chi}d} \end{bmatrix} \tag{4.36}$$

Representative derivative terms are:

$$\frac{\partial R_{\gamma^s}}{\partial \Delta \gamma^s} = 1 - \Delta t \cdot \frac{\partial \dot{\gamma}^s}{\partial \tau^s} \cdot \frac{\partial \tau^s}{\partial \gamma^s} \tag{4.37}$$

$$\frac{\partial R_{\chi d}}{\partial {}^{\chi}d} = 1 + \frac{A}{{}^{\chi}d} \nabla^2 \tag{4.38}$$

$$\frac{\partial R_{\chi d}}{\partial d} = -1 \tag{4.39}$$

After convergence, the internal variables are updated as:

$$\mathbf{C}_e^{n+1} = \mathbf{C}_e^n + \Delta \mathbf{C}_e, \quad \gamma^{s,n+1} = \gamma^{s,n} + \Delta \gamma^s, \quad d^{n+1} = d^n + \Delta d, \quad {}^{\chi}d^{n+1} = {}^{\chi}d^n + \Delta {}^{\chi}d \tag{4.40}$$

The consistent algorithmic tangent modulus for the global Newton iterations is then computed as:

$$\mathbb{C}^{\text{alg}} = \frac{\partial \mathbf{P}}{\partial \mathbf{F}} \tag{4.41}$$

This formulation guarantees mesh objectivity via the regularized microdamage field and allows robust convergence under complex loading paths.

4.3.3 Fatigue Crack Growth

This section investigates the fatigue crack growth behavior of the proposed microdamage regularized crystal plasticity model under cyclic loading using compact tension (CT) specimens. The aim is to assess the model's ability to capture anisotropic fatigue crack propagation, crack bifurcation, and the transition from plasticity-dominated to damage-controlled fracture modes.

The CT specimen geometry used in this study corresponds to the one illustrated earlier in Figure 3.1, with a specimen width of $w = 40$ mm, an initial crack length of $a = 18$ mm, and a thickness of $B = 3$ mm. The material orientation is defined by $(001)\langle 110\rangle$, a commonly used configuration in nickel-based single crystal superalloys to activate multiple slip systems under tensile loading. To mimic realistic service conditions, a fully mechanical cyclic loading is applied with a maximum load amplitude of $F = 220$ N over 400 cycles. The load control uses a load ratio of $R = 0.6$, where $R = F_{\min}/F_{\max}$, representing tension-tension cyclic loading.

To accurately resolve the damage field and crack propagation path, the region around the initial crack tip is finely meshed with a minimum element size of $10\,\mu$m. This refinement ensures the ability to capture narrow damage bands, crack branching phenomena, and evolving stress concentrations.

The mode I stress intensity factor for the compact tension geometry is computed using the analytical formulation proposed by Marchal (2006), given by:

$$K_I = \frac{F}{B\sqrt{w}} \left\{ \frac{\sqrt{2\tan\left(\frac{\pi a}{2w}\right)}}{\cos\left(\frac{\pi a}{2w}\right)} \left[0.752 + 2.02\frac{a}{w} + 0.37\left(1 - \sin\left(\frac{\pi a}{2w}\right)\right)^3 \right] \right\} \tag{4.42}$$

This expression relates the applied force to the stress intensity factor at the crack tip, accounting for the CT geometry and current crack length. It forms the basis for tracking the fatigue driving force in terms of the range ΔK over the course of loading cycles. The subsequent subsections present the detailed numerical results for 2D and 3D simulations, each compared with experimental benchmarks and analyzed with respect to plastic-damage interaction and anisotropic propagation characteristics.

4.3.3.1 2D Simulation Results

To assess the predictive capabilities of the microdamage-regularized crystal plasticity model, a two-dimensional simulation of fatigue crack growth in a compact tension (CT) specimen was performed under low-cycle fatigue conditions. A maximum tensile load of 220 N was applied cyclically over 400 cycles. To resolve fine-scale crack path features and local gradients in damage, a highly refined mesh was employed in the vicinity of the crack tip, with an element size of $10\,\mu$m.

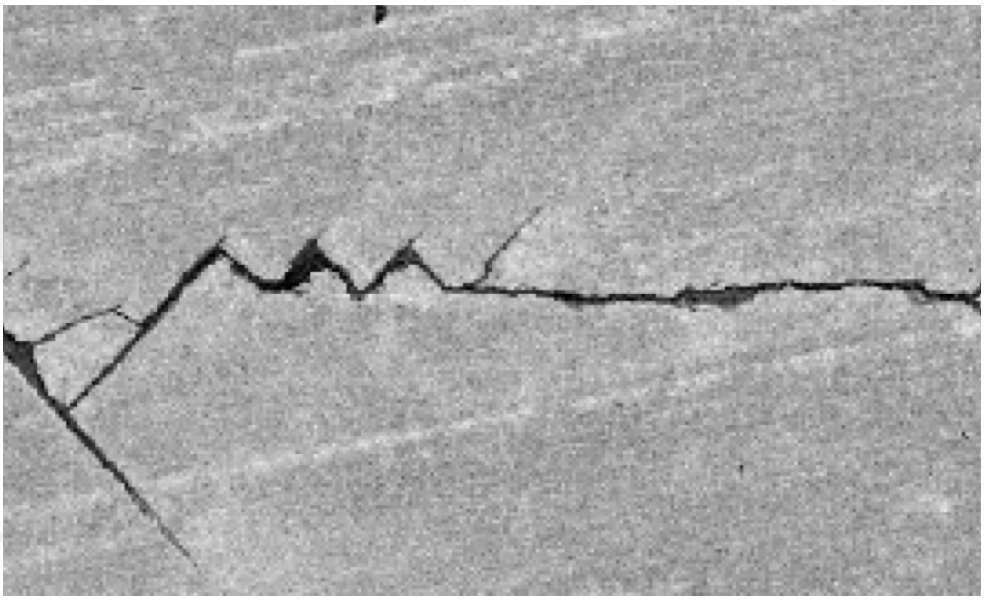

Figure 4.9: Experimental crack path in a PWA1483 single crystal CT specimen at 950°C [106].

Figure 4.9 shows the experimentally observed crack path in a PWA1483 CT specimen at 950°C, reported by Marchal et al.[106]. The crack initially branches near the notch, forming two separate paths, one of which eventually arrests as the other continues to propagate along a flatter trajectory. Further along, the path exhibits a zig-zag pattern inclined approximately at 45°, indicative of crystallographic influence on the propagation direction, and eventually a secondary bifurcation appears. These complex features — branching, crack arrest, zig-zag growth, and bifurcation — offer a rigorous reference point for evaluating the numerical model.

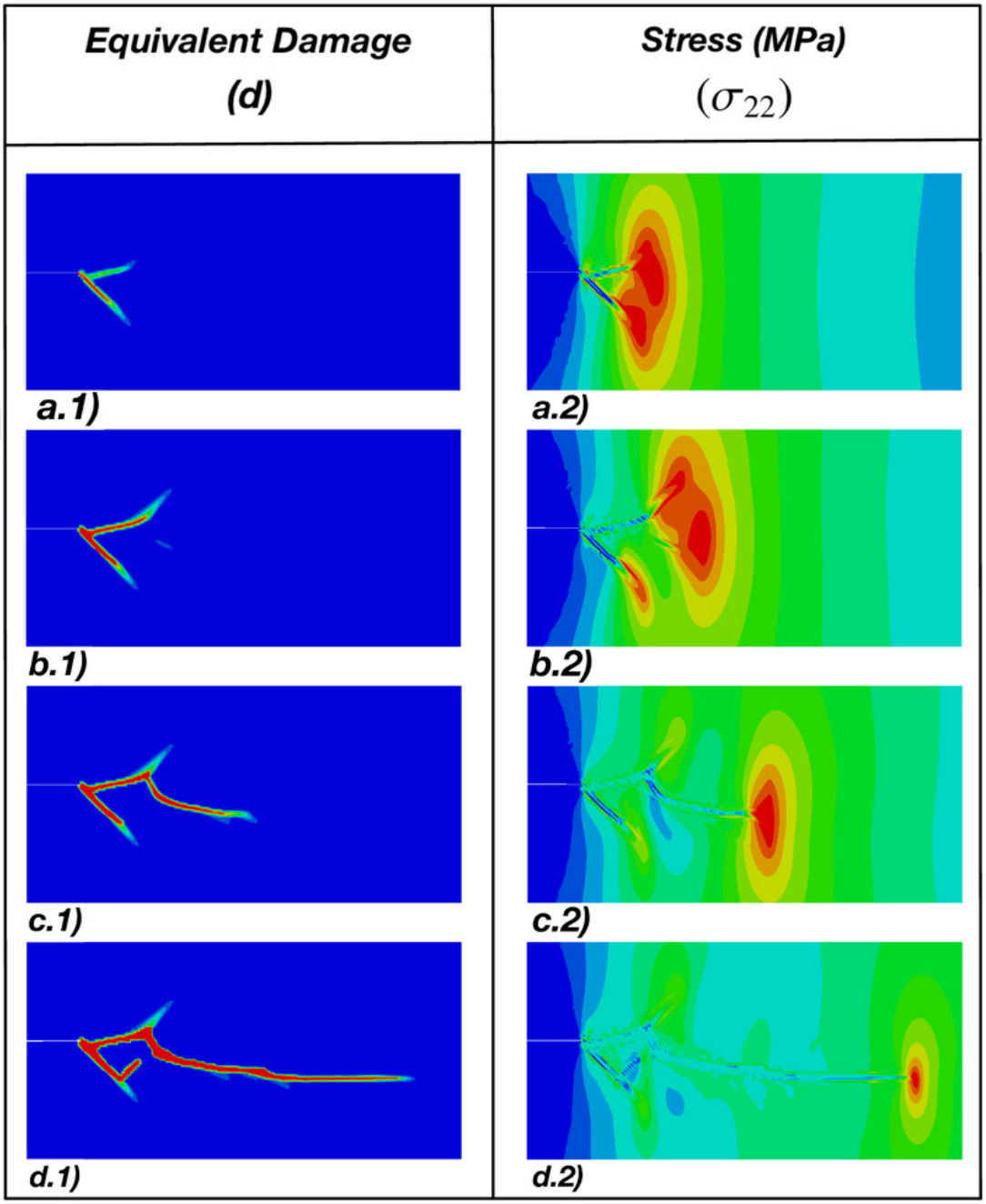

Figure 4.10: Damage field of center region (at the left side) and stress field at the crack tip (right side) a) First cycle b) Cycle 25 c) Cycle 100 d) Cycle 400.

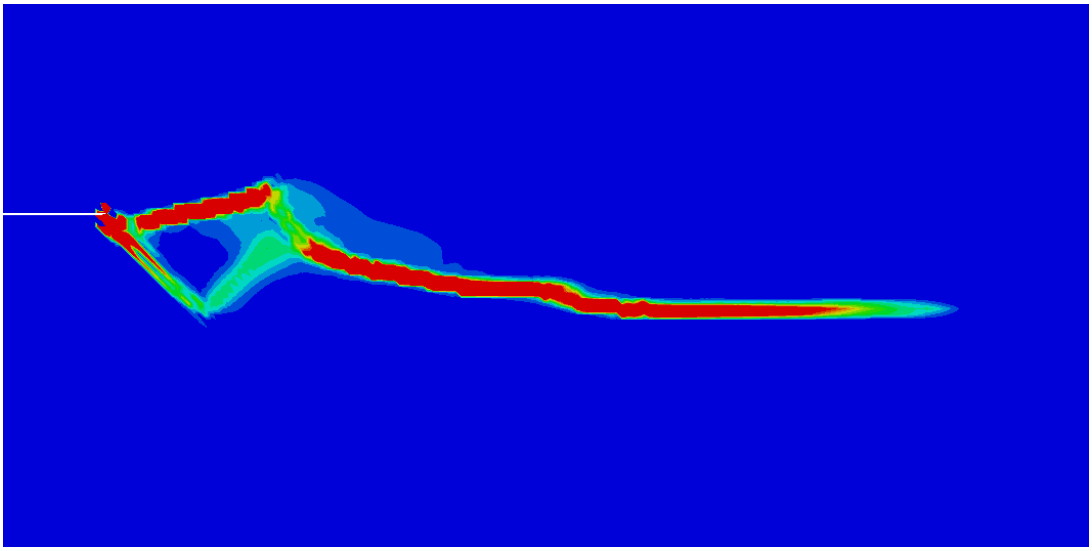

Figure 4.11: Equivalent plastic strain field after 400 cycles.

The corresponding simulation result is presented in Figure 4.10, showing the damage field after 400 loading cycles. The model successfully captures the essential features observed in the experiment. It reproduces the initial crack branching at the notch root and the subsequent selection of one dominant propagation path, as well as the emergence of a secondary bifurcation further ahead. While the zig-zag propagation is not fully realized, likely due to limitations in mesh resolution, the numerical crack path nonetheless reveals the model's sensitivity to underlying anisotropy and strain localization. An important physical feature evident in this result is the tracking behavior of the stress field. The stress concentrates around the crack tip and follows its progression with each cycle, while regions of completed damage show clear stress relaxation. During bifurcation, the stress field splits into multiple focal zones, aligning with the physically expected transition toward multiple potential propagation directions. This ability to capture crack-tip stress dynamics underscores the model's robustness in reflecting real crack behavior.

To investigate the interaction between damage and plasticity during fatigue crack growth, the equivalent plastic strain field is shown in Figure 4.11. The region along the main propagation path exhibits substantial plastic activity, consistent with a plasticity-driven fatigue mechanism. However, in the branching and bifurcation zones, plasticity is markedly reduced. This transition signifies that, in those regions, the crack grows in

a more brittle-like manner, governed not by plastic flow but by the directionality and gradients of the damage field. This behavior emerges naturally from the model's internal structure, in which the evolution of damage is coupled to plastic dissipation but can continue independently once the plastic threshold is reached. Thus, crack propagation is dictated by plasticity in the stable growth regime, while during instabilities such as branching, the damage evolution overtakes and governs the path selection.

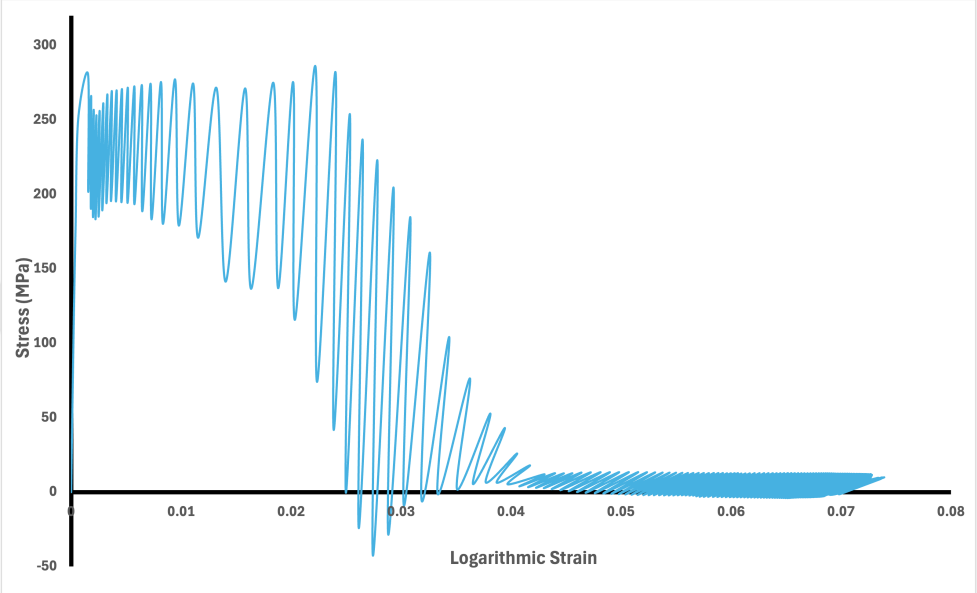

Figure 4.12: Global stress–strain response of the specimen under cyclic loading. Progressive softening and final stress collapse are observed.

The macroscopic response of the specimen under cyclic loading is presented in Figure 4.12, where the global stress is plotted against logarithmic strain. Initially, the material exhibits a characteristic cyclic hardening response, followed by progressive softening as plasticity and damage accumulate. As critical elements begin to fail due to excessive damage, a sharp decline in stress is observed, marking the onset of macroscopic fracture. Notably, the model does not exhibit any unphysical crack healing during the compressive phase of the cycles. Once damage is initiated, it irreversibly grows, consistent with the thermodynamic irreversibility embedded in the damage evolution law. This behavior is crucial for capturing realistic fatigue degradation in single crystals, where microcrack closure does not fully reverse prior material weakening.

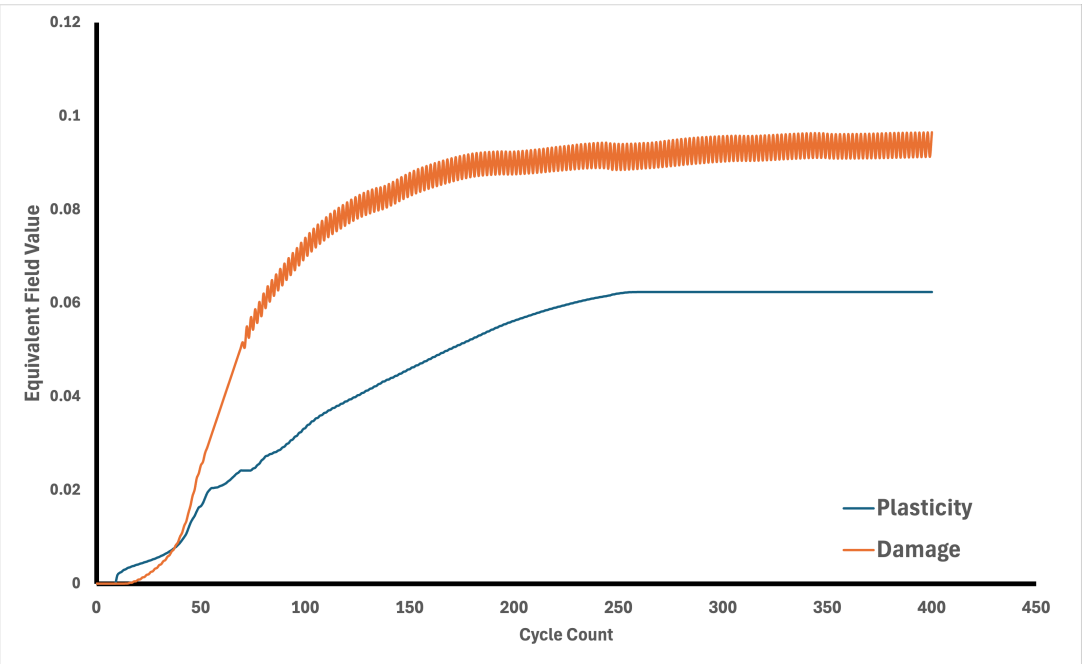

Figure 4.13: Cycle-by-cycle evolution of spatially averaged equivalent damage and plasticity fields.

Further insight into the competing roles of plasticity and damage is provided in Figure 4.13, where the spatially averaged field values are plotted as functions of the fatigue cycle count. Both quantities increase during the early cycles, reflecting coupled deformation and degradation mechanisms. However, beyond roughly 250 cycles, the plastic strain saturates while the damage field continues to grow. This marks a transition in the dominant failure mechanism: from a plasticity-controlled crack growth phase to a damage-driven regime where elements fail without further plastic deformation. This separation between the roles of damage and plasticity — both in time and in space — is a direct consequence of the model's microforce-based formulation and its use of internal length scales to regularize strain localization.

In conclusion, the 2D simulation results demonstrate that the proposed framework is capable of reproducing key features of fatigue crack growth observed experimentally, including crack branching, stress field redistribution, the transition from ductile to brittle-like behavior, and the saturation of plasticity. These observations highlight the physical realism and predictive strength of the microdamage-regularized crystal plasticity model under cyclic loading.

4.3.3.2 3D Simulation Results

Following the two-dimensional analysis, a three-dimensional simulation was carried out to investigate the full spatial characteristics of crack propagation under monotonic loading using the same compact tension (CT) specimen geometry. The specimen was discretized using C3D8 brick elements with element dimensions of $50 \times 50 \times 100\,\mu$m in the refined crack zone. A total of 30 elements were assigned across the 3 mm thickness, yielding sufficient resolution to capture through-thickness gradients. This mesh configuration, implemented via a user-defined element (UEL), enabled localization phenomena to emerge that are inaccessible in planar models. Due to the computational cost, the mesh was kept coarser than in 2D. Moreover, to mitigate convergence issues typical in 3D nonlinear simulations, the microdamage model was implemented using an explicit time integration scheme. As a result, the loading was applied monotonically to examine qualitative crack path behavior, rather than simulating cyclic fatigue life.

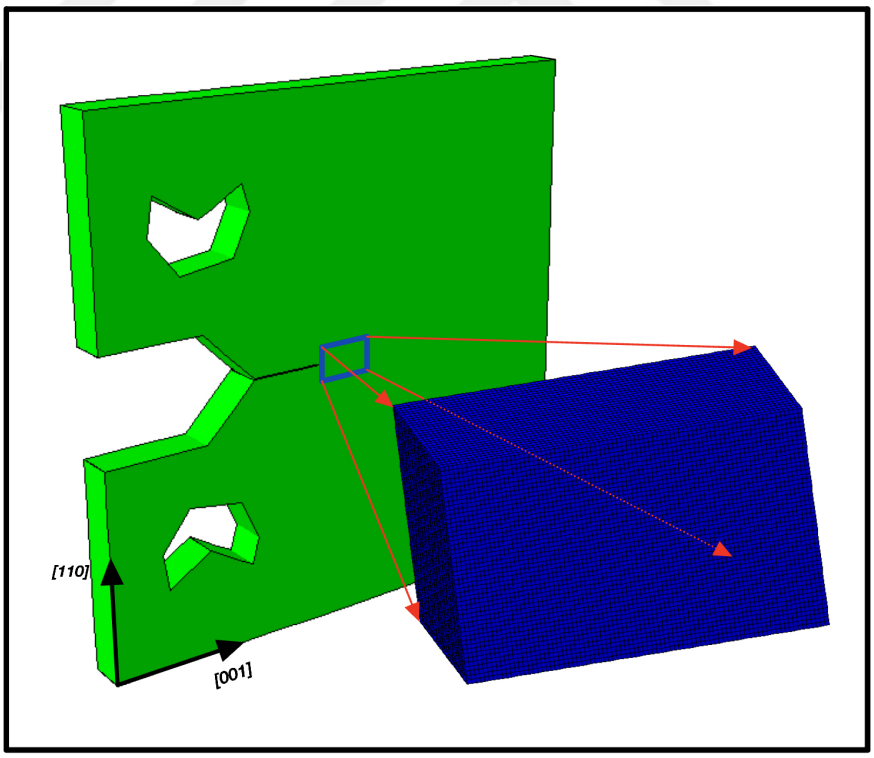

Figure 4.14: Three-dimensional CT specimen with custom UEL brick elements. The refined region is meshed with $50 \times 50 \times 100$ μm C3D8 elements, with 30 elements through the 3 mm thickness.

The overall 3D model is shown in Figure 4.14. While the geometry matches that of the 2D case, the discretization and formulation differ significantly. The simulation strategy here focuses on understanding the out-of-plane effects and the spatial evolution of crack fronts in a three-dimensional stress state, where stress triaxiality, free surface effects, and nonuniform constraint conditions play critical roles.

Figure 4.15 shows the damage field on three key cross sections. A clear crack bifurcation is observed at the notch root, consistent with the earlier 2D simulation. However, 3D results reveal additional detail. On the middle surface, crack propagation initiates early and proceeds preferentially along the crystallographic [111] direction, in line with anisotropic fracture behavior in nickel-based single crystals. Interestingly, although the crack tip is ahead in the middle layer, the outer surface already exhibits premature damage accumulation. This suggests that stress concentration initiates at the outer boundary, likely due to reduced constraint and surface effects, but the internal stress state becomes critical first. The center of the specimen accumulates sufficient energy for damage evolution earlier than the free surfaces, owing to higher triaxiality and confinement. As the crack propagates, damage spreads toward the outer surfaces. These observations reinforce the need for full 3D modeling when analyzing through-thickness variations in crack-driving forces.

Figure 4.16 displays the equivalent plastic strain field on the same cross sections. In contrast to the damage field, plasticity is more prominent at the outer surfaces than at the mid-thickness region. This apparent decoupling arises from two complementary mechanisms. First, on the outer surface, plasticity accumulates due to the dimple effect — a local compressive stress state resulting from free surface boundary conditions — which activates plastic deformation even in the absence of damage. However, because crack initiation requires tensile stress states, damage evolution is delayed in these regions. Second, at the middle surface, a strong stress localization triggers early damage accumulation. Once damage initiates, plasticity follows the damage field, softening the material and promoting further degradation. This spatial distribution shows that plasticity does not inhibit damage but rather lowers the effective resistance to it. If damage does not evolve despite plasticity accumulation, it is due to insufficient tensile stress — not because plasticity delays failure.

The asymmetry between damage and plasticity fields through the thickness is a critical feature that cannot be captured in 2D. In two-dimensional simulations, plasticity and damage were typically co-localized, except at branching or bifurcation zones. In 3D, the richer stress state enables separation of mechanisms depending on local triaxiality and boundary effects. Notably, when the coupling between damage and plasticity is increased, the resulting fields exhibit greater symmetry across the thickness, reinforcing the model's internal consistency and sensitivity to material parameters.

These 3D results demonstrate that the microdamage model successfully captures anisotropic crack propagation along the [111] direction — a feature not accessible in 2D. Moreover, the spatial divergence between damage and plastic strain localization across the specimen thickness reveals more physically accurate behavior. The observed initial crack bifurcation further validates the model, but secondary crack branching, as seen in experimental results, could not be reproduced here. This limitation is attributed to several factors: the coarser mesh required for tractable simulation time, the diffusive nature of the explicit formulation, and the convergence challenges inherent in 3D UEL implementations. These constraints prevented the resolution of finer crack features and hindered the model's ability to track complex bifurcation behavior beyond the initial stages.

As a result of these limitations, and following extensive effort toward improving 3D robustness, it was decided to adopt a phase-field regularization approach for the next stage of modeling. Phase-field models provide more control over crack path selection, offer greater numerical stability, and require less implementation effort — particularly in three-dimensional contexts. While the microdamage model remains promising, especially for capturing physical coupling mechanisms between damage and plasticity, phase-field methods for ductile single crystals offer a robust alternative capable of matching experimental crack path evolution. The formulation and results of the phase-field approach will be detailed in the next section.

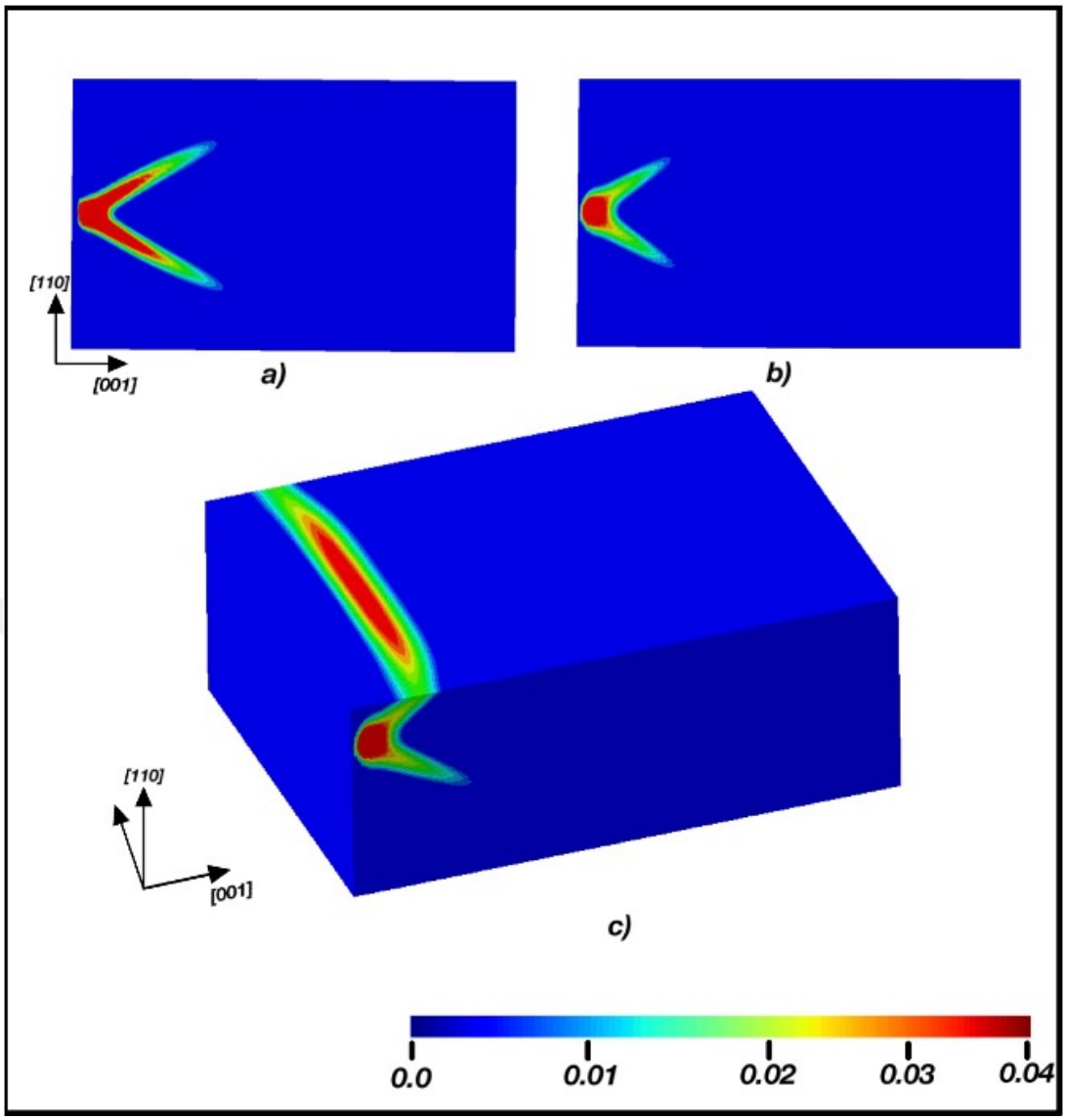

Figure 4.15: Three-dimensional damage field at final load state. (a) Middle surface (top-left), (b) Outer Surface (top-right), (c) full crack front view (bottom).

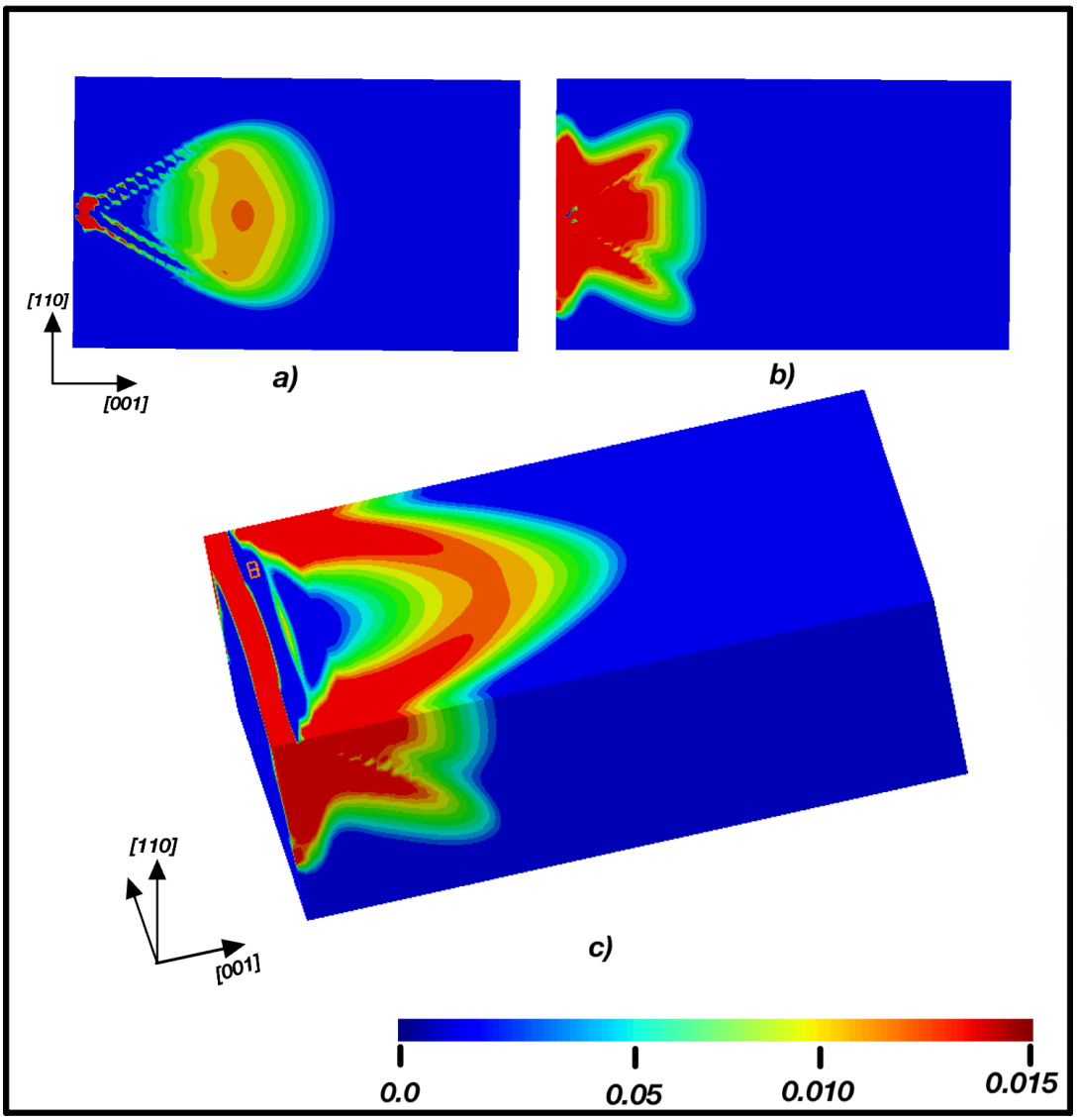

Figure 4.16: Three-dimensional equivalent plastic strain field. (a) Outer surface (top-left), (b) middle surface (top-right), (c) plasticity front view (bottom).

4.4 Phase-Field Modeling of Ductile Fracture in Single Crystal Superalloys

4.4.1 Introduction and Motivation

4.4.1.1 Evolution of Phase Field Fracture Modeling

The evolution of fracture modeling has undergone a significant transformation, starting with the pioneering work of Griffith [108], which introduced an energy-based

criterion for brittle crack propagation. Although Griffith's theory offered a profound thermodynamic perspective, it remained limited to linear elastic, isotropic materials and was incapable of predicting complex crack patterns or ductile fracture behavior. The subsequent development of cohesive zone models and local continuum damage mechanics attempted to address some of these limitations by introducing interface mechanics and element-wise degradation, respectively. However, these approaches were hindered by severe mesh sensitivity, lack of generality in three-dimensional simulations, and inadequate treatment of complex crack topologies such as branching, merging, and curvilinear propagation.

A major breakthrough in fracture modeling was the advent of variational formulations, most notably the framework developed by Francfort and Marigo [109], which formulated crack evolution as an energy minimization problem. The Ambrosio–Tortorelli regularization [110] enabled the numerical realization of this framework via a phase-field variable $\phi \in [0, 1]$, representing the transition from intact to fully broken material. Phase-field models for brittle fracture have since become a robust tool for capturing spontaneous crack initiation and complex crack trajectories without the need for tracking discontinuities or remeshing.

4.4.1.2 Phase-Field Formulation for Ductile Fracture Coupled to Plasticity

In their initial form, phase-field models were primarily tailored for brittle fracture, where crack evolution is driven solely by the release of elastic energy. To extend this framework to ductile materials, researchers incorporated the effects of plastic deformation, giving rise to phase-field models for ductile fracture. These models typically achieve the coupling with plasticity through either energy-based or degradation-based mechanisms. One of the most widely adopted strategies is energy-driven coupling, in which the fracture driving force includes not only stored elastic energy but also the accumulated plastic work. For instance, Miehe et al. [111] introduced a model that incorporates dissipated plastic energy into a history variable governing the phase-field evolution, enabling the model to capture critical features of ductile fracture such as void nucleation, growth, and the ductile-to-brittle transition. Alternatively, degradation-driven coupling has been proposed, wherein the phase-field vari-

able modulates the material's stiffness or yield strength, thereby influencing plasticity indirectly. This approach, examined by Alessi et al. [112], was compared with energy-based coupling, with the latter found to better reflect experimental observations of ductile failure. Furthermore, a key ingredient in phase-field models is the appropriate decomposition of fracture-driving energy to ensure physical consistency under complex loading states, especially in cyclic or compressive regimes. Techniques for decomposing the total energy into tensile and compressive parts, or into deviatoric and volumetric components, have been widely adopted to prevent unphysical crack closure or healing. Seminal contributions in this direction were made by Ambati et al. [113] and later generalized by Wu [114], who established thermodynamically consistent guidelines for fracture energy decomposition.

4.4.1.3 Anisotropy and Single-Crystal Considerations in Phase-Field Fracture

Modeling ductile fracture in single crystal superalloys introduces additional layers of complexity due to the pronounced anisotropy inherent in their elastic, plastic, and fracture behavior. The elastic anisotropy arising from the crystallographic structure of cubic materials significantly affects stress distributions around crack tips and, consequently, the crack propagation paths. To accurately capture these effects, phase-field models must incorporate orientation-dependent stiffness tensors, as demonstrated by Borden et al. [115]. In addition to elastic anisotropy, the anisotropy of fracture toughness plays a critical role, particularly in cleavage-dominated fracture modes. This behavior is typically modeled by assigning an orientation-dependent fracture energy $\mathcal{G}_c$, which enables the simulation of experimentally observed fracture patterns in single crystals [116]. Beyond anisotropic elasticity and toughness, the integration of crystal plasticity formulations into the phase-field framework further enhances the model's ability to simulate damage processes in single crystals. Such formulations account for anisotropic hardening, crystallographic slip, and lattice rotation, thus enabling the study of fracture in conjunction with evolving microstructural features. Recent works by Li et al. [117] and Mozaffari et al. [118] have advanced this direction by implementing crystal plasticity phase-field models capable of capturing the interactions between slip-induced damage and crack evolution. These models demonstrated the ability to simulate complex fracture phenomena such as anisotropic crack growth.

4.4.1.4 Advantages of Phase-Field over Conventional Damage Models

Compared to conventional damage models, the phase-field framework provides several compelling advantages that make it especially attractive for simulating ductile fracture in single crystal superalloys. One of the most notable strengths is its inherent mesh objectivity, achieved through the introduction of a regularization length scale ℓ, which ensures that energy dissipation remains independent of spatial discretization [119]. Furthermore, the diffuse crack representation enables automatic crack initiation and path prediction as an outcome of the energy minimization principle, eliminating the need for ad hoc criteria or crack tracking algorithms. The method is also numerically robust, with the absence of discontinuities promoting stable convergence under conditions involving large deformations and nonlinearities. Beyond robustness, the phase-field approach offers a unified variational structure that naturally accommodates the coupling of fracture with other physical mechanisms, such as plasticity, within a thermodynamically consistent framework [115, 112]. This flexibility allows for physically meaningful calibration and parameter interpretation. Another critical advantage lies in its ability to capture complex three-dimensional crack topologies, including branching and merging, without additional tracking algorithms. Finally, the formulation is readily applicable to finite strain kinematics and complex multiaxial loading scenarios, as demonstrated in recent contributions such as Shi et al. [120]. Taken together, these features establish the phase-field method as a rigorous, versatile, and predictive modeling framework that overcomes key limitations of classical damage theories and supports advanced applications in crystal plasticity and anisotropic fracture. The subsequent section introduces the specific mathematical formulation employed in this work.

4.4.2 Theoretical Framework for Crystal Plasticity Phase-Field Modeling

The coupled crystal plasticity phase-field fracture model employed in this work builds upon the variational and thermodynamically consistent framework introduced by Miehe et al. [111], and extends it by integrating a finite strain crystal plasticity formulation. The key idea is to represent crack evolution via a scalar phase-field variable $\phi \in [0, 1]$, which continuously transitions the material from the intact state ($\phi = 0$)

to fully broken ($\phi = 1$), removing the need to explicitly track discontinuities. The phase-field approach is embedded within a total energy minimization framework that captures the interaction between elastic deformation, plastic dissipation, and fracture.

4.4.2.1 Free Energy Decomposition and Regularization

The Helmholtz free energy density ψ is decomposed into three parts: elastic strain energy, plastic dissipation potential, and fracture energy:

$$\psi = g(\phi)\,\psi^{\text{el}}(\mathbf{F}_e) + \psi^{\text{pl}}(\{\gamma^\alpha\}) + \psi^{\text{frac}}(\phi, \nabla\phi) \tag{4.43}$$

where:

- $g(\phi) = (1-\phi)^2$ is the degradation function applied to the elastic energy,
- ψ^{el} is the stored elastic energy, computed from the elastic strain,
- ψ^{pl} accumulates dissipative effects due to crystallographic slip,
- ψ^{frac} is the regularized fracture energy density defined as:

$$\psi^{\text{frac}} = \frac{G_c}{2\ell}\phi^2 + \frac{G_c\ell}{2}|\nabla\phi|^2 \tag{4.44}$$

  where G_c is the critical energy release rate, and ℓ is a material length scale that controls the width of the diffused crack zone.

4.4.2.2 Multiplicative Kinematics and Anisotropic Elasticity

Under finite deformation, the total deformation gradient $\mathbf{F}$ is decomposed multiplicatively as:

$$\mathbf{F} = \mathbf{F}_e\mathbf{F}_p \tag{4.45}$$

where $\mathbf{F}_p$ accounts for irreversible plastic slip on crystallographic systems, and $\mathbf{F}_e$ is the elastic part. The elastic energy is evaluated from the elastic Green–Lagrange strain:

$$\mathbf{E}_e = \frac{1}{2}(\mathbf{F}_e^\top \mathbf{F}_e - \mathbf{I}) \tag{4.46}$$

and for anisotropic materials, it reads:

$$\psi^{\text{el}} = \frac{1}{2}\mathbf{E}_e : \mathbb{C} : \mathbf{E}_e \tag{4.47}$$

where $\mathbb{C}$ is the fourth-order elastic tensor characterizing the crystal's anisotropy (e.g., cubic symmetry).

4.4.2.3 Plastic Dissipation and Slip System Kinetics

Plastic deformation occurs through slip on predefined crystallographic systems α, with each system characterized by its resolved shear stress τ^α and shear rate $\dot{\gamma}^\alpha$. The cumulative plastic dissipation is given by:

$$\psi^{\text{pl}} = \sum_\alpha \int_0^t \tau^\alpha \dot{\gamma}^\alpha \, dt. \tag{4.48}$$

The evolution of shear on each system is governed by a rate-dependent flow rule:

$$\dot{\gamma}^\alpha = \left\langle \frac{|\tau^\alpha| - r^\alpha}{K} \right\rangle^n \text{sign}(\tau^\alpha) \tag{4.49}$$

where r^α is the current slip resistance, K is a viscosity-like parameter, and n is the rate sensitivity exponent. Hardening laws define the evolution of r^α, typically via accumulated slip or dislocation density.

4.4.2.4 Fracture Driving Force via Work Densities

The evolution of the phase-field is governed by a thermodynamic driving force constructed from internal energy densities. Following Miehe et al., the fracture state function $\tilde{D}$ is expressed as:

$$\tilde{D} = \left\langle \frac{\tilde{w}^e + \tilde{w}^p}{w_c} - 1 \right\rangle \tag{4.50}$$

where:

- $\tilde{w}^e$ is the local elastic energy density,

- $\tilde{w}^p$ is the accumulated plastic work density,
- w_c is a critical energy threshold for damage initiation,
- The Macaulay brackets $\langle\cdot\rangle$ enforce irreversibility (ϕ evolves only when the energy exceeds the threshold).

This formulation enables the model to capture both brittle and ductile contributions to fracture. It provides a physically meaningful link between the mechanical fields and damage evolution by coupling phase-field growth to total energy input.

4.4.2.5 Governing Equations

The variational principle yields the following coupled system of equations:

- **Balance of linear momentum:**

$$\mathrm{Div}(\mathbf{P}) = \mathbf{0}, \quad \text{where } \mathbf{P} = \frac{\partial \psi}{\partial \mathbf{F}} \tag{4.51}$$

- **Crystal plasticity evolution:**
  $\dot{\gamma}^\alpha$ governed by flow rule and hardening law.
- **Phase-field evolution:**

$$\frac{G_c}{2\ell}\phi - G_c \ell \Delta\phi - \frac{\partial \tilde{D}}{\partial \phi} = 0 \tag{4.52}$$

  where $\frac{\partial \tilde{D}}{\partial \phi}$ is the variational derivative of the damage driving force with respect to the phase-field variable.

These equations are solved incrementally in time, typically using a staggered (alternating) or monolithic numerical scheme. Crack irreversibility ($\dot{\phi} \geq 0$) is enforced through history variables or penalization techniques to ensure that damage does not heal.

4.4.3 Case Study I: Single-Edge Notched Specimen

To assess the predictive capabilities of the phase-field fracture formulation in anisotropic, plastically deforming single crystals, a single-edge notched (SEN) specimen was

analyzed and compared with corresponding experimental data. The specimen was oriented with [001] along the thickness and [110] along the crack propagation direction, a crystallographic configuration representative of common failure paths in single crystal nickel-based superalloys. Under mode-I loading, this setup activates cleavage-prone {111} planes, leading to complex crack propagation behavior dominated by anisotropic fracture resistance and plasticity-mediated dissipation mechanisms.

Figure 4.17 shows a scanning electron microscope (SEM) image of the fractured surface obtained from a SEN specimen test. The initial notch leads to a prominent crack that bifurcates into two distinct branches, suggesting significant anisotropic crack path selection, likely driven by a combination of elastic anisotropy and crystallographic cleavage directions. The surface texture indicates substantial plastic deformation preceding and accompanying crack advance, typical of ductile fracture behavior in these alloys. The bifurcated path, though not symmetric, indicates that fracture evolution is governed by local energy release rates interacting with the crystallographic microstructure.

In comparison, Figure 4.18 presents the result from the numerical simulation using the phase-field fracture model coupled with crystal plasticity. The simulated crack path captures the bifurcation phenomenon remarkably well, showing a qualitatively similar geometry to the experimental observation. The bifurcation emerges naturally within the phase-field framework, without any geometric prescription or crack tracking algorithm. This predictive capability stems from the variational structure of the model, which governs fracture evolution through energy minimization principles. As the simulation evolves, the crack propagates in directions that minimize the total internal energy—comprising both the elastic and plastic contributions—thus inherently reflecting the anisotropic fracture behavior of the crystal.

An important aspect of the phase-field approach employed here is that it does not explicitly model damage in the conventional sense (e.g., stiffness degradation via scalar damage variables). Instead, it relies on an energy-based criterion wherein crack propagation is driven by accumulated energy densities. In the context of ductile fracture, where plastic deformation significantly contributes to energy dissipation, the plastic work density acts as a key driver for phase-field evolution. This makes the model

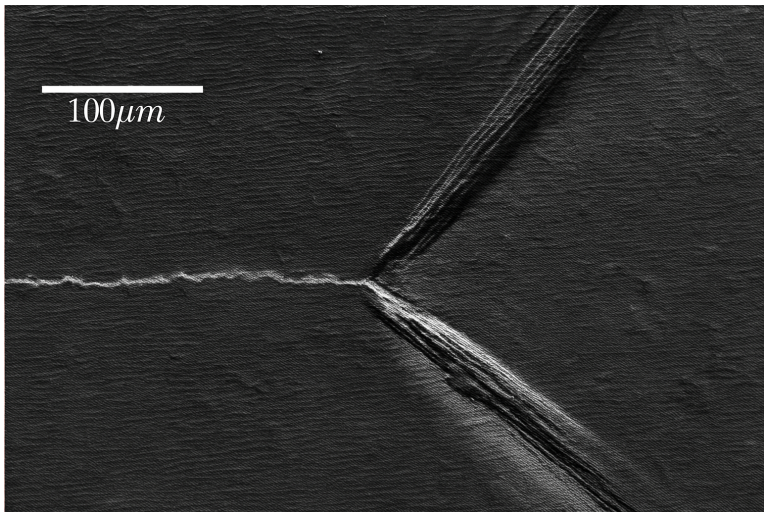

Figure 4.17: Experimental fracture surface of single crystal (001)[110] under mode-I loading.

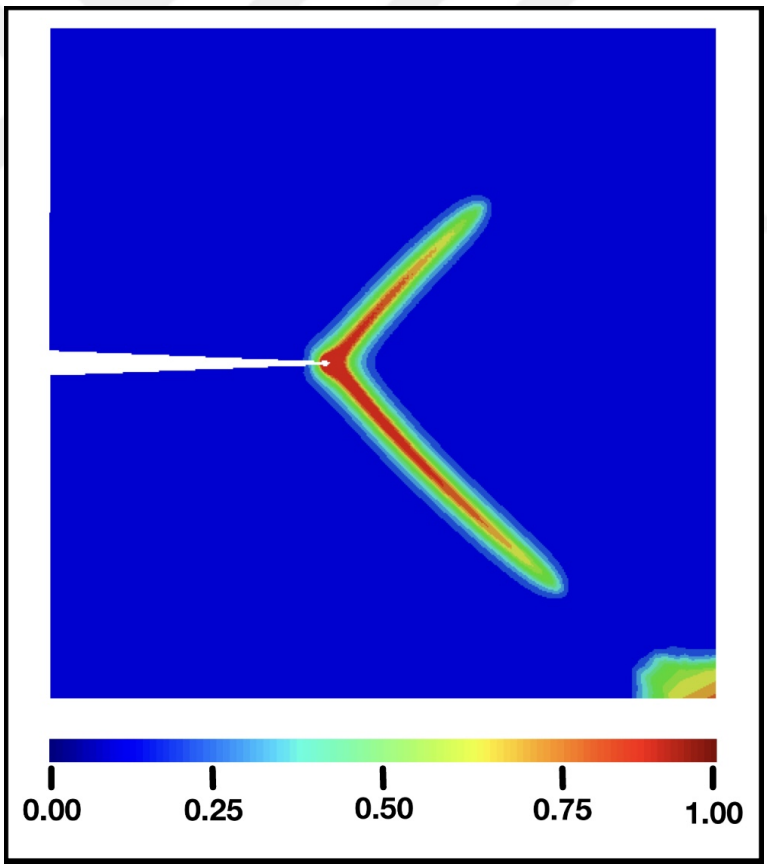

Figure 4.18: Phase-field simulation result showing bifurcated crack propagation in the same SEN specimen configuration.

particularly suitable for capturing ductile fracture behaviors. The experimental specimen displays pronounced plasticity ahead of the crack tip, and in regions of bifurcation, the fracture follows paths associated with maximum energy release—mirrored in the phase-field simulation by the emergence of damage contours along the same directions. The strong agreement in the crack path trajectory supports the conclusion that, when plastic energy dominates the field—as is the case in ductile materials—the phase-field model can accurately reproduce experimentally observed fracture morphologies.

The smooth, continuous nature of the simulated crack also reflects the regularizing effect of the internal length scale parameter in the phase-field method. This diffused representation aligns well with experimental fracture surfaces where the transition from microvoid coalescence to macroscopic crack faces occurs over a finite zone rather than a sharp interface. As such, the method provides a physically consistent description of the crack front without the need for ad hoc criteria or cohesive elements.

In summary, the SEN specimen simulation demonstrates that the phase-field fracture model, when coupled with a crystal plasticity framework, can successfully predict complex fracture behaviors including bifurcation and anisotropic propagation in ductile single crystal materials. The ability to account for both plastic and elastic energy contributions in a unified variational setting enables this approach to reflect the key physical mechanisms that govern fracture in experimentally relevant configurations.

4.4.4 Case Study II: Double Edge Notched Specimen

To evaluate the predictive capabilities and limitations of the microdamage and phase-field fracture models under complex loading and crack evolution scenarios, simulations were conducted on a double edge notched (DEN) specimen subjected to uniaxial tension. The geometry of the specimen and its finite element discretization are shown in Figure 4.19. The specimen was clamped at the bottom and a vertical tensile force was applied at the top. Owing to the expected high stress gradients and localized inelastic activity near the notch roots, the central region of the specimen was meshed with high refinement, while the surrounding regions used a coarser mesh to ensure computational efficiency.

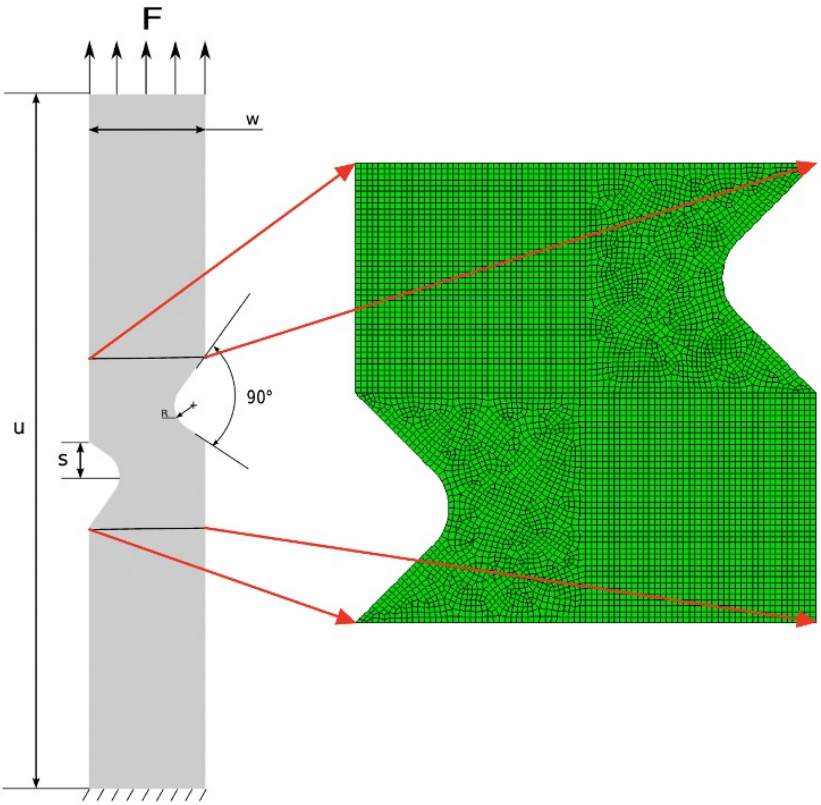

Figure 4.19: Geometry and mesh structure of the double edge notched specimen. Central region is finely meshed to resolve high gradients near the notch.

Simulation results for both fracture models are shown in Figure 4.20, alongside an experimental image obtained from a comparable tensile test on a single crystal superalloy specimen. The experimental observation reveals a two-stage crack evolution process: initially, a crack initiates from the notch root and propagates horizontally across the ligament, aligned with a crystallographically favorable direction. After a certain extent of propagation, the fracture path reorients and continues along a diagonal trajectory, indicative of a change in the dominant fracture mechanism and stress state.

The microdamage model successfully reproduces this two-stage fracture evolution. Initially, damage nucleates at the notch tips and propagates along a horizontal direction, reflecting the anisotropic stiffness degradation that is intrinsic to the model.

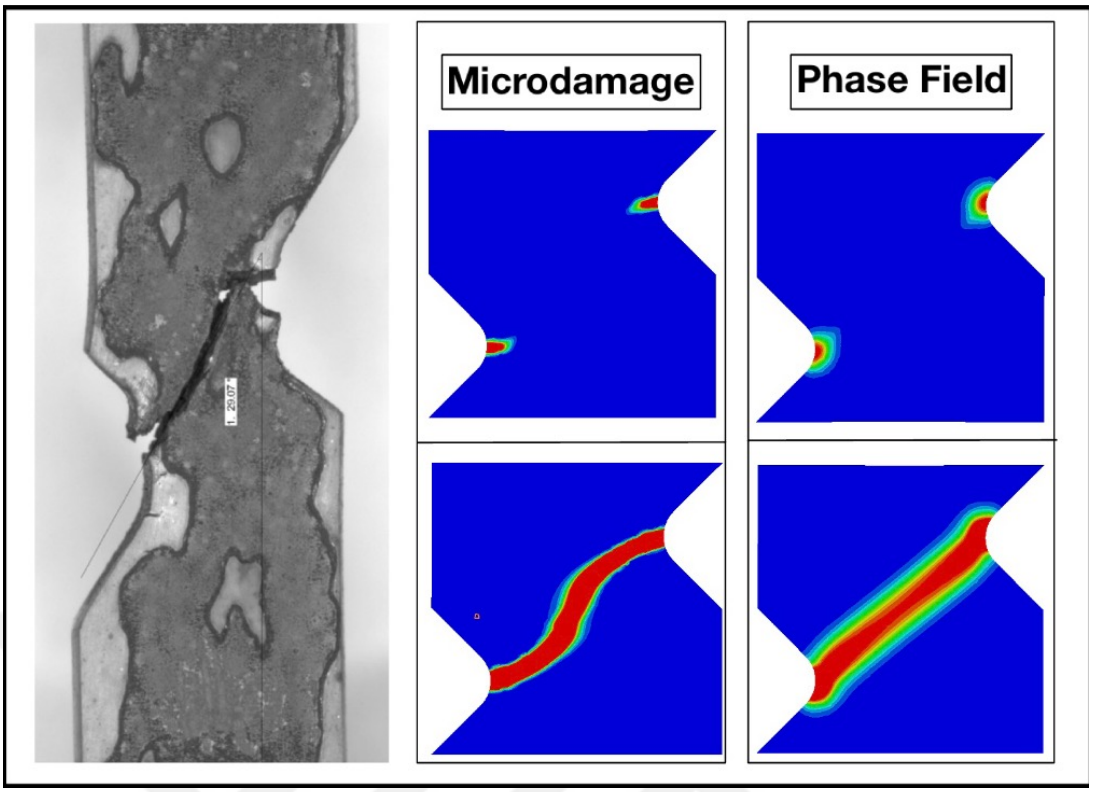

Figure 4.20: Comparison of experimental, microdamage, and phase-field fracture patterns in a double edge notched specimen.

As the crack propagates and the local stress field evolves, the model captures the onset of a secondary crack path that deviates from the initial orientation, following a diagonal direction. This transition corresponds to the increased stress intensity and strain localization that develops due to progressive damage accumulation and plastic deformation. Although the microdamage model relies on a scalar internal variable, it incorporates directional sensitivity through projection tensors defined on crystallographic orientations. Interestingly, despite these anisotropic ingredients, the simulated crack paths in this case remained relatively unaffected by orientation. This implies that, under the specific loading and boundary configuration, the global stress field dominated the fracture trajectory.

In contrast, the phase-field model produces qualitatively different results. The initial crack initiation is accurately predicted, owing to the model's strong dependence on plastic energy release and the associated localization near the notch root. This agreement highlights the strength of the phase-field approach in capturing ductile

fracture phenomena where plastic dissipation dominates the fracture driving force. However, the model fails to reproduce the distinct change in crack direction observed experimentally. Rather than arresting and re-nucleating along a new path, the crack continues along a smeared, energetically favorable trajectory. This limitation arises not from the scalar nature of the damage variable but from the isotropic character of the crack-driving mechanism and the fracture energy dissipation formulation. Unlike the microdamage model, which accounts for directional degradation in stiffness, the current phase-field implementation treats fracture in a directionally neutral manner.

Physically, this comparison underscores the relative strengths of the two approaches in different fracture regimes. When plasticity dominates the energy release process, the phase-field model provides a smooth and predictive evolution of the crack front. However, in damage-driven or orientation-sensitive fracture scenarios, especially where crack redirection occurs due to stress redistribution and anisotropic constraints, the microdamage model captures the physical behavior more accurately.

From a computational perspective, the phase-field model offers several advantages, including improved convergence properties and easier implementation within a variational framework. Its length scale parameter is well-defined and physically interpretable, offering consistent control over the diffused crack zone. However, the same diffuse nature can be a drawback when modeling sharp crack transitions. On the other hand, the microdamage model, while more susceptible to convergence issues under severe localization, provides a more localized representation of damage and better sensitivity to complex fracture topologies.

In summary, the phase-field model is well-suited for plasticity-dominated fracture but requires further enhancements—such as anisotropic fracture energy or directional degradation—for broader applicability to damage-sensitive and anisotropic crack growth phenomena. The microdamage model, although computationally more demanding, demonstrates improved physical agreement in such regimes and serves as a valuable reference for advancing phase-field approaches.

CHAPTER 5

Conclusions

This thesis presents a computational framework for modeling the fatigue crack behavior of nickel-based single crystal superalloys, focusing on the coupling between crystal plasticity and damage evolution under severe cyclic loading. The work is motivated by the critical role of these materials in aerospace propulsion systems, particularly turbine blades, where accurate prediction of crack initiation and growth under high-temperature, multiaxial, and cyclic stress states is essential for ensuring component safety and performance.

A robust, finite strain crystal plasticity model was developed and implemented through a user-defined UMAT subroutine in Abaqus. The model incorporates anisotropic plastic slip based on crystallographic mechanisms, rate-dependent flow rules, and an implicit time integration scheme supported by a consistent tangent operator. This formulation enables the simulation of realistic single crystal deformation behaviors including orientation-dependent hardening, slip system activation, and cyclic response. Validation against analytical solutions such as Rice's localization theory, as well as numerical benchmarks including compact tension and tension–torsion specimens, confirmed the model's ability to reproduce experimentally observed patterns such as shear band formation and asymmetric stress evolution.

Central to this thesis is the formulation and implementation of a microdamage continuum model to describe fatigue crack initiation and propagation. Based on gradient regularization, the microdamage model introduces a physically motivated internal length scale that stabilizes numerical solutions and eliminates mesh sensitivity. This regularization is particularly important for capturing damage localization in high-

gradient fields, and enables objective simulation of fatigue degradation. Notably, the model reproduces bifurcation and branching of fatigue cracks in a manner consistent with experimental observations in single crystal alloys. These results demonstrate the model's predictive power in identifying not only the location and mode of crack initiation, but also the path and morphology of crack growth under cyclic loading.

Three-dimensional implementation of the microdamage model represents a novel contribution to the literature. Most prior applications of gradient damage models are limited to two-dimensional settings; extending this framework to 3D allows for a more realistic representation of damage evolution in engineering components. The simulations revealed spatial separation between plasticity and damage fields, highlighting the importance of stress triaxiality and dimple formation in governing crack development. These findings underscore the physical value of gradient-based modeling in resolving stress concentrations and tracking the accumulation of plastic slip in critical zones—features that are particularly relevant for aerospace applications where fatigue life prediction depends on local microstructural behavior. Although the 3D implementation introduces significant computational challenges, its ability to resolve physically meaningful features makes it a compelling tool for future investigations.

To address limitations associated with crack path resolution, a complementary modeling approach based on the phase-field method was implemented. The phase-field formulation for ductile fracture offers a diffuse, variational representation of crack surfaces that naturally handles complex phenomena such as branching, merging, and coalescence. Coupled with the underlying crystal plasticity model, this approach enables simulation of fatigue-induced fracture without predefined crack geometries. Phase-field modeling has emerged as a promising and active area of research in fracture mechanics, offering a mathematically consistent and thermodynamically grounded alternative to conventional damage and cohesive zone models. The results in this thesis show that the phase-field method is capable of representing complex fracture topologies in three dimensions, making it highly relevant for future high-fidelity simulation efforts in structural integrity assessment.

A comparative analysis between the microdamage model and the phase-field formulation was conducted to evaluate their respective strengths. The microdamage model

excels in computational efficiency and in representing mesh-objective, physically interpretable damage evolution tied closely to plastic deformation mechanisms. In contrast, the phase-field model is more general in its ability to capture evolving crack topology and remains robust under severe localization. Both methods serve complementary purposes within the larger objective of accurately simulating fatigue fracture in high-performance materials.

From a practical standpoint, the ability to simulate stress concentrations and the evolution of plastic slip in the vicinity of geometric discontinuities such as holes, notches, and fillets is highly valuable for aerospace component design. Accurately capturing these effects allows for better estimation of fatigue life, more informed placement of inspection points, and optimized use of materials under design constraints. As the industry moves toward more predictive, simulation-driven certification of structural components, models such as those developed in this thesis have the potential to serve as foundational tools in the digital design and life assessment workflow.

Future work should focus on extending the current framework to address additional physical mechanisms relevant to high-temperature service environments. This includes the incorporation of time-dependent creep behavior, oxidation effects, and full thermo-mechanical coupling. Modeling polycrystalline microstructures, either through mean-field approaches or direct simulation of grain aggregates, would allow application of the framework to broader classes of nickel-based superalloys. Further development of the 3D phase-field simulations—including adaptive meshing, parallelization, and improved solution algorithms—will be essential for achieving practical scalability. Another promising avenue is the introduction of multiplane damage criteria, which could enhance the ability to simulate crack deflection and mixed-mode fracture observed in complex loading conditions.

In conclusion, this thesis offers a physically grounded, numerically stable, and extensible modeling platform for predicting fatigue fracture in single crystal superalloys. Through the development of advanced crystal plasticity, microdamage continuum, and phase-field formulations, the work bridges theoretical modeling and practical engineering needs, offering valuable insights into the mechanisms of failure in critical aerospace materials.

The groundwork laid here is expected to serve as a stepping stone for future research in fatigue, fracture, and high-temperature structural integrity modeling.

REFERENCES

[1] N. E. Prasad and R. J. H. Wanhill, *Aerospace Materials and Material Technologies*. Springer, 2017.

[2] H. I. H. Saravanamuttoo, G. F. C. Rogers, and H. Cohen, *Gas Turbine Theory*, 6th ed. Pearson, 2008.

[3] R. C. Reed, *The Superalloys: Fundamentals and Applications*. Cambridge University Press, 2006.

[4] M. J. Donachie and S. J. Donachie, *Superalloys: A Technical Guide*. ASM International, 2002.

[5] T. M. Pollock and S. Tin, "Nickel-based superalloys for advanced turbine engines: Chemistry, microstructure, and properties," *J. Propul. Power*, vol. 22, no. 2, pp. 361–374, 2006.

[6] Ö. Aslan, "High Temperature Mechanical Behaviour of New Generation Single Crystal Superalloys," Ph.D. dissertation, École des Mines de Paris, 2010.

[7] A. F. Giamei, "Development of single crystal superalloys: A brief history," *Adv. Mater. Processes*, vol. 171, no. 9, pp. 26–30, 2013.

[8] K. Harris, "Advanced single crystal superalloys," *MRS Bull.*, vol. 18, no. 3, pp. 45–52, 1993.

[9] G. R. Leverant and B. H. Kear, "Refractory metal additions to nickel-based superalloys," *Metall. Trans.*, vol. 1, no. 3, pp. 491–498, 1970.

[10] P. Caron and T. Khan, "Evolution of Ni-based superalloys for single crystal gas turbine blade applications," *Aerosp. Sci. Technol.*, vol. 1, no. 3, pp. 139–151, 1997.

[11] R. C. Reed, N. Matan, D. C. Cox, M. A. Rist, and C. M. F. Rae, "Creep of CMSX-4 superalloy single crystals," *Mater. Sci. Eng. A*, vol. 245, no. 1, pp. 150–168, 2008.

[12] T. V. Rajan, C. P. Sharma, and A. Sharma, *Heat Treatment: Principles and Techniques*. PHI Learning Pvt. Ltd., 2011.

[13] D. W. MacLachlan, C. M. F. Rae, and R. C. Reed, "Orientation dependence of the creep and fatigue behavior of CMSX-4," *Acta Mater.*, vol. 57, no. 19, pp. 6302–6313, 2009.

[14] E. P. Busso, F. T. Meissonnier, and N. P. O'Dowd, "A 3D rate-dependent crystal plasticity model for polycrystalline metals," *Int. J. Solids Struct.*, vol. 37, no. 30, pp. 4125–4148, 2000.

[15] S. Ghosh and D. M. Dimiduk, "Computational methods for crystal plasticity," *J. Eng. Mater. Technol.*, vol. 123, no. 4, pp. 471–480, 2001.

[16] N. E. Prasad and R. J. H. Wanhill, "Superalloys," in *Aerospace Materials and Material Technologies*, Springer, 2016, pp. 220–249.

[17] R. Cozar and A. Pineau, "Morphology of γ' precipitates and thermal stability of nickel-based superalloys," *Metall. Trans.*, vol. 4, no. 1, pp. 47–59, 1973.

[18] S. Tian, Z. Mao, and Y. Zhou, "Influence of Ta and Hf on the microstructure and creep behavior of nickel-base single crystal superalloys," *Mater. Sci. Eng. A*, vol. 558, pp. 463–470, 2012.

[19] H. Yamagata, T. Ohta, H. Nakayama, H. Harada, and M. Osawa, "Effect of ruthenium on the phase stability of fourth-generation Ni-base single crystal superalloys," *Metall. Mater. Trans. A*, vol. 32, no. 4, pp. 949–956, 2001.

[20] P. Caron, "Recent developments in gamma prime-strengthened single crystal superalloys," *J. Eng. Gas Turbines Power*, vol. 122, no. 4, pp. 465–475, 2000.

[21] E. Simonetti *et al.*, "Rhenium effects in Ni-based single crystal superalloys: A review," *Superalloys 2004*, pp. 803–812, 2004.

[22] B. Décamps, P. Caron, and T. Khan, "The effect of ruthenium on the microstructural stability of Re-containing single-crystal superalloys," *Superalloys 2004*, pp. 863–870, 2004.

[23] K. L. Harris, J. L. Smialek, and C. A. Barrett, "Effects of Cr and Al contents on oxidation resistance of Ni-based superalloys," *Oxid. Met.*, vol. 38, no. 3–4, pp. 287–307, 1992.

[24] A. C. Yeh *et al.*, "Microstructural development of next-generation single crystal Ni-based superalloys," *Superalloys 2008*, pp. 911–918, 2008.

[25] T. B. Massalski, Ed., *Binary Alloy Phase Diagrams*, 2nd ed. ASM International, 1990.

[26] K. Kakehi, "Effect of cooling rate on the microstructure and mechanical properties of a nickel-base single crystal superalloy," *Mater. Sci. Eng. A*, vol. 289, no. 1–2, pp. 22–28, 2000.

[27] F. J. Humphreys and M. Hatherly, *Recrystallization and Related Annealing Phenomena*. Elsevier, 2004.

[28] T. Gladman, "Precipitation hardening in metals," *Mater. Sci. Technol.*, vol. 15, no. 1, pp. 30–36, 1999.

[29] M. K. Miller, M. J. Mills, and E. A. Kenik, "The γ–γ' microstructure of Ni-based superalloys," *Mater. Sci. Eng. A*, vol. 234–236, pp. 922–925, 1997.

[30] F. Hanriot, G. Cailletaud, and L. Remy, "High temperature constitutive modeling - Theory and application, chapter Mechanical behaviour of a nickel-based superalloy single crystal," in *ASME*, New York, 1991, pp. 139–150.

[31] P. Caron and T. Khan, "High-temperature creep properties of single crystal superalloys," *Mater. Sci. Eng. A*, vol. 234–236, pp. 67–74, 1997.

[32] Y. Hijikata, T. Sugiyama, H. Iwata, and M. Nakamura, "Temperature dependence of the tensile strength and creep strength of single crystal Ni-based superalloy," *Mater. Trans.*, vol. 48, no. 5, pp. 1037–1042, 2007.

[33] H. Fujii, K. Yoshimi, and H. Oikawa, "Mechanical behavior of a nickel-base single-crystal superalloy at high temperatures," *Mater. Sci. Eng.*, vol. 108, pp. 93–102, 1989.

[34] A. I. Epishin, T. Link, M. Staubli, and U. Glatzel, "Temperature dependence of the tensile strength of nickel-based superalloys with different orientation," *Mater. Sci. Eng. A*, vol. 319–321, pp. 802–806, 2001.

[35] T. J. Ruggles and M. V. Nathal, "Orientation dependence of the mechanical properties of Ni-base single crystals," *Superalloys 2004*, pp. 83–90, 2003.

[36] M. K. Miller and E. A. Kenik, "Strength and deformation mechanisms of Ni-base superalloys," *Mater. Sci. Technol.*, vol. 23, no. 5, pp. 553–560, 2007.

[37] D. W. MacLachlan and D. M. Knowles, "Deformation behavior of [001] Ni-base single crystals at elevated temperature," *J. Mater. Sci.*, vol. 44, no. 13, pp. 3481–3490, 2009.

[38] Y. Yamabe-Mitarai, Y. Koizumi, H. Harada, and H. Yamagata, "Effects of microstructure on tensile properties of single crystal superalloys," *Mater. Trans.*, vol. 45, no. 6, pp. 1930–1935, 2004.

[39] J. R. Davis, Ed., *ASM Specialty Handbook: Nickel, Cobalt, and Their Alloys*. ASM International, 1997.

[40] X. Cao and J. T. Guo, "Influence of γ' morphology on tensile properties of single crystal superalloys," *J. Mater. Process. Technol.*, vol. 141, no. 1, pp. 88–92, 2003.

[41] J. Y. Guédou, A. Pineau, and D. Caillard, "Study of the fracture mechanisms in single crystal Ni-base superalloys," *Acta Metall. Mater.*, vol. 42, no. 4, pp. 1349–1360, 1994.

[42] A. M. Minor, J. W. Morris Jr., and E. A. Stach, "Nanoscale observation of fracture in Ni-base superalloys," *Scripta Mater.*, vol. 56, no. 6, pp. 379–382, 2007.

[43] S. Suresh, *Fatigue of Materials*, 2nd ed. Cambridge University Press, 1998.

[44] J. Telesman, T. P. Gabb, P. J. Bonacuse, and L. J. Ghosn, "The effects of surface and subsurface inclusions on fatigue crack initiation in a nickel-base superalloy," *Metall. Mater. Trans. A*, vol. 26, no. 4, pp. 1001–1012, 1995.

[45] M. R. Bache, W. J. Evans, and L. G. James, "Fatigue crack propagation in single crystal nickel-based superalloys," *Int. J. Fatigue*, vol. 21, no. 2, pp. 159–172, 1999.

[46] H. Mughrabi and M. Ott, "Fatigue crack initiation and propagation in CMSX-4 single crystal superalloys," in *Superalloys 1996*, TMS, 1999, pp. 501–510.

[47] M. Ott and H. Mughrabi, "Influence of microstructure on fatigue behavior of Ni-based single crystals," *Mater. Sci. Eng. A*, vol. 260, no. 1–2, pp. 276–286, 1999.

[48] L. Rémy and A. Pineau, "Orientation and temperature effects on LCF of single crystals," *Mater. Sci. Eng. A*, vol. 128, no. 1–2, pp. 103–112, 1991.

[49] R. Chieragatti and L. Vergani, "Crack initiation mechanisms in single crystal superalloys," *Fatigue Fract. Eng. Mater. Struct.*, vol. 14, no. 6, pp. 569–583, 1991.

[50] H. Yu, R. L. Peng, Y. Hedberg, and S. Johansson, "Effect of γ' morphology on fatigue in Ni-based SC alloys," *Int. J. Fatigue*, vol. 132, 105358, 2020.

[51] A. Sengupta and R. W. Heckel, "Influence of HIP treatment on fatigue performance of CMSX-4," *Metall. Mater. Trans. A*, vol. 25, no. 5, pp. 993–1004, 1994.

[52] N. E. Prasad and R. J. H. Wanhill, *Aerospace Materials and Material Technologies*, Chapter 9: Superalloys for High-Temperature Applications, 2017.

[53] E. Orowan, "Zur Kristallplastizität," *Z. Phys.*, vol. 89, no. 9–10, pp. 634–659, 1934.

[54] R. Hill, "Generalized constitutive relations for incremental deformation of metal crystals by multislip," *J. Mech. Phys. Solids*, vol. 14, no. 2, pp. 95–102, 1966.

[55] D. Peirce, R. J. Asaro, and A. Needleman, "Material rate dependence and localized deformation in crystalline solids," *Acta Metall.*, vol. 30, no. 6, pp. 1087–1119, 1982.

[56] R. Becker, "Analysis of texture evolution in channel die compression of FCC polycrystals using a Taylor-type crystal plasticity model," *Acta Metall. Mater.*, vol. 39, no. 6, pp. 1211–1230, 1991.

[57] F. Roters, P. Eisenlohr, L. Hantcherli, D. D. Tjahjanto, T. R. Bieler, and D. Raabe, "Overview of constitutive laws, kinematics, homogenization and multiscale methods in crystal plasticity finite-element modeling: Theory, experiments, applications," *Acta Mater.*, vol. 58, no. 4, pp. 1152–1211, 2010.

[58] E. P. Busso and D. L. McDowell, "A dislocation-based finite element model for cyclic viscoplasticity of FCC single crystals," *Int. J. Plast.*, vol. 16, no. 5, pp. 597–626, 2000.

[59] D. Raabe and F. Roters, "Crystal plasticity FEM as a scale-bridging method for metal forming simulations," *Modell. Simul. Mater. Sci. Eng.*, vol. 12, no. 3, pp. R39–R64, 2004.

[60] D. L. McDowell, "A perspective on trends in multiscale plasticity modeling, experimentation, and computation," *Int. J. Plast.*, vol. 24, no. 9, pp. 1282–1309, 2008.

[61] A. Ma, F. Roters, and D. Raabe, "A dislocation density based constitutive model for crystal plasticity FEM including geometrically necessary dislocations," *Acta Mater.*, vol. 54, no. 8, pp. 2169–2179, 2006.

[62] L. Zhang, L. Zhao, R. Jiang, and C. Bullough, "Crystal plasticity finite-element modelling of cyclic deformation and crack initiation in a nickel-based single-crystal superalloy under low-cycle fatigue," *Fatigue Fract. Eng. Mater. Struct.*, vol. 43, no. 8, pp. 1769–1783, 2020.

[63] M. Kaminski, P. Kanouté, S. Kruch, and E. P. Busso, "A high temperature fatigue damage model for single-crystal superalloys," *Mater. High Temp.*, vol. 33, no. 4, pp. 297–309, 2016.

[64] E. H. Lee, "Elastic-plastic deformation at finite strains," *J. Appl. Mech.*, vol. 36, no. 1, pp. 1–6, 1969.

[65] M. E. Gurtin, "A finite-deformation, gradient theory of single-crystal plasticity with free energy dependent on the accumulation of geometrically necessary dislocations," *Int. J. Plast.*, vol. 26, no. 8, pp. 1073–1096, 2010.

[66] M. Ortiz and E. A. Repetto, "Nonconvex energy minimization and dislocation structures in ductile single crystals," *J. Mech. Phys. Solids*, vol. 47, no. 2, pp. 397–462, 1999.

[67] L. Anand and M. Kothari, "A computational procedure for rate-independent crystal plasticity," *J. Mech. Phys. Solids*, vol. 44, no. 4, pp. 525–558, 1996.

[68] V. A. Lubarda, "Elastoplastic theory based on the multiplicative decomposition of deformation gradient: Thermodynamic formulation and implications," *Int. J. Plast.*, vol. 17, no. 6, pp. 751–787, 2001.

[69] J. R. Rice, "Inelastic behavior of solids: Part III—Constitutive relations and internal variables," in *Constitutive Equations in Plasticity*, R. N. Thurston and C. W. Bert, Eds., New York: McGraw-Hill, 1971, pp. 23–79.

[70] S. Flouriot, "Modélisation des effets d'échelle et des bandes de glissement dans les matériaux cristallins: application aux superalliages monocristallins," Ph.D. dissertation, École Nationale Supérieure des Mines de Paris, 2003.

[71] P. Franciosi, M. Berveiller, and A. Zaoui, "Latent hardening in copper and aluminum single crystals," *Acta Metall.*, vol. 28, no. 3, pp. 273–283, 1980.

[72] J. L. Bassani and T. Y. Wu, "Latent hardening in single crystals: Theory and experiments," *Proc. R. Soc. Lond. A*, vol. 435, no. 1893, pp. 21–41, 1991.

[73] E. H. Jordan and K. P. Walker, "Constitutive modeling of single crystal superalloys," *NASA Tech. Memo.*, NASA-TM-86986, 1985.

[74] D. Nouailhas and G. Cailletaud, "Cyclic behaviour of single crystal superalloys under multiaxial loading: Experiments and modelling," *Eur. J. Mech. A Solids*, vol. 14, no. 1, pp. 67–84, 1995.

[75] D. Peirce, R. J. Asaro, and A. Needleman, "An analysis of nonuniform and localized deformation in ductile single crystals," *Acta Metall.*, vol. 30, no. 6, pp. 1087–1119, 1982.

[76] R. J. Asaro, "Micromechanics of crystals and polycrystals," *Adv. Appl. Mech.*, vol. 23, pp. 1–115, 1983.

[77] C. Miehe, M. Hofacker, and F. Welschinger, "A phase field model for rate-independent crack propagation," *Comput. Methods Appl. Mech. Eng.*, vol. 192, pp. 2765–2778, 2002.

[78] Y. Wang, M. Li, Z. Chen, *et al.*, "Crystal plasticity theory coupled with meso-damage to predict the ratchetting behavior of nickel-based single crystal superalloy," *Eng. Struct.*, vol. 263, 115984, 2022.

[79] Y. Gong, A. Ma, Q. Sun, *et al.*, "A microdamage model for FCC single crystals considering a mixed failure mechanism of slip and cleavage," *Int. J. Plast.*, vol. 174, 103892, 2024.

[80] D. R. Jacome, A. M. A. Bastos, E. P. Busso, *et al.*, "Experimental observations of rafting and creep damage in single crystal superalloys," *Acta Mater.*, vol. 61, no. 6, pp. 2041–2056, 2013.

[81] S. Guo, Y. Zhao, and C. Liu, "Microstructural evolution and damage mechanisms in Ni-based single crystal superalloys during high temperature creep," *J. Mater. Sci.*, vol. 56, pp. 4304–4322, 2021.

[82] G. Harikrishnan and J. B. Le Graverend, "A creep-damage phase-field model: Predicting topological inversion in Ni-based single crystal superalloys," *Mater. Sci. Eng. A*, vol. 735, pp. 365–379, 2018.

[83] J. B. Le Graverend, *et al.*, "Creep–fatigue interaction and microstructure degradation in single crystal superalloys," *Procedia Struct. Integr.*, vol. 33, pp. 104–111, 2021.

[84] J. Lemaitre, "A continuous damage mechanics model for ductile fracture," *J. Eng. Mater. Technol.*, vol. 107, no. 1, pp. 83–89, 1985.

[85] L. M. Kachanov, "Time of the rupture process under creep conditions," *Izv. Akad. Nauk SSR Otd. Tekhn. Nauk.*, vol. 8, pp. 26–31, 1958.

[86] Y. N. Rabotnov, *Creep Problems in Structural Members*. North-Holland, Amsterdam, 1969.

[87] J. L. Chaboche, "Continuum damage mechanics: Part I—general concepts," *J. Appl. Mech.*, vol. 55, no. 1, pp. 59–64, 1988.

[88] S. Murakami, "Mechanical modeling of material damage," *J. Appl. Mech.*, vol. 55, no. 2, pp. 280–286, 1988.

[89] C. Miehe, S. Mauthe, and S. Teichtmeister, "Minimization principles for the coupled problem of Darcy–Biot-type fluid transport in porous media linked to phase field modeling of fracture," *Int. J. Numer. Methods Eng.*, vol. 106, no. 9, pp. 683–713, 2016.

[90] N. Bonora, "A nonlinear CDM model for ductile failure," *Eng. Fract. Mech.*, vol. 58, no. 1–2, pp. 11–28, 1997.

[91] B. Li, *et al.*, "Advanced damage modeling of Ni-based superalloys under thermomechanical fatigue," *Mater. Des.*, vol. 231, 111956, 2023.

[92] H. Sabnis, *et al.*, "Directionally anisotropic damage modeling for single crystals," *Comput. Mater. Sci.*, vol. 124, pp. 150–160, 2016.

[93] R. H. J. Peerlings, *et al.*, "Gradient-enhanced damage for quasi-brittle materials," *Int. J. Numer. Methods Eng.*, vol. 39, no. 19, pp. 3391–3403, 1996.

[94] D. Scherer, *et al.*, "Porous single-crystal plasticity with gradient damage," *Int. J. Plast.*, vol. 143, 103011, 2021.

[95] S. Forest, "Micromorphic approach for gradient elasticity, viscoplasticity, and damage," *ASCE J. Eng. Mech.*, vol. 135, no. 3, pp. 117–131, 2009.

[96] G. A. Francfort and J. J. Marigo, "Revisiting brittle fracture as an energy minimization problem," *J. Mech. Phys. Solids*, vol. 46, no. 8, pp. 1319–1342, 1998.

[97] C. Miehe, M. Hofacker, and F. Welschinger, "A phase-field model for ductile fracture at finite strains," *J. Mech. Phys. Solids*, vol. 58, no. 10, pp. 1716–1740, 2010.

[98] M. J. Borden, T. J. R. Hughes, C. M. Landis, and A. Anvari, "A phase-field description of dynamic brittle fracture," *Comput. Methods Appl. Mech. Eng.*, vol. 217–220, pp. 77–95, 2012.

[99] M. Ambati, T. Gerasimov, and L. De Lorenzis, "Review on phase-field models for brittle fracture," *Comput. Mech.*, vol. 55, no. 2, pp. 383–405, 2015.

[100] C. Miehe, F. Aldakheel, and E. Raina, "Phase field modeling of ductile fracture," *J. Mech. Phys. Solids*, vol. 96, pp. 481–502, 2016.

[101] R. Alessi, S. Vidoli, and L. De Lorenzis, "Coupled phase-field and damage models for fracture," *Mech. Mater.*, vol. 124, pp. 26–44, 2018.

[102] B. Wu and J. Zhang, "Phase-field, dislocation based plasticity and damage coupled model: Modelling and application to single crystal superalloys," *Int. J. Plast.*, vol. 154, 103247, 2022.

[103] Z. P. Bažant and T. B. Belytschko, "Wave propagation in a strain-softening bar: exact solution and stability conditions," *Int. J. Solids Struct.*, vol. 24, no. 7, pp. 605–628, 1988.

[104] A. C. Eringen and E. S. Suhubi, "Nonlinear theory of simple micro-elastic solids—I," *Int. J. Eng. Sci.*, vol. 2, no. 2, pp. 189–203, 1964.

[105] S. Forest, "Micromorphic approach for gradient elasticity, viscoplasticity and damage," *J. Eng. Mech.*, vol. 135, no. 3, pp. 117–131, 2009.

[106] N. Marchal, "Propagation de fissure en fatigue-fluage à haute température de superalliages monocristallins à base de nickel," Ph.D. dissertation, École Nationale Supérieure des Mines de Paris, France, 2006.

[107] P. Sabnis, "Modeling of creep fracture in single crystal Ni-based superalloys using a micro-damage approach," Ph.D. dissertation, École des Mines de Paris, 2013.

[108] A. A. Griffith, "The phenomena of rupture and flow in solids," *Philos. Trans. R. Soc. Lond. A*, vol. 221, pp. 163–198, 1921.

[109] G. A. Francfort and J. J. Marigo, "Revisiting brittle fracture as an energy minimization problem," *J. Mech. Phys. Solids*, vol. 46, no. 8, pp. 1319–1342, 1998.

[110] L. Ambrosio and V. M. Tortorelli, "Approximation of functional depending on jumps by elliptic functionals via r-convergence," *Commun. Pure Appl. Math.*, vol. 43, no. 8, pp. 999–1036, 1990.

[111] C. Miehe, M. Hofacker, and F. Welschinger, "A phase field model for rate-independent crack propagation: Robust algorithmic implementation based on operator splits," *Comput. Methods Appl. Mech. Eng.*, vol. 268, pp. 185–218, 2015.

[112] R. Alessi, S. Vidoli, and L. De Lorenzis, "A phenomenological approach to the modeling of fracture in elastoplastic materials via a phase-field method," *Comput. Methods Appl. Mech. Eng.*, vol. 340, pp. 139–166, 2018.

[113] M. Ambati, T. Gerasimov, and L. De Lorenzis, "A review on phase-field models of brittle fracture and a new fast hybrid formulation," *Comput. Mech.*, vol. 55, no. 2, pp. 383–405, 2015.

[114] J. Y. Wu, "A thermodynamically consistent phase-field model for ductile fracture," *J. Mech. Phys. Solids*, vol. 132, 103684, 2020.

[115] M. J. Borden, T. J. R. Hughes, C. M. Landis, and A. Anvari, "Phase-field modeling of brittle fracture," in *Adv. Appl. Mech.*, vol. 55, pp. 1–116, Elsevier, 2022.

[116] L. De Lorenzis and C. Maurini, "Phase-field modeling of anisotropic brittle fracture," *Int. J. Numer. Methods Eng.*, vol. 107, no. 10, pp. 853–888, 2016.

[117] T. Li, F. Roters, and D. Raabe, "On plastic crack driving force in crystal-plasticity phase-field fracture model," *Modell. Simul. Mater. Sci. Eng.*, vol. 31, no. 1, 015008, 2023.

[118] A. Mozaffari, A. Ural, and S. Keten, "An open-source Abaqus implementation of the phase-field method to study the effect of plasticity on the instantaneous fracture toughness in dynamic crack propagation," *Modell. Simul. Mater. Sci. Eng.*, vol. 31, no. 3, 035010, 2023.

[119] C. Miehe, M. Hofacker, and F. Welschinger, "A phase field model for rate-independent crack propagation: Robust algorithmic implementation based on operator splits," *Comput. Methods Appl. Mech. Eng.*, vol. 199, no. 45–48, pp. 2765–2778, 2010.

[120] Y. Shi and Y. Zhao, "A ductile fracture phase field model based on strain rate-dependent dissipation potential," *Modell. Simul. Eng.*, 2024, Article ID 3456701.

APPENDIX A

ALGORITHM 1

This chapter presents the numerical algorithms employed in the finite element implementation of microdamage coupled with crystal plasticity model. The key procedures include the element-level assembly routine and the material integration subroutine, which together define the coupled constitutive framework.

A.1 Psuedo-code for Microdamage User Element Routine

```
SUBROUTINE UEL(...)

  ! Initialization and Setup
  ! Set displacement and microdamage residuals and tangents to zero
  R_u = 0;  R_g = 0;  K_uu = 0;  K_gg = 0

  ! Read geometry, material, and time increment information
  ! such as element parameters, props, nDim, nNode, time, dtime

  ! Allocate storage for SDVs if not already done
  IF (.NOT. ALLOCATED(globalSdv)) THEN
    ALLOCATE(globalSdv(numElem, nInt, ngSdv))
  END IF

  ! Read nodal values: displacements, microdamage, rates
  DO i = 1, nNode
    DO j = 1, nDim
      u(i,j)  = uAll(k)
```

A.1 Psuedo-code for Microdamage User Element Routine (Continued)

```
      du(i,j) = duAll(k)

      v(i,j)  = du(i,j)/dtime
      k = k + 1
    END DO
    gpNew(i) = uAll(k)
    dGP(i)   = duAll(k)
    gpOld(i) = gpNew(i)   dGP(i)
    k = k + 1
  END DO

  ! Check for excessive change in microdamage and cut time step if
     needed
  DO i = 1, nNode
    IF (ABS(dGP(i))   1.0E6) THEN
      pnewdt = 0.5
      RETURN
    END IF
  END DO

  ! Update current nodal configuration
  DO i = 1, nNode
    coordsC(:,i) = coords(:,i) + u(i,:)
  END DO

  ! Integration Setup: choose Gauss integration rule
  IF (nInt == 8) THEN
    CALL xint3D8pt(...)
  ELSE
    CALL xit(...)
  END IF
```

A.1 Psuedo-code for Microdamage User Element Routine (Continued)

```
1
2   ! Begin loop over Gauss points
3   jj = 0
4   DO intpt = 1, nIntPt
5
6     ! Load state variables
7     IF (kinc == 1 .AND. kstep == 1) THEN
8       ! Initialize plastic and damage gradients at start
9       F_p^t = I;  F_d^t = I;  γ^t = 0;  d^t = 0
10    ELSE
11      ! Read previous values from state variables
12      ! F_p^t, F_d^t, γ^t, d^t
13    END IF
14
15    ! Compute shape functions and derivatives
16    CALL calcShape3DLinear(...)
17    CALL mapShape3D(...)
18
19    ! Evaluate microdamage fields and kinematic quantities
20    ! Compute: gp_τ, gp_t, ∇gp, ġp
21    ! Compute: ∇v, F_τ, F_t
22    ! Compute: J̇ = (det F_τ − det F_t)/Δt
23
24    ! Perform constitutive integration
25    CALL INTEG(...)
26    ! Updates: T^τ, F_p^τ, F_d^τ, d^τ, γ^τ
27
28    ! Save updated internal variables
29    svars(jj + ...) = updated internal variables
30
31    ! Store field outputs for visualization or postprocessing
32    globalSdv(elemPt, intpt, :) = (T^τ, d^τ, ∇d)
```

A.1 Psuedo-code for Microdamage User Element Routine (Continued)

```
    ! Compute residuals
    ! Construct B matrix for strain displacement coupling
    ! B ∈ ℝ^{6×24}
    S = Voigt(T^τ)
    R_u += −B^T S · det J · w

    DO i = 1, nNode
      ! Add microdamage contributions to residual
      R_g(i) += det J · w · (β∇gp · ∇N_i + N_i P_τ)
    END DO

    ! Compute tangent stiffness matrices
    K_uu += B^T C B · det J · w

    DO i = 1, nNode
      DO j = 1, nNode
        K_gg(i, j) += − det J · w · (β∇N_i · ∇N_j + N_i N_j ∂P/∂gp)
      END DO
    END DO

    jj = jj + nLocalSDV
  END DO
  ! End of Gauss point loop

  ! Assemble residual vector for solver
  DO i = 1, nNode
    A11 = (nDim+1) (i 1) + 1
    A12 = nDim (i 1) + 1
    rhs(A11:A11+2,1) = R_u(A12 : A12 + 2)
    rhs(A11+3,1)     = R_g(i)
  END DO
```

A.1 Psuedo-code for Microdamage User Element Routine (Continued)

```
1   ! Assemble tangent matrix for solver
2   DO i = 1, nNode
3     DO j = 1, nNode
4       A11 = (nDim+1) (i 1) + 1
5       A12 = nDim (i 1) + 1
6       B11 = (nDim+1) (j 1) + 1
7       B12 = nDim (j 1) + 1
8
9       amatrx(A11:A11+2,B11:B11+2) = K_uu(A12 : A12 + 2, B12 : B12 + 2)
10      amatrx(A11+3,B11+3)         = K_gg(i, j)
11    END DO
12  END DO
13
14  elemPt = elemPt + 1
15  RETURN
16
17 END SUBROUTINE
```

APPENDIX B

ALGORITHM 2

This chapter presents the numerical algorithms employed in the finite element implementation of microdamage coupled with crystal plasticity model. The key procedures include the element-level assembly routine and the material integration subroutine, which together define the coupled constitutive framework.

B.1 Psuedo-code for Microdamage User Material Routines

```
SUBROUTINE INTEG(...)

  ! Initialization
  ! Set identity tensor and initialize material parameters
  ! Construct elastic stiffness tensor:  ℂ
  ! Set consistent tangent:  ℂ_tan = ℂ

  !
  ! Damage Update
  CALL DAMAGE(...)

    ! Compute trial elastic deformation gradient:
    !    F_e^tr = F F_d^-1 F_p^-1

    ! Compute logarithmic strain:
    !    E_e^tr = log(U_e^tr)
```

B.1 Psuedo-code for Microdamage User Material Routines (Continued)

```
1   ! Evaluate Mandel stress:
2   !   M_e^tr = ℂ : E_e^tr
3
4   ! For each damage direction i:
5   !   Project stress: n^(i) · M_e^tr · n^(i)
6   !   Evaluate driving force:  f^(i) = n^(i) · M_e^tr · n^(i) − Y
7
8   !   If f^(i) > 0, evolve damage:
9   !     Δd^(i) = ( f^(i) / K_d )^(n_d)
10
11  ! Accumulate damage tensor:
12  !   D = Σ_i Δd^(i) n^(i) ⊗ n^(i)
13
14  ! Integrate damage deformation gradient:
15  !   F_d^τ = exp(DΔt) F_d^t
16
17  RETURN
18
19  !
20  ! Plasticity Update
21  CALL PLAST(...)
22
23  ! Compute trial elastic deformation gradient:
24  !   F_e^tr = F F_d^-1 F_p^-1
25
26  ! Evaluate logarithmic strain: E_e^tr
27  ! Compute Mandel stress: M_e^tr = ℂ : E_e^tr
```

B.1 Psuedo-code for Microdamage User Material Routines (Continued)

```
    ! For each slip system s = 1 to 12:
    !   Compute resolved shear: τ^(s) = M_e^tr : P^(s)
    !   Back stress: x^(s), slip resistance: r^(s)
    !   Evaluate yield function: f^(s) = |τ^(s) − x^(s)| − r^(s)
    !   If f^(s) > 0, compute:
    !      γ̇^(s) = (f^(s)/k)^n sign(τ^(s) − x^(s))
    !      Δγ^(s) = γ̇^(s) Δt

    ! Construct stretching tensor: D_p = Σ_s Δγ^(s) P^(s)
    ! Integrate plastic flow: F_p^τ = exp(D_p) F_p^t
    ! Update accumulated slip: ε̄_p^τ = ε̄_p^t + Δt Σ_s |γ̇^(s)|

    RETURN
  !
  ! Elastic Update

  ! Recompute elastic gradient: F_e^τ = F F_d^-1 F_p^-1
  ! Polar decomposition: F_e^τ = R_e^τ U_e^τ
  ! Logarithmic strain: E_e^τ = log(U_e^τ)
  ! Mandel stress: M_e^τ = ℂ : E_e^τ
  ! Compute Cauchy stress:
  !    σ^τ = (1/det F_e) F_e M_e F_e^-T
  RETURN
END SUBROUTINE
```

CURRICULUM VITAE

Surname, Name: Kasar, Çağatay

EDUCATION

Degree	Institution	Year of Graduation
Integrated PhD	Atılım University Mechanical Engineering	2025
BS	Middle East Technical University Metallurgical and Materials Engineering	2020
High School	Ayhan Sümer Anadolu Lisesi, Ankara	2014

FOREIGN LANGUAGES

Fluent English

PUBLICATIONS

1. Kasar, Ç.; Kaftancioglu, U.; Bayraktar, E.; Aslan, O. Lifetime Prediction of Single Crystal Nickel-Based Superalloys. Appl. Sci. 2025, 15, 201.
2. Kasar, Ç., Aslan, Ö., Gatamorta F., Miskioğlu, İ., Bayraktar, E. (2023). Development of Ni-Al/Nb2Al/ZrO2-Based Design of Recycled Aluminium (AA7075)-Based Composites Reinforced with Nano Filler NiAl Intermetallic. In: CNanofillers for Sustainable Applications, 1st Edition, CRC Press, 2023. ISBN: 9781003400998.

RESEARCH INTERESTS

- ➢ Ni-Based Single Crystal Superalloys
- ➢ Consitutive Modeling
- ➢ Damage Mechanics
- ➢ Fatigue Damage